

Novel Materials for Picosecond Devices Ranging from Spintronics to Radiation Detection

by
Jing Cheng

Submitted in Partial Fulfillment of the
Requirements for the Degree
Doctor of Philosophy

Supervised by
Professor Roman Sobolewski

Materials Science Program
Arts, Sciences and Engineering
Edmund A. Hajim School of Engineering and Applied Sciences

University of Rochester
Rochester, New York

2025

Table of Contents

Biographical Sketch	vi
Acknowledgments	vii
Abstract	ix
Contributors and Funding Sources	xi
List of Figures	xiii
1 Introduction	1
1.1 Motivation	1
1.2 (Cd,Mg)Te materials background	2
1.3 THz spintronics materials background	4
1.4 Pulse characterization of Ti:Sapphire laser system	6
1.5 Ultrafast Signal Detection	8
1.6 Outline of thesis	10
2 State-of-the-Art Developments in THz Spintronics and CdTe-	

Based detectors	12
2.1 THz radiation emission and detection	12
2.1.1 Introductions to THz radiation	12
2.1.2 Photoconductive antenna	14
2.1.3 Optical rectification	17
2.1.4 Spintronic emission and detection	18
2.2 Development of CdTe-based detectors	23
2.2.1 Introduction to wide-range ultrafast detector	23
2.2.2 CMT detector incentives	25
2.2.3 CMT material background	26
2.2.4 CMT Performance for Nuclear Detection Applications .	27
3 Experimental approach	29
3.1 Terahertz time-domain spectroscopy (THz-TDS) system	29
3.1.1 THz time-domain system	30
3.1.2 Low temperature measurements	33
3.2 CdMgTe materials and device characterization methods	34
3.2.1 Pump-probe spectroscopy	34
3.2.2 Device measurements	37
4 Dynamics of THz Spintronics in Various Systems	39
4.1 Sample fabrication and characterization	39
4.1.1 Thin films fabrication	39
4.1.2 Graphene synthesis and characterization	40

4.2	Generation mechanisms of FeCo/graphene heterostructure . . .	44
4.2.1	Emission layer	44
4.2.2	Main emission mechanism	46
4.2.3	Evaluation of Inverse Rashba-Edelstein Length	48
4.3	Circular Photogalvanic Effect	51
4.4	Spin texture of a single-layer graphene	56
4.5	Temperature-dependent THz transients in weakly remnant Py nanolayers	58
4.6	Terahertz Emission from Tunneling FeCo/ MgO/Pt Spintronic Heterostructures	61
5	CdMgTe materials and device characterization	68
5.1	Crystal growth	68
5.2	Charge transport measurements	72
5.3	Bandgap and picosecond response measurements	73
5.4	Device fabrication	79
5.5	Electrical photoconductive effect and responsivity	83
5.6	Time-resolved photoresponse	86
5.7	Three terminal Device	89
5.8	Improved time-resolved photoresponse	91
6	Future Work	93
6.1	Future work about THz spintronics	93

6.1.1	Temperature-dependent THz transients in moderately remnant CoPd and strongly remnant FeCo nanolayers .	93
6.1.2	THz Measurements in the reflection mode	94
6.2	Future work about CMT detector	95
6.2.1	Electro-optic sampling	95
	Bibliography	97

Biographical Sketch

The author was born in Wuhan, Hubei Province, China. She completed her Bachelor of Science degree in Materials Science at Northeastern University. In 2019, she began her doctoral studies in Materials Science at the University of Rochester, where she focused on ultrafast phenomena under the guidance of Professor Roman Sobolewski.

Acknowledgments

I am deeply grateful to my advisor, Roman Sobolewski, for his invaluable guidance—not only in my research but also in my daily life. Thank you for being such an exceptional mentor and role model.

I would also like to extend my heartfelt appreciation to my committee members, Gary Wicks, Tod Krauss, Ivan Komissarov, and Jaime Cárdenas, for their insightful guidance and support throughout my thesis journey.

My sincere thanks go to the various departments at the Laboratory for Laser Energetics, including the mechanical, electrical, and chemical divisions, whose support ensured the smooth execution of my daily experiments. I am also incredibly grateful to the LLE coordinators for assisting with administrative matters and organizing my travel to conferences.

A special thanks to my research group colleagues, Genyu Chen, Yunus Akbaş, and Debamitra Chakraborty—I have learned so much from each of you, and I truly appreciate your generous help in every aspect. I am also grateful to my friends at LLE, Junchi Zhang, Yihan Liu, and Yu Zhang—the time we spent together was truly memorable. Additionally, I would like to

thank Bill Donaldson for always inviting me to the daily bridge games and for the many fascinating conversations we shared.

I am also grateful to my dear friends, You Zhang, Zhewen Yang, Pei Xiong, Xue Dong, Ziqi Zhang, Yingjie Wu, Yuxuan Liu, Shizhao Liu, Meiling Ying, Yiwen E, Yueling Chen, Hanling Liao, Junran Ye, Bo Wen, Qianqian Wei, Huiying Wang, and Ming Wang, for their friendship and support. We shared so many wonderful moments together, and I truly appreciate your companionship. These memories are incredibly meaningful to me—thank you all for being a part of them.

I would also like to thank the friends I met during my internship at Canon Medical Research USA. This was my very first internship, and I was fortunate to have an incredible mentor, Xiaohui Zhan, and a supportive manager, Yi Qiang. I am also grateful to my friends Xi Chen, Efren Lee, Lorie, Kayla, and Alex, who made this journey so enjoyable and unforgettable.

Most importantly, I want to express my deepest gratitude to my family—my parents and younger sister—for their unwavering love, support, and belief in me.

Last but certainly not least, to my fiancé, Yuxin (Ethan) Chen—thank you for your constant support over the past five years. You have helped me grow into a better person, and for that, I am forever grateful.

Abstract

The advancement of ultrafast optoelectronic and spintronic devices requires novel materials with superior properties. This dissertation explores two key areas: CdMgTe (CMT) semiconductor-based detectors for ultrafast radiation detection and spintronic heterostructures for efficient terahertz (THz) emission.

The primary goal of this work is to investigate and optimize material properties for high-speed detection and THz signal generation. For CMT-based detectors, the research focuses on understanding charge transport dynamics, bandgap tunability, and photoconductive response to enable ultrafast optical-to-X-ray detection. In the THz spintronics study, the goal is to explore novel metallic ferromagnetic heterostructures with and without a tunneling MgO layer, as well as FeCo/graphene bilayers, to enhance spin-charge conversion efficiency for THz emission.

The methodology involves femtosecond pump-probe spectroscopy, time-resolved photoconductivity measurements, and THz time-domain spectroscopy (THz-TDS). The CMT device fabrication process includes cleanroom-based

lithography and e-beam deposition techniques.

Results show that CMT materials exhibit high carrier mobility and fast response times, making them very suitable for ultrafast detection of radiation ranging from optical to X-ray. Graphene-based spintronic heterostructures demonstrate strong THz emission with enhanced spin-orbit coupling. In the tunneling heterostructure, the MgO layer induces a change in the spin polarization of THz emission. These findings advance next-generation ultrafast photodetectors and THz spintronic emitters for high-speed communications, imaging, and spectroscopy.

Contributors and Funding Sources

This work was supported by a dissertation committee consisting of Professor Roman Sobolewski and Professor Ivan Komissarov from the Department of Electrical and Computer Engineering and the Materials Science program, Professor Gary Wicks and Professor Jaime Cárdenas from the Institute of Optics, and Professor Todd Krauss from the Department of Chemistry. The experiments presented in Chapter 4 were conducted with the early assistance of Dr. Genyu Chen and analyzed with the help of Professor Ivan Komissarov, Dr. Roman Adam, and Dr. Daniel Bürgler at the Research Center Jülich, Germany. Some analyses presented in Chapter 5 were carried out with the support of Dr. Henry Chen and Sudhir Trivedi from Brimrose Co. All other work conducted for this dissertation was completed independently by the author.

The CMT-related research was supported in part by the Brimrose Co through the Department of Energy under Award DE-SC0021468. The THz spintronics project was supported by the University of Rochester National Inertial Confinement Fusion Program under Award DE-NA0004144, the Uni-

versity of Rochester University Research Award (URA) Program and support from Research Center Jülich, Germany.

List of Figures

- 1.1 Bandgap energy as a function of composition at 2 K and 300 K. The solid line is a quadratic fit (eq. 1.1) of the bandgap at 300 K . Translated upward 0.1 eV a match between this quadratic fit and the bandgap at 2 K is obtained. The dotted line is an approximate linear fit of the bandgap of alloys at 2 K [5]. 4
- 1.2 Normalized intensity autocorrelation of a Gaussian pulse with a duration of 102 fs, measured in our MIRA 900 laser system. 7
- 1.3 Optical sampling techniques.(a) Real-time sampling (b) Equivalent-time sampling 9
- 2.1 Terahertz gap in the electromagnetic spectrum [26] 13
- 2.2 The photoconductive switch with a hemispherical Si lens used as a THz emitter (a) and as a THz detector (b). Dark parts represent the LT-GaAs substrate and red dots and lines represent a laser pulse focal spot and direction. 15

- 2.3 Conceptual overview of THz emission from spintronic devices.
 (a) Laser excitation of a magnetic material (e.g., Fe) creates more majority than minority spins. (b) The inverse spin Hall effect at the Fe/Pt interface induces a transient charge current, generating THz emission. The spin current \mathbf{J}_s propagates normal to the interface, and the charge current \mathbf{J}_c , generated by the inverse spin Hall effect, gives rise to a THz transient [56]. 19
- 2.4 (a) Room-temperature response of a $9 \times 7 \times 1.5\text{-mm}^3$ pseudo-hemispherical $\text{Cd}_{1-x}\text{Mg}_x\text{Te}$ detector at 450 V to an Am-241 gamma source, demonstrating an energy resolution of 7% at 60 keV. (b) Cs-137 (662 keV) gamma response of a $4.5 \times 4.5 \times 9\text{-mm}^3$ $\text{Cd}_{1-x}\text{Mg}_x\text{Te}$ detector in a Frisch-Grid configuration (see inset). 28
- 3.1 Schematic of the THz time-domain measurement setup. BS denotes the beam splitter, while M1–M4 represent four dielectric mirrors. The two magnets indicate the coil used to generate an external magnetic field. PEM refers to the photoelastic modulator 31
- 3.2 Cross-section of the cryostat with a spintronic emitter operated at variable temperatures 34
- 3.3 Configuration for pump probe spectroscopy which could measure both reflectivity or transmissivity variations 36

3.4	Diagram of experimental setup for device photoresponse measurements	37
4.1	Typical Raman spectra of single-layer (a) and few-layer (b) graphene, and the 2D band position as a function of the G band position (c). Stars indicate positions of unstrained, undoped graphene for 1- to 4-layer graphene. The bold solid line (slope = 2.2) represents biaxial strain variation, while dashed lines (slope = 0.7) indicate charge carrier concentration variation.	41
4.2	Maps of the I_{2D}/I_G intensity ratio and the morphology of graphene transferred onto the MgO/FeCo structure. The maps represent measurements taken from different regions of the sample.	42
4.3	High resolution TEM image of a MgO/FeCo (6 nm)/graphene sample with 2 nm resolution bar	43
4.4	THz emission from FeCo/graphene nano bilayer. (a) THz transients emitted from FeCo/Graphene bilayer. (b) The power spectrum of the experimental waveform.	44
4.5	(a) THz emission from a FeCo/MgO nanobilayer (orange) and a pure FeCo layer (blue). (b) Corresponding THz power spectra of experimental waveforms.	45

-
- 4.6 Evaluation of the mechanism of THz generation in the FeCo/graphene nanobilayer. (a) THz transients emitted from the sample under excitation from opposite directions. (b) Magnetization (black curve) and the amplitude of the THz signal (red dashed line) as functions of the external magnetic field. Both the magnetic moment and THz peak amplitude curves were normalized at 50 kA/m to enable direct comparison. 47
- 4.7 Evaluation of inverse Rashba-Edelstein length of graphene and Rashba spin texture (a) THz waveforms for FeCo/Ir (red) and FeCo/graphene (black) nanobilayers, recorded under the same experimental conditions. The insets show the mutual orientations of j_s , j_C , and M based on the value of θ_{SHE} for Ir (b) Fermi contours for minority (blue) and majority (red) spins in graphene conducting band. Dashed contours correspond to the shifted Fermi contours due to injection of spin polarized (spins parallel to M) electrons. 49

- 4.8 (a) THz transients recorded using a photoelastic modulator for two opposite directions of FeCo/graphene magnetization (blue and red) and a demagnetized sample (black). (b) and (c) The scheme of the graphene band diagram with SOC and exchange interaction included for an external magnetic moment parallel, $M \parallel +k_y$ (b), and antiparallel $M \parallel -k_y$ (c). Blue and red correspond to the orientations of the spins (S_y), parallel (blue) and antiparallel (red) to k_y . The presented dispersions are expressly distorted to clearly demonstrate the discussed effects. 52
- 4.9 (a) and (b) show the allowed transitions for right-hand circularly polarized light, for $M \parallel +k_y$ and $M \parallel -k_y$, respectively. (c) and (d) show the allowed transitions for left-hand circularly polarized light, for $M \parallel +k_y$ and $M \parallel -k_y$, respectively. The thick red arrows represent the generated charge currents. The longer arrows correspond to larger currents. 54
- 4.10 Spin texture of single layer graphene when both spin-orbit coupling and exchange energies are presented 57
- 4.11 THz amplitudes, $A_{\text{THz}}(H)$ (left y-axis; red and blue dots), and magnetization, $M(H)$ (right y-axis; black solid line), of a Py/Pt bilayer as a function of the external magnetic field H . The inset provides a magnified view of the region near the origin for better visualization of fine details. 59

4.12 (a) $A_{\text{THz}}(T)$ of a Py/Pt sample as a function of reduced temperature (T/T_C) under different B_{ext} , with the black curve representing MPMS magnetization measurements. (b) qualitative fitting of relative magnetization versus reduced temperature, with the inset comparing relative magnetization and normalized THz peak amplitude.	60
4.13 Time-domain THz transients measured from a 6-nm FeCo/4-nm Pt bilayer in the direct (black), reverse (blue), and 180° in-plane rotation (red) geometries. The bilayer orientation is depicted in the inset.	62
4.14 THz-TDS transients measured from a 6-nm FeCo/1-nm MgO/4-nm Pt trilayer in the same geometry.	63
4.15 Enter Caption	64
4.16 Enter Caption	65
4.17 Angular dependence of a normalized signal for FeCo/Pt and FeCo/MgO/Pt samples. The $\mu = 0$ case corresponds to the sample/detector configuration shown in the inset	67
5.1 Schematic diagram of the Vertical Bridgman method.	69
5.2 (a) Bridgman Grown CdMgTe crystalline boule and a sample prepared for detector fabrication; (b) a vacuum sealed ampoule for annealing	70

5.3	Cd _{1-x} Mg _x Te single crystal wafers with different bandgaps: upper right $x = 0.45$, upper left $x = 0.45$, lower left $x = 0.15$, and lower right $x = 0.03$	71
5.4	Hecht-fit via Am-241 response for obtaining $\mu\tau_e$ value.	73
5.5	transmission and reflection spectra of CMT crystal with 3% Mg	74
5.6	Absorption coefficient spectra of CMT crystal	75
5.7	Tauc plot of a Cd _{0.97} Mg _{0.03} Te single crystal. Two different samples were tested to analyze the optical properties of the material	76
5.8	Cd _{1-x} Mg _x Te ($x = 0.03$), single crystal pump-probe measurement results, indicate an ultrafast (2.5 ps) photoresponse with a 3 ps single-exponential relaxation. The exponential fit (solid black line)).	79
5.9	A proof-of-concept CMT surface photodetector. Inset on the left shows with a meander electrode pattern in detail. The device was wirebonded to an SMA (Sub-Miniature Version A) connector for high-speed measurements.	80

5.10	(a) Schematic design of the fabricated pattern, illustrating the geometric dimensions of the structure, including the active area ($600 \mu\text{m} \times 600 \mu\text{m}$), finger width ($30 \mu\text{m}$), finger spacing ($30 \mu\text{m}$), and total finger length ($570 \mu\text{m}$). The large trapezoidal pads have widths of 1 mm and 2 mm, designed to mitigate power reflections. (b) Optical microscope image of the fabricated pattern, demonstrating the successful transfer of the design onto the CMT crystal.	81
5.11	I–V characteristics under light (red) and dark (blue) conditions for a tested CMT MSM device. The inset shows the dark current I–V in detail (bulk measurement across a CMT sample).	84
5.12	The I–V characteristics of our proof-of-concept $\text{Cd}_{1-x}\text{Mg}_x\text{Te}$ ($x = 0.03$) photodetector were measured under various power levels of 800-nm optical excitation. The beam diameter was approximately $300 \mu\text{m}$	85
5.13	Responsivity as a function of bias voltage. The calculations are shown for various values of incident optical power	87
5.14	Time resolved CMT detector response to a pulsed x-ray, 800 nm, high harmonics signals	88

5.15	(a) Schematics of interdigitated surface electrodes and a back-crystal contact to collect X-ray-generated electrons. (b) A proof-of-concept three-terminal device to be developed for simultaneous surface absorption, optical, and volume transmission X-ray experiments.	89
5.16	Optical photoresponse experimental results for volume detector at the HHG facility	90
5.17	Time-resolved CMT detector response to pulsed 800 nm signals, measured using a 25-GHz bandwidth oscilloscope. Blue: Measured photoresponse; Red: Response smoothed by a high-pass filter; Black: Gaussian fit. Inset: New package, allowing direct insertion of the MSM into the SMA connector.	92
6.1	THz peak amplitude values of CoPd/Pd (blue dots) and CoFe/Ir (orange dots) samples as a function of temperature.	94
6.2	(a) A time resolved CMT photoconductive response measured at $75 \mu\text{m}$ from the excitation spot via the internal EO effect. (b) the schematic of two-color EOS setup. [146]	96

Chapter 1

Introduction

1.1 Motivation

My thesis focuses on novel materials for ultrafast devices and is divided into two distinct parts, each with its own objectives. The first part investigates the THz emission mechanism in CoFe/graphene, a novel nanobilayer structure consisting of a ferromagnetic (FM) layer and graphene. While graphene has yet to be explored for THz spintronic devices, well-established heterostructures containing FMs and heavy metals (HMs) have been the focus of research for over a decade. Additionally, I conducted an extensive study on various FM/heavy metal systems and introduced the MgO tunneling layer. This study focuses on THz emission from graphene-based spintronic emitters and has the potential to broaden the scope of graphene applications, paving the way for new THz spintronic devices.

The second part of my thesis focuses on the development of a picosecond-response optical-to-x-ray cadmium magnesium telluride (CMT) radiation de-

tector. Currently, available photodetectors lack the capability to provide the broad spectral coverage required for course timing of optical and X-ray pulses in time-resolved pump-probe experiments. To address this limitation, my objective is to bridge this gap by investigating the optical and electronic properties of CMT materials through femtosecond all-optical pump-probe spectroscopy and time-resolved photoresponse studies. After identifying the optimal Mg concentration in CMT crystals. I designed the transmission line circuit and packaging for the CMT photodetector. Using maskless laser lithography in a cleanroom environment, I fabricated the desired patterns and conducted extensive experiments to characterize the device. By achieving these objectives, I aim to position the CMT detector as a promising candidate for high-speed optical-to-x-ray detection, thereby expanding the capabilities of both research and commercial photodetection technologies.

Since conventional oscilloscopes lack the temporal resolution required to characterize ultrafast responses in the picosecond range, all projects in this thesis employ femtosecond Ti:sapphire lasers and utilize the sampling detection method. The details of this experimental approach will be discussed in depth in the corresponding chapter.

1.2 (Cd,Mg)Te materials background

$\text{Cd}_{1-x}\text{Mg}_x\text{Te}$, with a composition range of $x = 0$ to 0.45, adopts the zinc blende crystal structure and represents the latest addition to ternary al-

loy systems. It joins the well-established (Cd,Zn)Te and (Cd,Mn)Te crystals, both widely recognized for their applications in X-ray detection [1]. CMT exhibits all the essential properties of an optimal radiation detector, including high material density ($5.83 \cdot \text{g}/\text{cm}^3$), a large effective atomic number (49.5), ultrahigh resistivity ($10^{10} \Omega \cdot \text{cm}$), and a high electron mobility-lifetime ($\mu\tau_e$) product ($> 10^{-4} \text{cm}^2\text{V}^{-1}$) [2]. Moreover, the “parent” crystals, CdTe and MgTe, have nearly identical lattice constants (6.48 Å and 6.42 Å, respectively), facilitating high-quality growth of single CMT crystals [3]. At room temperature, bandgap of CMT is tunable from 1.5 eV ($x = 0$) to 3.5 eV ($x = 1.0$) as the function shown below, increasing at a rate of approximately 17 meV per Mg atomic percent [4]:

$$E_g = 1.5 + 1.7x + 0.3x^2 \quad (1.1)$$

Figure 1.1 presents the lowest direct bandgap energy (E_g) as a function of alloy composition (x) for CMT. At both 2 K and 300 K, a similar trend is observed, where E_g increases with increasing Mg concentration; however, the bandgap values are shifted by approximately 0.1 eV between the two temperatures [5]. Notably, the incorporation of Mg not only widens the bandgap but also leads to a slight reduction in the lattice constant. A previous study by our group reported a 0.4% decrease in the lattice constant as the Mg concentration increased to 0.68 [6].

We aim to achieve an optimal bandgap with approximately 3 - 10% Mg

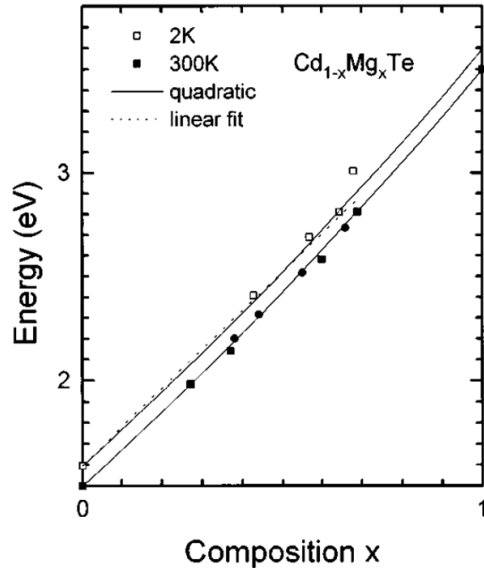


Figure 1.1: Bandgap energy as a function of composition at 2 K and 300 K. The solid line is a quadratic fit (eq. 1.1) of the bandgap at 300 K. Translated upward 0.1 eV a match between this quadratic fit and the bandgap at 2 K is obtained. The dotted line is an approximate linear fit of the bandgap of alloys at 2 K [5].

concentration. We focused on determining the ideal Mg concentration and dopant levels for growing CMT crystals with low defect density and good uniformity, to obtain material exhibiting picosecond X-ray and optical response.

1.3 THz spintronics materials background

THz spintronics is an emerging field that leverages spin-based phenomena for ultrafast signal processing and information technology applications. The development of efficient THz spintronic devices relies on the discovery and

optimization of novel materials with strong spin-orbit coupling, ultrafast spin dynamics, and high spin-to-charge conversion efficiency. Key materials in this field include heavy metals such as Pt, W, and Ta, which exhibit strong spin Hall effects [7], as well as topological insulators like Bi_2Se_3 , which provide efficient spin-momentum locking for enhanced spin transport [8]. Additionally, antiferromagnetic materials such as Mn_2Au and CuMnAs are gaining attention due to their potential for high-speed operation without stray magnetic fields [9]. The integration of two-dimensional (2D) materials, including graphene and transition metal dichalcogenides (TMDs), further expands the possibilities for THz spintronic applications by offering tunable electronic and spintronic properties [10]. Recent advances also highlight the role of heterostructures that combine different class of material to achieve superior spintronics performance [11].

In this work, we focus on graphene, a widely studied natural 2D material with unique band structure and optical properties. Graphene is often considered an ideal medium for spin information transfer due to its long spin diffusion length [12]. However, its intrinsic spin-orbit coupling (SOC) energy is extremely low, on the order of a few μeV [13], which limits its applicability in spintronic applications requiring spin manipulation.

Several strategies have been employed to enhance the SOC in graphene. For instance, the controlled addition of small amounts of covalently bound hydrogen atoms can increase the SOC by three orders of magnitude, up to 2.5 meV [14]. Similarly, fluorine functionalization has been shown to achieve

SOC values as high as 9.1 meV [15]. Another approach involves decorating graphene with heavy ion adatoms, which also significantly enhance its SOC [16]. Additionally, *d*-block metals such as Au, Ti, or In, which exhibit strong SOC, can open a bandgap at the Dirac point of graphene [16, 17].

A further mechanism for Rashba SOC enhancement in graphene is hybridization between the π -states of graphene and the $3d$ -states of ferromagnetic (FM) metals, such as Co [18]. Considering that the spin Hall angle (θ_{SHE}) of chemical vapor deposition (CVD)-grown graphene (~ 0.2) [19] is comparable to values observed in heavy metals (HMs) [20], this approach is particularly appealing. The FM/graphene bilayer system can serve as a promising candidate for terahertz (THz) emitters, leveraging the enhanced SOC for efficient spintronic applications.

1.4 Pulse characterization of Ti:Sapphire laser system

A self-mode-locked femtosecond Ti:Sapphire laser is used for all experiments in this dissertation, featuring ultrashort pulses and tunable wavelengths. The Ti:Al₂O₃ crystal's broad emission spectrum (700–1,050 nm) results from lattice distortions [21]. Mode-locking utilizes the Kerr lens technique [22], where high-intensity modes focus better, enabling CW suppression via an adjustable slit [23]. Adjustable prisms compensate for group velocity dispersion, producing 80–150 fs pulses.

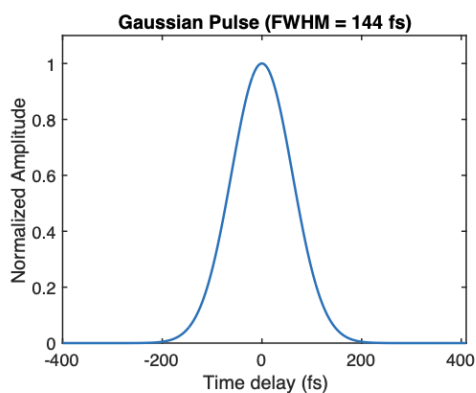


Figure 1.2: Normalized intensity autocorrelation of a Gaussian pulse with a duration of 102 fs, measured in our MIRA 900 laser system.

Our system operates within the 750–850 nm wavelength range, maintaining a stable pulse width of approximately 100 fs. Pulse duration was measured using an autocorrelator (Inrad), which splits the laser beam into two parts, introduces a relative delay, and recombines them in a nonlinear crystal [24]. The resulting Gaussian autocorrelation trace (Fig. 1.2) exhibits a full width at half maximum (FWHM) of 144 fs, corresponding to a calculated pulse width of 102 fs. The slight broadening is attributed to the influence of optical components. With a repetition rate of 76 MHz and an operational output power of 1 W, the Ti:Sapphire laser is well-suited for a variety of ultrafast spectroscopy applications.

1.5 Ultrafast Signal Detection

An oscilloscope is the fundamental instrument for time-domain measurements, with its operating principle illustrated in Fig. 1.3(a) [25]. However, real-time capture of ultrafast carrier dynamics on picosecond timescales is impractical due to the limited bandwidth of conventional oscilloscopes.

To overcome this limitation, repetitive sampling can be employed, as shown in Fig. 1.3(b). In the first acquisition cycle, when a trigger event occurs, a probe pulse of finite duration Δt samples a single point of the signal. In the next cycle, an identical probe pulse, delayed by a time interval $\Delta\tau$ relative to the previous pulse, samples another section of the waveform. By repeating this process across multiple acquisition cycles, a sequence of sample points separated by $\Delta\tau$ is recorded. This method enables accurate waveform reconstruction through linear interpolation, provided that the trigger exhibits minimal jitter and the time delay is precisely controlled. The key advantage of this technique is that it allows the oscilloscope's effective bandwidth to exceed its real-time bandwidth, as only one sample point is captured per period.

Optical sampling systems operate on the same principle as electronic sampling oscilloscopes but use ultrashort optical pulses as probes instead of electrical pulses. Since optical pulses are significantly shorter in duration, they enable higher bandwidth and subpicosecond time resolution, making them indispensable for ultrafast spectroscopy.

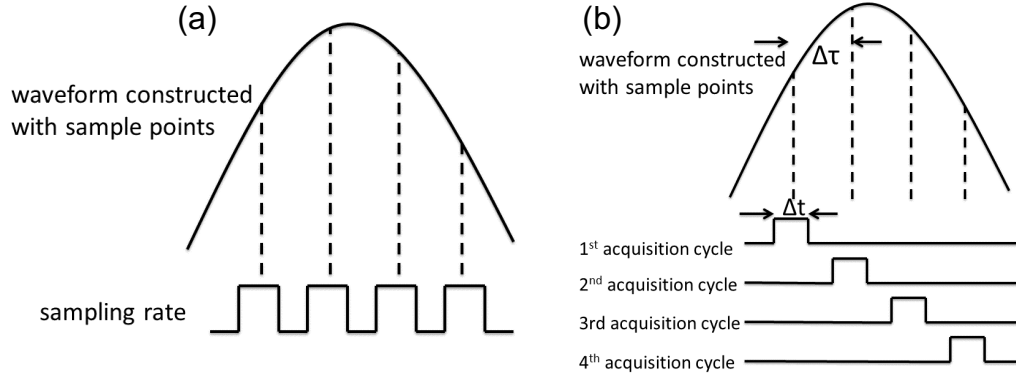


Figure 1.3: Optical sampling techniques.(a) Real-time sampling (b) Equivalent-time sampling

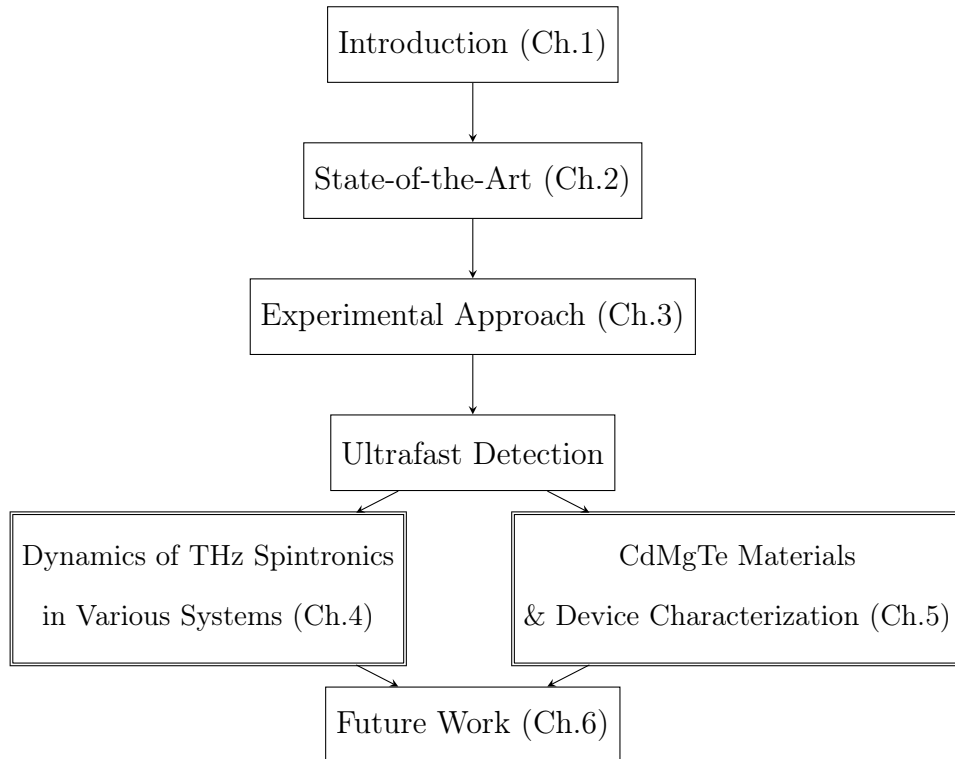
Advanced detection systems are also critical in ultrafast spectroscopy. In our THz spectroscopy experiments, free-space THz detectors from Teravil, with subpicosecond resolution and bandwidths up to 5 THz are widely used. These detectors, based on a LT-GaAs photoconductive material and an enhanced with high-resistivity float-zone silicon lense, achieve signal-to-noise ratios (SNRs) exceeding 60 dB at 0.5 THz, making them highly suitable for a range of ultrafast applications.

For visible light detection in pump-probe spectroscopy, New Focus 1801 photoreceivers with a 125 MHz bandwidth and a gain of 4×10^4 V/A are utilized, achieving a noise equivalent power (NEP) of $3.3 \text{ pW}/\sqrt{\text{Hz}}$. These photoreceivers enable real-time noise compensation and are sensitive to reflectivity changes as small as 10^{-6} .

A major challenge in ultrafast spectroscopy is detection of weak signals, often limited by background noise, particularly $1/f$ noise from laser intensity

fluctuations. A common approach to mitigating this noise is modulating the light source using a mechanical chopper or an acousto-optic modulator (AOM). The modulated signal is then processed via a lock-in amplifier, which isolates the reference frequency through phase-sensitive detection. AOMs, with modulation frequencies up to 250 kHz, provide superior SNR compared to mechanical choppers (typically operating in the kHz range) but at the cost of reduced laser power, as only one diffracted beam is utilized.

1.6 Outline of thesis



This flowchart illustrates the progression of this thesis. After the Introduction (Chap.1), where the motivation for the study was introduced, followed by an overview of the background on CMT materials and THz spintronics. Additionally, it covered the key technical aspects such as the pulse characterization of a Ti:Sapphire laser system and ultrafast signal detection, which was the key aspect to connect THz spintronic dynamics with material and device characterization. Next (Chap.2) we present state-of-the-art developments in THz spintronics and CdTe-based detectors, providing a comprehensive overview of the fundamental technologies, including THz radiation emission and detection, as well as development of CMT-based detectors. The next chapter, experimental approach, outlines the research methodology, emphasizing the THz time-domain spectroscopy (THz-TDS) system and techniques for the characterization of CMT materials and devices. Subsequently, we move to Chap.4, THz dynamics in spintronic and magnetic nanostructures, presenting experimental findings related to the emission mechanisms of FeCo/HM. This is followed in Chap.5, by a thorough examination of CMT materials and device characterization that covers essential topics such as charge transport measurements, bandgap characterization, and device fabrication. Finally, we conclude with (Chap.6) future work, which proposes new research directions, including the further exploration of CMT detector performance and the development of advanced techniques, such as electro-optic sampling.

Chapter 2

State-of-the-Art Developments in THz Spintronics and CdTe-Based detectors

2.1 THz radiation emission and detection

2.1.1 Introductions to THz radiation

The electromagnetic (EM) spectrum is commonly divided into two primary regions: radio frequency (RF) electronics and photonics, arranged by decreasing wavelength and increasing energy and frequency, as illustrated in Fig. 2.1 [26, 27]. RE electronics generally operates within the kHz to GHz range and is optimized for applications such as communications and wireless transmission systems. Specifically, RF (3 kHz–300 MHz) supports radio communications [28], while microwaves (300 MHz–300 GHz) enable technologies like satellite communications and radar [29].

In contrast, photonics encompasses higher frequencies, beginning with visible light (430 THz–750 THz), which powers technologies such as cameras and

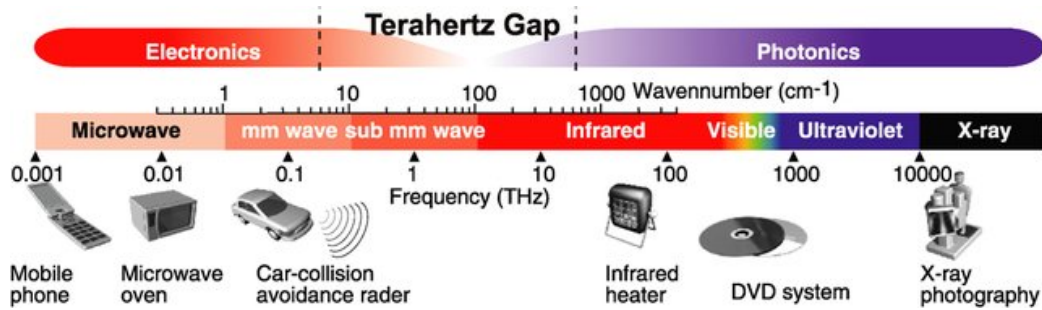


Figure 2.1: Terahertz gap in the electromagnetic spectrum [26]

televisions [30]. Ultraviolet (UV) radiation (750 THz–30 PHz) plays a critical role in photolithography and various industrial applications [31]. Furthermore, high-frequency ionizing radiation, including X-rays (30 PHz–30 EHz) and gamma rays (> 30 EHz), is essential in medical imaging techniques such as computed tomography (CT) and positron emission tomography (PET) [32, 33], despite their associated risks [34].

THz radiation, situated between the microwave and infrared regions of the electromagnetic spectrum (0.1–30 THz), is often referred to as the "THz gap" [26]. THz gap, long theorized, has only recently been explored due to limitations in electronics, including resistive losses, slow response, and photonic challenges like wavelength mismatch and inefficient sources [35, 36]. Recent advancements in THz science and technology have largely overcome these challenges. Innovations such as short carrier lifetime semiconductors, quantum cascade lasers, and ultrafast laser technologies have enabled efficient generation, detection, and manipulation of coherent THz waves [37, 38].

These breakthroughs have advanced both scientific research and prac-

tical applications. In non-destructive testing, THz waves enable material characterization and industrial quality control [39]. In security, THz radiation is extensively used in airport body scanners to detect concealed threats [40]. THz spectroscopy aids in identifying hazardous substances [41], while in medicine, THz imaging provides non-invasive diagnostic methods for skin cancer, burns, and wound healing [42, 43, 44]. Additionally, THz radiation is key in advancing ultra-fast 6G and satellite communications [45, 46].

2.1.2 Photoconductive antenna

Photoconductive (PC) antennas based on low-temperature-grown GaAs (LT-GaAs), are widely employed as emitters and detectors of THz EM pulses. The schematic of PC antennas is shown in Fig. 2.2. Each antenna consists of two metal electrodes placed on an LT-GaAs substrate, with a gap of approximately $10\ \mu\text{m}$. For emitters, the electrodes are arranged as parallel metallic stripes, while detectors utilize H-shaped structures with a $5\ \mu\text{m}$ gap (Fig. 2.2(b)) which ensures that the detector responds specifically to THz radiation polarized parallel to the two small notches.

When the emitter is excited by an ultrashort laser pulses, electron-hole pairs are generated within the LT-GaAs substrate. To achieve ultrafast detection, LT-GaAs is typically As rich and contains a large number of defects, resulting in a carrier lifetime of less than $150\ \text{fs}$ [47]. Due to a significantly higher mobility of electrons compared to holes, the contribution of holes to the current generation is negligible [48, 49]. The generated transient currents

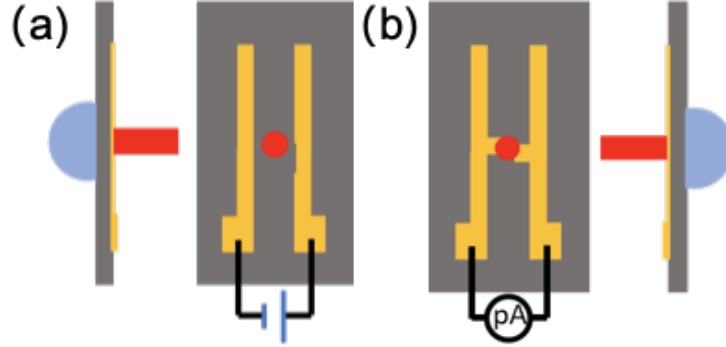


Figure 2.2: The photoconductive switch with a hemispherical Si lens used as a THz emitter (a) and as a THz detector (b). Dark parts represent the LT-GaAs substrate and red dots and lines represent a laser pulse focal spot and direction.

can be expressed by the following equation

$$J(t) = e N(t) \mu E_{\text{bias}}, \quad (2.1)$$

where $N(t)$ represents the density of states of photocarriers, which depends on both the laser pulse shape and the carrier lifetime of a given PC material [50, 42], e is the elementary charge, μ is the electron mobility, and E_{bias} is the external bias electric field.

The application of an external bias across the electrodes accelerates the transient photoelectrons, generating an ultrafast burst of electromagnetic (EM) radiation on the order of 1 ps [35, 51]. The resulting EM pulse, E_{THz} , can be expressed as

$$E_{\text{THz}} = \frac{A}{4\pi\epsilon_0 c^2 z} \frac{\partial N(t)}{\partial t} = \frac{Ae}{4\pi\epsilon_0 c^2 z} \frac{\partial N(t)}{\partial t} \mu E_{\text{bias}}, \quad (2.2)$$

where A is the area of the pump laser focal point, ϵ_0 is the vacuum permittivity, c is the speed of light, and z is the distance between the field point and the THz source, which is much greater than the dimensions of the PC antenna. The frequency spectrum of the emitted signal is broadband, extending into the THz region, with the polarization of the THz transients aligned parallel to the bias field. A silicon (Si) lens is attached to the rear of the LT-GaAs substrate to collimate the emitted THz radiation. As indicated by Eq. 2.2, the amplitude of the emitted THz transient increases with both the number of generated photoelectrons and the external bias. Therefore, the laser power and external bias are set to their maximum values without exceeding the GaAs breakdown threshold.

For detection, a picoammeter (pA meter) is connected to measure the current induced between the antenna contacts. Probe laser pulses are used to measure the dynamics of photocarriers between two small notches of the strip lines. The transient THz electric field accelerates these photocarriers, producing a pA-level current proportional to the THz field amplitude. A femtosecond-resolution delay stage is used to sample the THz waveform. The resulting current can be expressed as

$$\bar{I} = e\bar{n}_e E_{\text{THz}}(\tau_{\text{delay}}), \quad (2.3)$$

where \bar{n}_e represents the average electron density generated by the probe laser pulse, and $E_{\text{THz}}(\tau_{\text{delay}})$ denotes the THz electric field as a function of the time

delay between the THz and probe laser pulses.

2.1.3 Optical rectification

Another commonly used technique for THz generation and detection is a nonlinear optical process called optical rectification (OR). In the context of THz generation, an ultrafast laser pulse is directed onto a nonlinear optical crystal, such as ZnTe, LiTaO₃, CdTe, or BBO. The intense electric field of the femtosecond laser pulse interacts with the crystal, causing a rapid displacement of charge carriers within the material. This charge displacement results in the generation of a non-linear quasi-DC polarization, which is a defining characteristic of optical rectification [45]. Due to the oscillation of the optical electric field within the material, the induced nonlinear polarization produces a transient current that oscillates with a frequency spectrum extending into the THz range, thereby generating broadband THz radiation.

For THz detection, the reverse process of optical rectification occurs. When a THz pulse interacts with a nonlinear optical medium, it induces a time-varying polarization within the material, much like the generation process. In this case, the THz radiation modulates the electronic response of the crystal, leading to a shift in the material's polarization. To detect this shift, the crystal is illuminated by an optical probe pulse. The interaction between the THz field and the optical probe field induces a shift in the material's polarization. This shift can be detected as a change in the intensity of phase of optical signal [39, 42].

The detection of THz radiation is typically performed using a balanced detection scheme, where the change in the optical probe signal, due to the presence of the THz field, is monitored with high sensitivity. By adjusting the time delay between the optical probe and the THz pulse, the complete time-domain waveform of the THz signal can be reconstructed [52].

In both the generation and detection processes, phase matching is a crucial factor for ensuring high efficiency and coherence of the THz radiation. Phase matching ensures that the different wavevectors involved in the nonlinear interaction remain synchronized over the length of the nonlinear medium. This can be achieved through various techniques, such as optimizing the orientation of the nonlinear crystal or using quasi-phase matching (QPM) techniques, where the nonlinear properties of the material are periodically modulated to compensate for phase mismatch [53, 54].

2.1.4 Spintronic emission and detection

THz emission mechanisms mentioned previously utilize only the charge degree of freedom for electrons and not their spin degree of freedom [55]. THz spintronic emitters, which simultaneously manipulate both the charge and spin degrees of freedom of electrons, emerge as a new research direction, due to their numerous advantages such as, low cost, ultra-broadband emission, simplicity of use, and robustness [56].

The Inverse Spin Hall Effect (ISHE) is the core emission mechanism in THz spintronic emitters, where it facilitates the conversion of spin currents

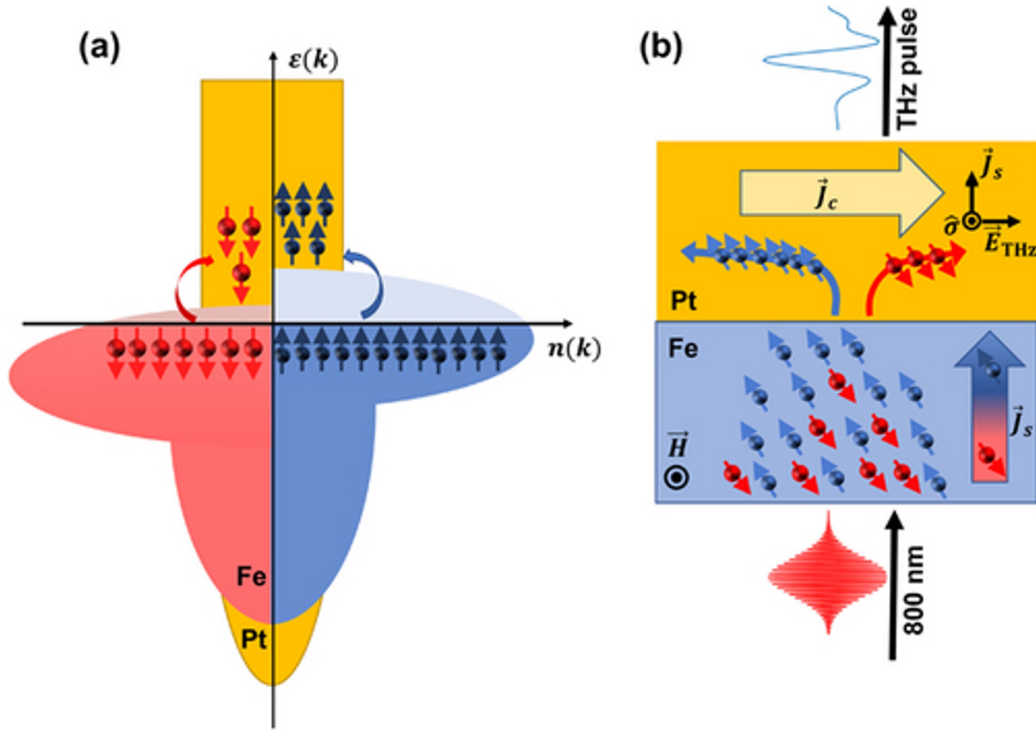


Figure 2.3: Conceptual overview of THz emission from spintronic devices. (a) Laser excitation of a magnetic material (e.g., Fe) creates more majority than minority spins. (b) The inverse spin Hall effect at the Fe/Pt interface induces a transient charge current, generating THz emission. The spin current \vec{J}_s propagates normal to the interface, and the charge current \vec{J}_c , generated by the inverse spin Hall effect, gives rise to a THz transient [56].

into charge currents, enabling efficient THz radiation generation. To understand the underlying physics of ISHE, it is essential to examine its relationship with the classical Hall effect and the Spin Hall Effect (SHE), both of which arise from charge carrier dynamics in response to external forces.

The Hall effect, first discovered by Edwin Hall in 1879, describes the generation of a transverse voltage in a conductor when an electric current flows

perpendicular to an applied magnetic field. This phenomenon arises due to the Lorentz force acting on charge carriers, leading to charge accumulation at the material's edges and the development of a measurable voltage difference. The Hall effect has been widely used for determining carrier densities and characterizing magnetic field properties in various materials [57].

In contrast, the Spin Hall Effect (SHE) is a consequence of spin-orbit coupling [58], where an electric current in a non-magnetic material generates a transverse spin current without the need for an external magnetic field. This leads to the accumulation of spin-polarized electrons at the edges of the material, allowing spin manipulation without ferromagnetic components. The SHE has significant implications for spintronic applications, including spin-based information storage and processing [59].

Furthermore, the Inverse Spin Hall Effect (ISHE) builds upon the principles of SHE, enabling the conversion of spin currents into charge currents. This conversion is fundamental to spintronic THz emitters, as it allows for the detection and utilization of spin accumulation in electronic and optoelectronic devices [60]. When a femtosecond laser pulse illuminates a ferromagnetic/heavy-metal (FM/HM) bilayer, majority (spin-up) electrons in the FM layer, such as Fe, Co, Ni, or their alloys, are excited to *sp*-states above the Fermi energy. These electrons possess longer mean free paths compared to minority (spin-down) electrons in *d*-states [61], as illustrated in Fig 2.3 (a) [62]. The decay time of minority spin electrons is shorter due to the hot Fermi-Dirac distribution, where a higher occupation of states re-

sults in reduced lifetimes. Heavy metals (HMs), such as Pt, Ir, Pd, or Au, are selected for spintronic emitters due to their large SOC. When optically excited spin-polarized electrons diffuse into the HM layer, spin-up and spin-down electrons move in opposite directions due to SOC [63]. This process generates a transient longitudinal spin current density, \vec{J}_s , which is converted into a transient transverse charge current density, \vec{J}_c , leading to the emission of an electromagnetic radiation pulse in the THz frequency range [64, 65], as depicted in Fig 2.3 (b). The relationship between \vec{J}_c and \vec{J}_s can be expressed as follow

$$\vec{J}_c = \frac{2e}{\hbar} \theta_{\text{SHE}} (\vec{J}_s \times \vec{\sigma}), \quad (2.4)$$

where e is the elementary charge, $\hbar = \frac{h}{2\pi}$ (with h being Planck's constant), θ_{SHE} is the spin Hall angle, and $\vec{\sigma}$ is the spin polarization vector [66, 67, 68]. The spin Hall angle, θ_{SHE} , which characterizes the efficiency of spin-to-charge conversion, is considered a key figure of merit in spintronic applications. Typically, heavy metals with high atomic numbers exhibit large θ_{SHE} : for example, $\theta_{\text{SHE}} = 0.12\text{--}0.15$ for Ta [69], $\theta_{\text{SHE}} = 0.3$ for W [70], $\theta_{\text{SHE}} = 0.01\text{--}0.02$ for Ir [71, 72], and $\theta_{\text{SHE}} \approx 0.03\text{--}0.05$ for Pt [73, 20].

In the past decade, significant progress has been made in THz spintronic emitters due to extensive scientific efforts. Beyond the spin Hall angle (θ_{SHE}) and spin diffusion length (λ_{sd}), parameters such as material composition [74], thickness of the nonmagnetic (NM) layer [75], wavelength of incident laser radiation [76], FM/HM interface properties [63], and FM/HM material com-

binations have been studied to enhance signal strength and broaden bandwidth.

It is essential to emphasize that all THz spintronic devices follow the same fundamental principle: a transient spin current is generated in the FM layer by an ultrafast laser pulse and is subsequently converted into a transient charge current at the FM/HM interface, resulting in THz emission. Recently, more precise physical mechanisms for spin-to-charge conversion have been explored. For example, two-dimensional electron gas (2DEG) systems, such as the surface/interface of topological insulators (TIs) or Rashba interfaces, are expected to achieve more efficient spin-to-charge conversion compared to HMs [77]. In these systems, effects analogous to the spin Hall and inverse spin Hall effects are referred to as the Rashba-Edelstein Effect (REE) and the Inverse Rashba-Edelstein Effect (IREE), respectively. Unlike bulk systems, where both intrinsic and extrinsic SHE can occur, REE is purely intrinsic.

Spin-to-charge and reverse charge-to-spin conversion in 2D systems are determined by the spin texture in k -space. For IREE, the injection of a 3D spin-polarized current into a 2D material creates an imbalance in charge carrier distribution, leading to a net 2D charge current. This relationship can be expressed as

$$\vec{j}_c = \lambda_{\text{IREE}} \vec{j}_s, \quad (2.5)$$

where λ_{IREE} is the inverse Rashba-Edelstein length [78, 79].

While most research in THz spintronics has primarily focused on THz

generation, recent studies have reported broadband spintronic detection of the absolute field strength of THz electromagnetic pulses. This detection is based on magneto-optic probing of the Zeeman torque exerted by the THz magnetic field on the magnetization of a ferromagnetic material [80], which opens up a new direction for high-sensitivity THz detection and field-strength measurements.

2.2 Development of CdTe-based detectors

2.2.1 Introduction to wide-range ultrafast detector

Radiation detectors based on semiconductors are designed to detect and measure electromagnetic radiation spanning from optical wavelengths to high-energy X and gamma rays and are used in a variety of applications such as medical imaging, security screening, material analysis, and astronomy [81]. The basic principle of operation of these detectors is the photoelectric effect [82]. When a photon of a sufficient energy (above the semiconductor energy gap) strikes a semiconductor material, it can dislodge an electron from its valence band, creating a hole in the process. The electron-hole pair can then contribute to a current flow in the semiconductor, which can be detected and measured. The design of semiconductor-based radiation detectors is dependent on the specific application and the wavelength range of interest. For optical detectors, materials such as silicon or gallium arsenide are commonly

used due to their high quantum efficiency and developed technology [83]. For X-ray detectors, materials such as cadmium telluride (CdTe), cadmium zinc telluride [(Cd,Zn)Te], and mercury iodide (HgI₂) are commonly used, due to their high atomic number, which enhances X-ray absorption [84]. An ultrafast photodetector is a type of photodetector that is designed to detect optical signals with extremely short durations, typically in the range of femtoseconds (10^{-15} s) to picoseconds (10^{-12} s). These detectors are used in a wide range of scientific and industrial applications, including ultrafast spectroscopy, laser diagnostics, and ultrahigh-speed telecommunications [85]. The most challenging part is detecting an optical signal with extremely short duration. The response time of the photodetector must be on the same order of magnitude determined, by the speed of electron-hole pairs recombination, or a transit time of the photocurrent. For example, some ultrafast photodetectors use semiconductors with high carrier mobility, such as GaAs or InGaAs, that in a low capacitance arrangement can achieve ultrafast response times [86]. Others may use specialized structures such as microchannel plates or avalanche photodiodes to achieve high sensitivity and low noise levels [87]. In addition to the fast response time, ultrafast photodetectors often have other key performance characteristics, such as high sensitivity, low noise, and high temporal resolution. The sensitivity of an ultrafast photodetector is controlled by the efficiency with which incident photons generate electron-hole pairs, while the noise level is determined by the level of unwanted electrical signals that are generated in the detector.

2.2.2 CMT detector incentives

The demand for wide-range ultrafast photodetectors has been increasing in recent years due to the growing need for high-speed and high-sensitivity detection of pulsed light across a broad range of wavelengths, especially from optical to X ray. This demand is being driven by the need for more convenient, more compact, more cost-effective photodetectors, instead of using multiple specialized detectors. However, few current commercially available photodetectors can do this job [88]. On one hand, ultrafast detectors such as InGaAs are available to cover the NIR range but not the X-ray-Visible wavelengths. On the other hand, Si-based photodetectors can cover X-ray-to-Visible range very well but have high leakage currents. Recently, HgPSe₃ single crystals has been mentioned as a new candidate for wide-range detectors, but their response time is in a second range, excluding ultrafast applications [89]. The Hamamatsu G4176-03 ultrafast metal-semiconductor-metal (MSM) photodetector, which is LT-GaAs-based (low temperature grown GaAs), was a potential solution; however, this device was recently discontinued. A replacement with equivalent or better performance than the Hamamatsu G4176-03 is thus needed, as currently called for by the market [90]. Similar to GaAs, Cd-MgTe is a wide-bandgap semiconductor with applications in optoelectronics and particle physics, including radiation detection (Bremsstrahlung, X-rays, gamma-rays, and thermal neutrons). (Cd,Mg)Te offers advantages over LT-GaAs, particularly in X-ray/optical cross-correlation. It achieves comparable or superior carrier lifetimes for both electrons and holes, with electron mo-

bility up to $1000 \text{ cm}^2/\text{V}\cdot\text{s}$ ($400 \text{ cm}^2/\text{V}\cdot\text{s}$ for LT-GaAs). CdMgTe's electron lifetime ranges from 0.1 ns for ultrafast applications to 1 μs for spectroscopy-grade materials, while LT-GaAs has an electron lifetime of 0.1 μs . CdMgTe also exhibits lower leakage current due to its wider bandgap. So here, I propose the ternary semiconductor material, CMT as a very promising candidate as a dual optical/x-ray ultrafast detector.

2.2.3 CMT material background

Cadmium telluride (CdTe) is a binary $A_{II}B_{VI}$ direct bandgap semiconductor known for its unique physical and electronic properties. CdTe crystallizes in a non-centrosymmetric zinc blend structure (face-centered cubic), characterized by 43-point group symmetry. With a bandgap of approximately 1.5 eV at 300 K, CdTe is widely employed in thin-film solar cells due to its low cost, high absorption coefficient, and scalability [91]. Moreover, its bandgap can be tailored by alloying with elements such as mercury, zinc, manganese, or magnesium, broadening its applications in photovoltaics, radiation detection, and optoelectronics.

For example, alloying CdTe with mercury (HgCdTe) produces a versatile material for infrared detection [92], while combining it with zinc is used as a solid-state detector for X-rays and gamma rays due to its high atomic number. Currently, cadmium zinc telluride (CdZnTe) is commercially utilized in advanced photon-counting computed tomography (PCCT) systems, providing superior visualization of small structures and improved tissue char-

acterization compared to conventional CT [93]. CdZnTe also finds extensive applications globally in security screening, nondestructive industrial imaging, and aerospace technologies [1]. My research focused on the ternary alloy cadmium magnesium telluride (CdMgTe), which is considered 'specially engineered' because, unlike other tunable ternary compounds where the constituent concentration is typically restricted to a narrow range (no more than 20%), Cd_{1-x}Mg_xTe can be grown with x values as high as 0.5. This remarkable flexibility is due to very similar crystalline structures of both CdTe and MgTe crystals and allows Cd_{1-x}Mg_xTe to accommodate a wide range of applications. For example, x can be tuned below 0.1 for ultra-fast timing applications or increased to 0.4 to 0.5 for scintillator, optoelectronic and THz applications [90].

2.2.4 CMT Performance for Nuclear Detection Applications

The response of CMT crystals with varying dimensions to different nuclear sources is presented in this section. The crystals were processed and experiments were finished at Brimrose Co. The thickness and electron lifetime of the material can be adjusted to meet the specific requirements of various nuclear applications.

All samples utilized in previous studies exhibited short carrier lifetimes, essential for picosecond timing responses in femtosecond laser and X-ray experiments. By fine-tuning the material properties to achieve a slightly

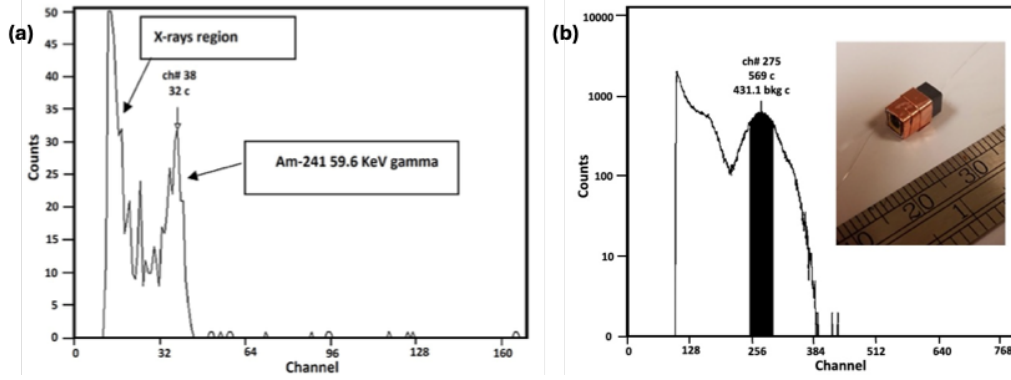


Figure 2.4: (a) Room-temperature response of a $9 \times 7 \times 1.5\text{-mm}^3$ pseudo-hemispherical $\text{Cd}_{1-x}\text{Mg}_x\text{Te}$ detector at 450 V to an Am-241 gamma source, demonstrating an energy resolution of 7% at 60 keV. (b) Cs-137 (662 keV) gamma response of a $4.5 \times 4.5 \times 9\text{-mm}^3$ $\text{Cd}_{1-x}\text{Mg}_x\text{Te}$ detector in a Frisch-Grid configuration (see inset).

longer electron lifetime and, consequently, a higher $\mu\tau_e$ product, the energy resolution of the nuclear spectral responses improves [90].

For Am-241 gamma source detection, the CMT crystal thickness was adjusted to 1.5 mm and shaped into a pseudo-hemispherical geometry. The hard X-ray component of the source is distinctly observed in Fig. 2.4 (a), demonstrating a 7% energy resolution at 60-keV gamma rays. In the case of Cs-137 (662 keV) detection, shown in Fig. 2.4 (b), the crystal thickness was increased to 9 mm to enhance its ability to withstand higher radiation levels. Additionally, the CMT crystal was encapsulated in a Frisch-grid configuration to optimize charge collection efficiency. These results underscore the potential of CMT crystals as promising candidates for high-performance nuclear radiation measurements.

Chapter 3

Experimental approach

This chapter outlined the experimental techniques employed to investigate ultrafast optical and electronic properties. For THz spintronics studies, terahertz time-domain spectroscopy (THz-TDS) was employed, and low-temperature measurements enabled temperature-dependent investigations. For ultrafast detector studies, pump-probe spectroscopy was utilized to examine carrier dynamics, while a dedicated device characterization setup facilitated ultrafast photoconductivity measurements. Together, these methodologies establish a robust framework for advancing the understanding of ultrafast optoelectronic and THz phenomena.

3.1 Terahertz time-domain spectroscopy (THz-TDS) system

Terahertz time-domain spectroscopy (THz-TDS) is a powerful technique for investigating the optical and electronic properties of materials in the THz

frequency range. By generating and detecting short THz pulses, THz-TDS enables time-resolved measurements with high spectral resolution and sensitivity. In this work, a custom-built THz-TDS system was designed and implemented to characterize the dynamic response of the studied samples under controlled experimental conditions. The setup incorporates a femtosecond laser source, optical and mechanical components for beam manipulation, temperature control and a photoconductive antenna for THz detection. The details of the system configuration and operation are described below.

3.1.1 THz time-domain system

A specialized THz-TDS system was designed for our experiments, as illustrated in Fig. 3.1. The system employs a commercial Ti:sapphire laser (MIRA900) to generate a train of nominally 100-fs laser pulses, centered at an 800-nm wavelength with a repetition rate of 76 MHz. To mitigate potential interference, a Faraday isolator is positioned at the laser cavity output. A polarizing beam splitter is utilized to precisely control the power distribution between the pump and probe beams, typically maintaining a 90:10 power ratio. The lower-power branch (probe beam) is directed onto a LT-GaAs photoconductive antenna, which serves as a THz transient detector (Teravil Co.) [94]. A pre-amplifier is integrated between the detector and the lock-in amplifier to enhance and record the amplitude of the detected THz transients.

The high-power branch (pump beam) first reflects from a retroreflector

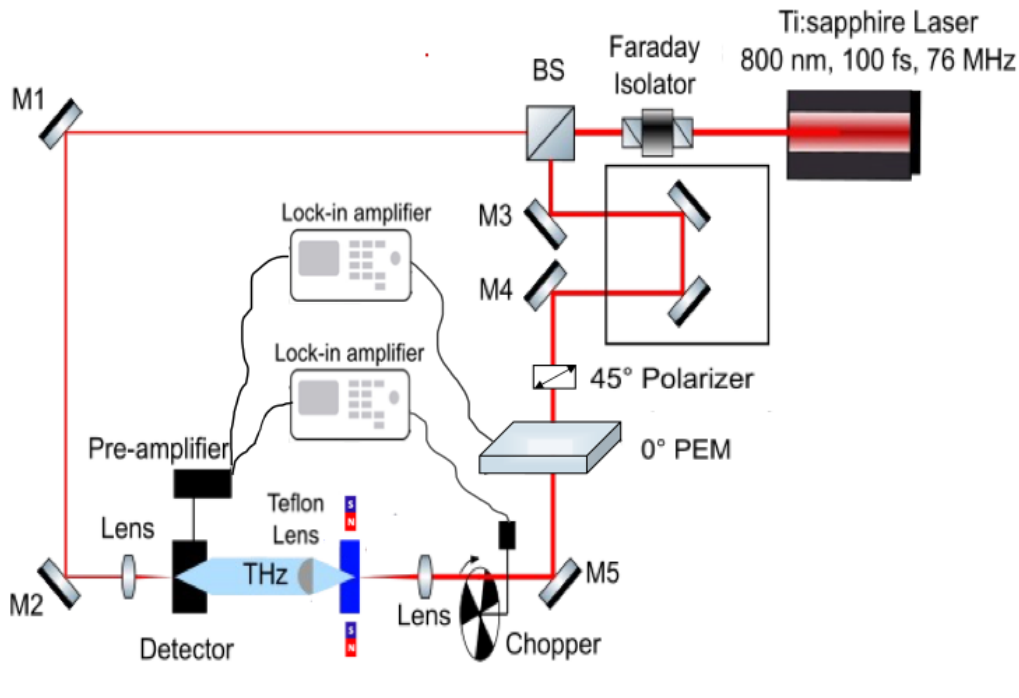


Figure 3.1: Schematic of the THz time-domain measurement setup. BS denotes the beam splitter, while M1–M4 represent four dielectric mirrors. The two magnets indicate the coil used to generate an external magnetic field. PEM refers to the photoelastic modulator

mounted on a delay stage before passing through a 45-degree polarizer and two modulators: a photoelastic modulator (PEM) with a quartz optical head (HINDS Instruments) and an optical chopper. The system resolution is determined by the Newport delay stage, which can be adjusted with a step size as small as $2.5 \mu\text{m}$, corresponding to an optical path delay of 16.6 fs. Additionally, a Teflon (polytetrafluoroethylene) lens with a 5-mm diameter and a 10-mm focal length is employed to collimate the emitted THz radiation. A tunable external magnetic field of up to 140 kA/m is applied using

electromagnet coils wrapped around iron yokes.

Two modulators are incorporated into the pump beam path to accommodate different experimental requirements. For conventional THz-TDS measurements, a mechanical chopper is employed for intensity-modulated experiments. In this configuration, the 45-degree polarizer is removed, and the PEM is turned off, allowing the pump beam to pass through the quartz optical head with approximately 95% transmission. If higher power is required, the PEM can be entirely removed without affecting the light polarization. The mechanical chopper operates at a frequency of 2 kHz and serves as a reference for the lock-in amplifier. Finally, the pump beam is focused onto the sample at normal incidence, resulting in a fluence of approximately $330 \mu\text{J}/\text{cm}^2$ at the sample plane.

Conversely, when the PEM is activated, the chopper is turned off, allowing the beam to pass through the gaps between the chopper blades. The quartz optical head of the PEM undergoes mechanical stress via compression or stretching, inducing birefringence. This effect causes different linear polarization components of the light to propagate at varying speeds through the quartz, generating a phase difference known as retardation. A specific condition arises when linearly polarized light, oriented at 45 degrees to the optical axis, propagates through the quartz with a retardation set to $\lambda/4$. In this scenario, the PEM functions as an oscillating quarter-wave plate, causing the polarization to oscillate between right-handed and left-handed circular polarization. The oscillation frequency is 50 kHz, dictated by the quartz

material of the PEM's optical head. By activating the PEM and applying a 50-kHz modulation signal, polarization modulation of the light is achieved.

3.1.2 Low temperature measurements

A liquid-nitrogen-cooled optical cryostat (Janis VPF-100) is employed for low-temperature measurements, with a cross-sectional view illustrated in Fig. 3.2. The samples are mounted on a Cu cold finger, which is directly attached to a nitrogen reservoir, ensuring efficient thermal contact and rapid cooling. A pair of permanent magnets is fixed to the cold finger, generating a constant magnetic field of approximately 230 kA/m, which is sufficient to ensure that all tested samples remain in a fully saturated magnetic state throughout the experiments [95].

To precisely monitor the sample temperature, a temperature sensor is positioned adjacent to the sample, providing real-time measurements. Temperature regulation is achieved using a heater, allowing for adjustments within a broad range from 60 K to 450 K. By actively pumping nitrogen vapor, the boiling temperature of liquid nitrogen can be slightly reduced below 77 K, enabling more precise control over the lower temperature range.

Before conducting the actual measurements, the transparency of the cryostat's optical silica windows in the THz spectral range was thoroughly examined to ensure minimal signal distortion. Experimental validation confirmed that the windows exhibit negligible THz attenuation, making them well-suited for the intended measurements.

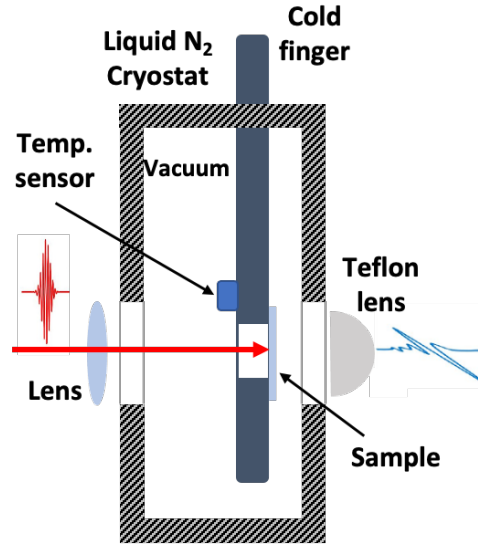


Figure 3.2: Cross-section of the cryostat with a spintronic emitter operated at variable temperatures

3.2 CdMgTe materials and device characterization methods

3.2.1 Pump-probe spectroscopy

Optical pump-probe spectroscopy is a well-established and powerful technique for characterizing the carrier dynamics of materials by monitoring transient changes in reflectivity or transmissivity of materials [96, 97, 98]. For all CMT-related measurements, especially for CMT materials characterization, a single-color configuration is employed.

As illustrated in Fig. 3.3, optical pulses generated by the same commercial Ti:sapphire laser are split into two beams using a 90/10 beam splitter. This

approach mitigates jitter issues, as both beams originate from a single source. Unlike the THz-TDS setup, the pump and probe beams in this configuration are focused on the same spot of the sample. The pump beam excites the semiconductor sample, generating photocarriers, while the probe beam monitors the temporal evolution of these photocarriers. The laser energy is set near or above the sample's bandgap, enabling the pump beam to excite electrons from the valence band to the conduction band. This process induces a transient change in the material's optical properties, including reflectivity and transmissivity, caused by phonon or thermal relaxation and electron-phonon interactions [99, 100, 101]. The probe beam, with significantly lower power, is directed at the sample to detect pump-induced changes by collecting reflected or transmitted light. These changes are typically small, with reflectivity or transmissivity variations on the order of 10^{-6} to 10^{-4} .

To ensure that only the optically excited region of the sample is probed, the probe beam diameter ($\sim 20 \mu\text{m}$) is kept slightly smaller than the pump beam diameter ($\sim 30 \mu\text{m}$). The probe beam, after reflecting off the surface or passing through the sample, is detected by a photodetector connected to a lock-in amplifier. To capture the complete transient response, synchronization between the pump and probe beams is systematically varied using a computer-controlled delay stage in the probe beam path. By extending the sampling path, the ultrafast sampling pulse is delayed relative to the excitation pulse.

The polarizations of the pump and probe beams are set orthogonal to

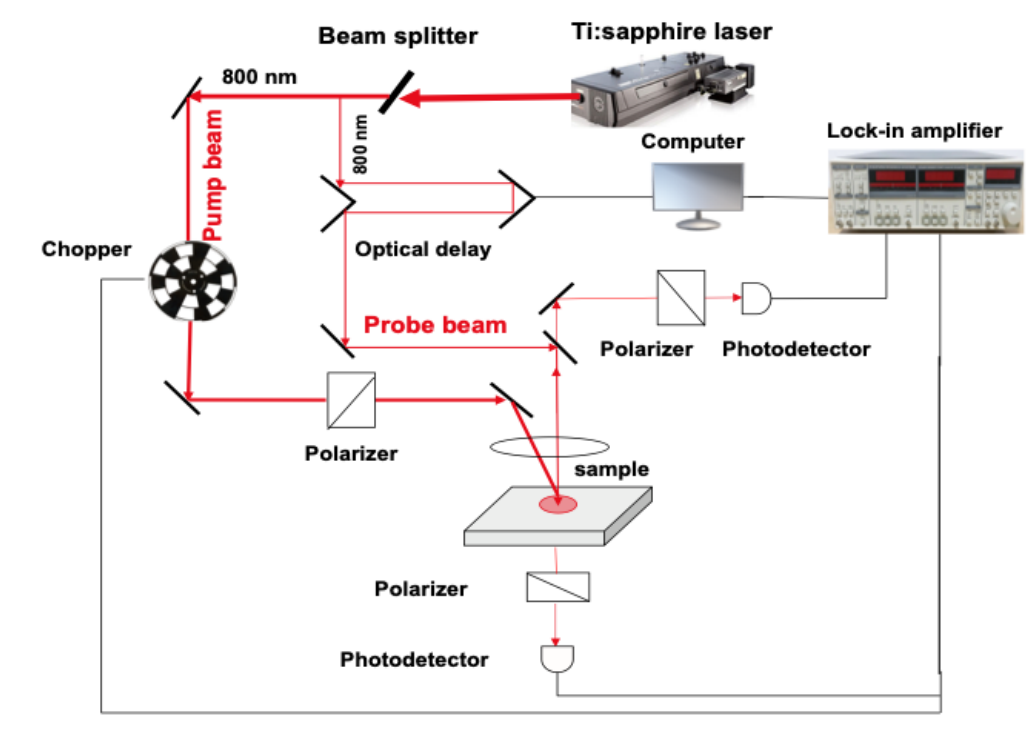


Figure 3.3: Configuration for pump probe spectroscopy which could measure both reflectivity or transmissivity variations

eliminate coherent artifacts [102]. This is achieved by passing the probe beam through a half-wave plate, oriented 90° out of phase with the pump beam. A polarizer placed in front of the photodetector ensures that only the probe beam is detected, preventing interference from the pump beam. The lock-in amplifiers, digital multimeters, delay stage, and photodetectors are interconnected via a GPIB interface and controlled using a LabVIEW program.

3.2.2 Device measurements

The Ti:sapphire laser power is attenuated to a desirable level using a neutral density filter (not shown in the diagram) to ensure precise control over the excitation intensity. To achieve uniform light intensity distribution over the photodetectors, the laser beam is focused to a spot diameter of approximately $100\ \mu\text{m}$. This precise focusing enables efficient coupling of the laser energy to the active region of the device. Fig. 3.4 illustrates the experimental setup, with a zoomed-in view showing the diagram of the CMT device [103].

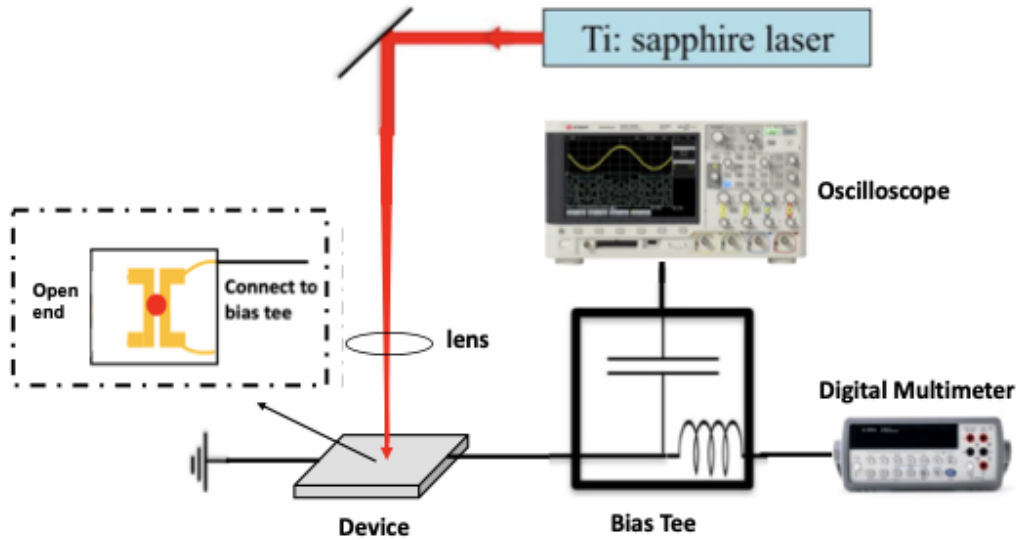


Figure 3.4: Diagram of experimental setup for device photoresponse measurements

The device configuration includes one end connected to a bias Tee, which serves a dual purpose: simultaneously applying a DC bias to the sample and facilitating the readout of high-frequency photoresponse signals. The bias

Tee ensures stable operation and effective separation of the DC and high-frequency components. All other ends are in connection with the ground to eliminate potential hazards caused by photocurrent.

Chapter 4

Dynamics of THz Spintronics in Various Systems

4.1 Sample fabrication and characterization

All FeCo-based spintronic samples were fabricated at the Institute of Physics, Polish Academy of Sciences, Warsaw, Poland, and thin-film graphene was produced in the Belarusian State University of Informatics and Radioelectronics, Minsk, Belarus.

4.1.1 Thin films fabrication

The fabrication process started with $10 \times 10 \text{ mm}^2$ MgO crystals with a (100) surface orientation were used as substrates. FeCo films were grown under ultra-high vacuum conditions (1×10^{-10} Torr) using a molecular beam epitaxy (MBE) system. A $\text{Fe}_{50}\text{Co}_{50}$ layer was deposited via co-evaporation, employing a cobalt (Co) e-beam gun and an iron (Fe) effusion cell.

To complete the structure, a 3-nm-thick Ir or Pt layers were deposited on top of the FeCo layer using an e-beam gun. The quality of the entire structure was monitored and controlled through reflection high-energy electron diffraction (RHEED) and a flux detector.

4.1.2 Graphene synthesis and characterization

Graphene was grown in a custom quartz tube reactor (inner diameter: 14 mm) on 25 μm thick Cu foil (99.9%, Alfa Cesar). Before synthesis, a Cu foil was electrochemically polished in 1 M orthophosphoric acid for 5 minutes at 2.3 V and annealed in an Ar/H₂ mixture (100 cm³/min and 60 cm³/min) at 1050°C for 60 minutes. Methane (1.3 cm³/min) was introduced for 30 minutes while reducing H₂ flow to 6 cm³/min. After synthesis, the sample was cooled at 50°C/min rate, and an unwanted graphene on the foil's backside was removed with the oxygen plasma. The Cu foil was dissolved in FeCl₃ solution, and the graphene film was washed in distilled water before its transfer onto the FeCo surface. Details of the synthesis and transfer process are available in [104].

To preserve the integrity of polycrystalline CVD graphene, its transfer to the target surface was assisted by a PMMA polymer layer. Removing this layer required physical and chemical treatments, often involving elevated temperatures that could affect the FeCo properties, particularly at the interface. To minimize such effects, few-layer graphene was synthesized to maintain its integrity during wet transfer.

The transferred graphene was characterized using Raman spectroscopy

with a Confotec NR500 scanning confocal microscope (spectral resolution $< 3 \text{ cm}^{-1}$). Raman spectra were recorded under ambient conditions using a 488 nm (2.54 eV) laser over a $30 \times 30 \mu\text{m}^2$ area with 30×30 points. Typical spectra of single- and few-layer graphene are shown in Figs. 4.1 (a) and (b). A noticeable D band was observed in single-layer graphene with an I_D/I_G ratio of ~ 0.75 . The G band intensity ratio between single- and few-layer graphene (~ 4) indicates that the few-layer graphene corresponds to four layers [105].

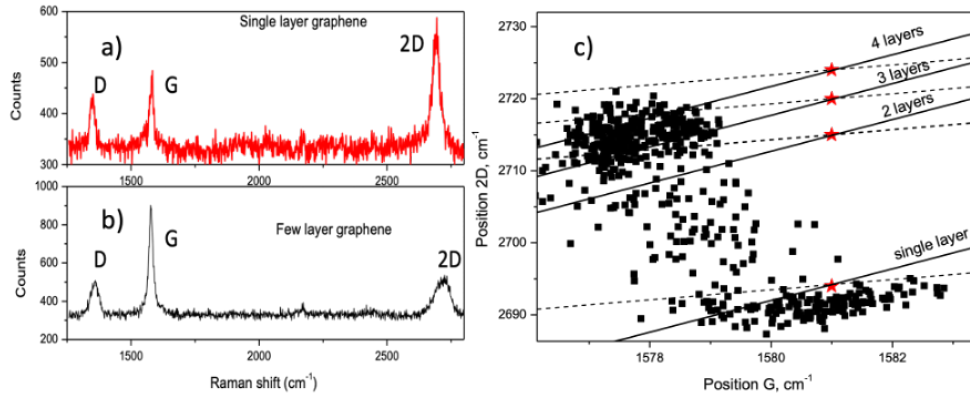


Figure 4.1: Typical Raman spectra of single-layer (a) and few-layer (b) graphene, and the 2D band position as a function of the G band position (c). Stars indicate positions of unstrained, undoped graphene for 1- to 4-layer graphene. The bold solid line (slope 2.2) represents biaxial strain variation, while dashed lines (slope 0.7) indicate charge carrier concentration variation.

Fig. 4.1 (c) shows the correlation between 2D and G band positions [106], revealing strain and doping effects. Single-layer graphene was nearly unstrained and lightly *p*-doped [107], while a four-layer graphene exhibited a

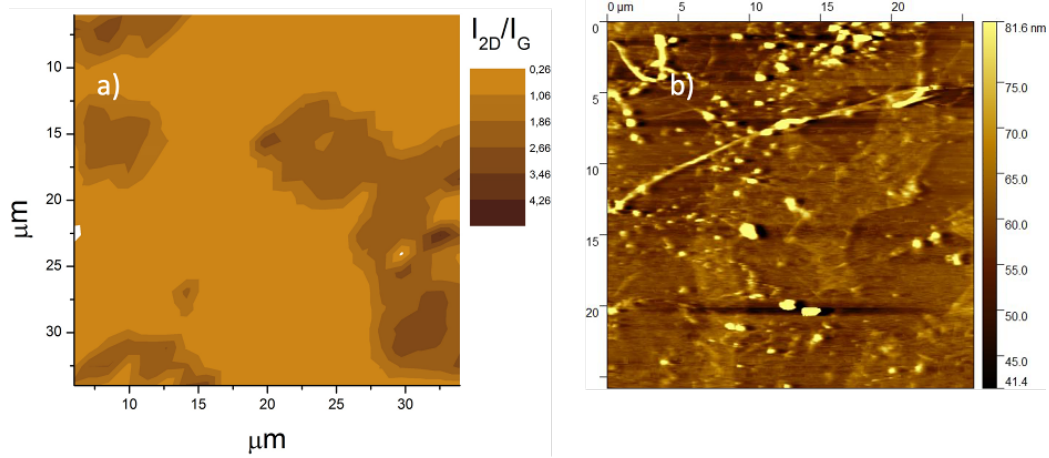


Figure 4.2: Maps of the I_{2D}/I_G intensity ratio and the morphology of graphene transferred onto the MgO/FeCo structure. The maps represent measurements taken from different regions of the sample.

tensile strain. Spatial distributions of the single- and few-layer graphene are also shown in Fig. 4.1 (c), where the lower I_{2D}/I_G ratio indicates a thicker graphene [108].

Figure. 4.2 presents maps of the I_{2D}/I_G intensity ratio and the graphene morphology on the MgO/FeCo structure respectively. The morphology correlates well with the I_{2D}/I_G map, demonstrating uniform graphene coverage across the sample.

The structure and quality of the graphene-FeCo interface were further investigated using high-resolution transmission electron microscopy (HRTEM) at the Institute of Microelectronics and Photonics in Warsaw, Poland. The HRTEM image, shown in Fig. 4.3, confirms the epitaxial growth of the FeCo film with a thickness of 6 nm. A three-layer graphene structure is observed on top of the FeCo film, consistent with the results from Raman spectroscopy.

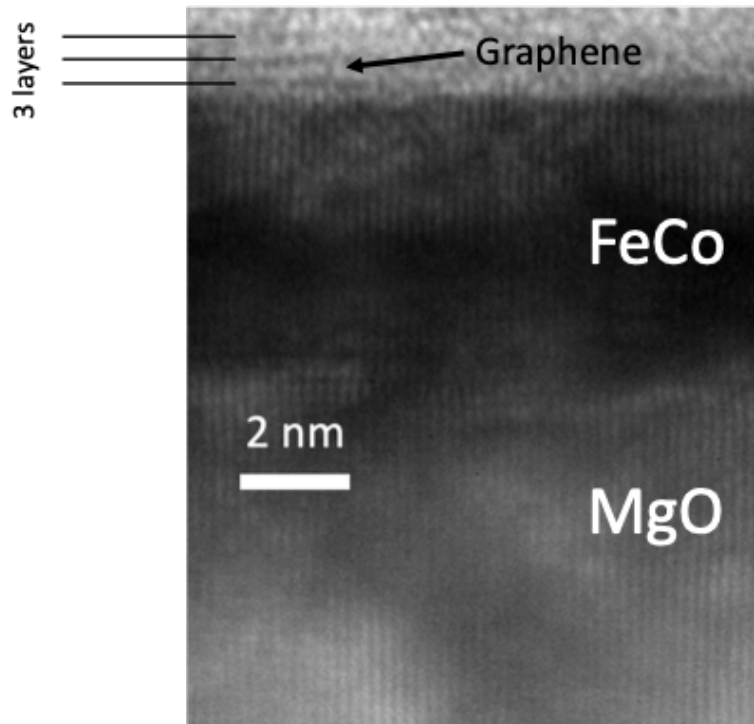


Figure 4.3: High resolution TEM image of a MgO/FeCo (6 nm)/graphene sample with 2 nm resolution bar

Spacing between the graphene layers was measured to be approximately 0.33 nm, which agrees well with the standard interlayer spacing for graphite. Notably, no significant native oxide formation was detected at the FeCo/graphene interface. However, the possibility of partial oxidation of FeCo cannot be entirely excluded, as oxidation could occur through grain boundaries, defects, or discontinuities in the graphene layer.

4.2 Generation mechanisms of FeCo/graphene heterostructure

4.2.1 Emission layer

The generation mechanisms of THz transients in FeCo/graphene heterostructures are discussed in this section. Fig.4.4 (a) (black curve) presents a high-amplitude, time-domain electromagnetic transient recorded from a FeCo/graphene sample after illumination by Ti:Sapphire laser pulses in reverse geometry. Details about the experimental setup were provided in Section 3.1.1.

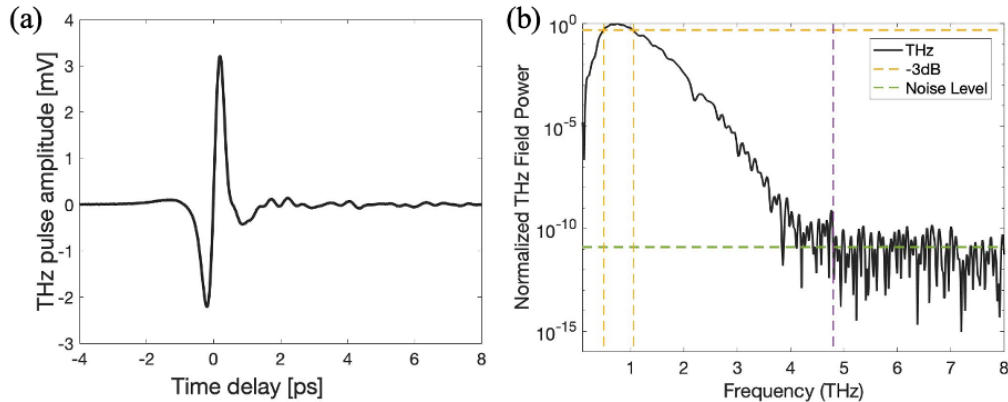


Figure 4.4: THz emission from FeCo/graphene nano bilayer. (a) THz transients emitted from FeCo/Graphene bilayer. (b) The power spectrum of the experimental waveform.

The corresponding power spectrum, obtained via the fast Fourier transform of the experimental waveform, is shown in Fig. 4.4 (b). The spectrum bandwidth extends up to 4.7 THz, with a 3-dB cutoff at 1.1 THz.

A simplified interpretation suggests that the THz generation originates from the FeCo/graphene bilayer. However, the presence of an oxide layer cannot be entirely excluded, even though no such layer was observed in the HRTEM images. To further clarify this, THz generation from a bare FeCo film had been analyzed.

To account for various scenarios, two additional samples were fabricated: a protected FeCo with MgO and a non-protected FeCo, denoted as FeCo(6 nm) / MgO(2 nm) and FeCo(6 nm), respectively. In the former case, a 2-nm-thick MgO cap layer was grown *in situ* to prevent the formation of a native FeCo oxide.

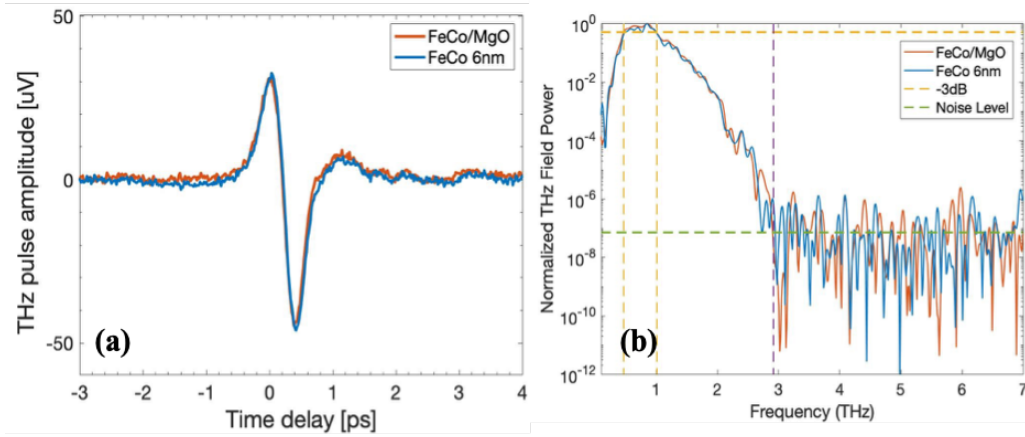


Figure 4.5: (a) THz emission from a FeCo/MgO nanobilayer (orange) and a pure FeCo layer (blue). (b) Corresponding THz power spectra of experimental waveforms.

Figure 4.5 (a) and (b), identical THz pulses with the same spectra. They were observed from both the protected and non-protected FeCo samples. This result indicates that the transients generated by FeCo are negligible

when compared to the THz pulses emitted by the FeCo/graphene bilayer, which exhibit peak-to-peak amplitudes in the mV range under identical experimental conditions.

The latter confirms the direct role of graphene in THz generation within the FeCo/graphene nanobilayer, while excluding the pure FeCo and the FeCo oxide interface contributions from our consideration.

4.2.2 Main emission mechanism

Notably, the presence of graphene on top of a FeCo layer leads to strong THz signal generation, highlighting the inverse Rashba-Edelstein effect (IREE), or the more general inverse spin Hall effect (ISHE), as the most plausible mechanism. A convenient way to distinguish ISHE from other mechanisms is to verify whether the THz signal depends on the direction and strength of the magnetization \mathbf{M} of the FM layer.

Figure 4.6 (a) presents THz signals recorded from a FeCo/graphene sample excited from either the graphene side (front, black curve) or the substrate side (back, red curve). According to Eq. (2.4), the charge current density \mathbf{j}_C is proportional to the vector product of $\boldsymbol{\sigma}$ (the spin polarization direction related to \mathbf{M} and \mathbf{j}_S), which flows towards the FM/graphene interface.

When the external magnetic field remains unchanged, irradiating the sample from opposite sides changes the direction of both spin and charge currents, resulting in a sign reversal of the THz waveform. This behavior, as observed experimentally in Figure 4.6 (a), confirming the IREE/ISHE mech-

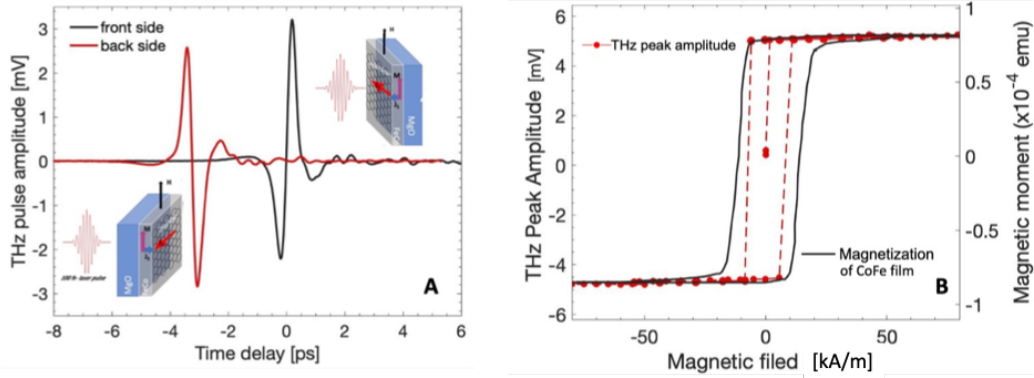


Figure 4.6: Evaluation of the mechanism of THz generation in the FeCo/graphene nanobilayer. (a) THz transients emitted from the sample under excitation from opposite directions. (b) Magnetization (black curve) and the amplitude of the THz signal (red dashed line) as functions of the external magnetic field. Both the magnetic moment and THz peak amplitude curves were normalized at 50 kA/m to enable direct comparison.

anism. The THz transient generated by front-side irradiation (red curve) has an opposite phase compared to the back-side irradiation (blue curve).

By contrast, flipping a pure FeCo samples (with or without graphene protection) does not alter the sign of the emitted THz transient, indicating that THz generation in these samples arises from the fast demagnetization process in the FeCo layer [56]. This distinction reinforces the pivotal role of graphene in the THz emission from FeCo/graphene bilayers. Furthermore, since the amplitude of the THz signal is proportional to the rate of change of \mathbf{j}_C , it correlates directly with the magnetization of the sample. Experimental results, shown in Figure 4.6 (b), further validate this relationship, providing additional evidence for the IREE/ ISHE mechanism. A slight narrowing of the THz amplitude hysteresis loop as compared to the $M(H)$ hysteresis, is

attributed to the laser-induced local heating effect.

4.2.3 Evaluation of Inverse Rashba-Edelstein Length

As discussed in Chapter.2.1.4, the spin Hall angle θ_{SHE} or λ_{IREE} serves as a figure of merit for the ISHE or IREE effect responsibly. Estimating this parameter from a THz signal requires knowledge of \mathbf{j}_S , precise THz detector calibration, and consideration of experimental subtleties. However, a rough estimate can be made by comparing the FeCo/graphene signal with that of a FeCo/heavy-metal (HM) bilayer, where θ_{SHE} of the HM is known. For this purpose, a FeCo (6 nm)/Ir (3 nm) bilayer was tested, as θ_{SHE} for Ir is well known and equal $\sim 0.01\text{--}0.02$ [71, 72]. Signals recorded from FeCo/Ir and FeCo/graphene samples under identical experimental conditions are shown in Figure 4.7. The most striking result is the opposite sign of the THz transient emitted by the FeCo/graphene bilayer, as compared to FeCo/Ir.

The direction of \mathbf{j}_C in graphene enables a qualitative understanding of the spin texture in the graphene conduction band, associated with IREE. To induce \mathbf{j}_C in the observed direction (Fig. 4.7 b), the outer Fermi contour must shift oppositely. This shift implies that for injected electrons with spins polarized parallel to \mathbf{M} , the spin texture of the outer (inner) contour should exhibit clockwise (counterclockwise) helicity. The latter reasoning applies strictly to the single-layer graphene (SLG). However, the inclusion of few-layer graphene (FLG) should not qualitatively alter the picture.

From the ratio of signal amplitudes, for FeCo/Ir and FeCo/graphene sam-

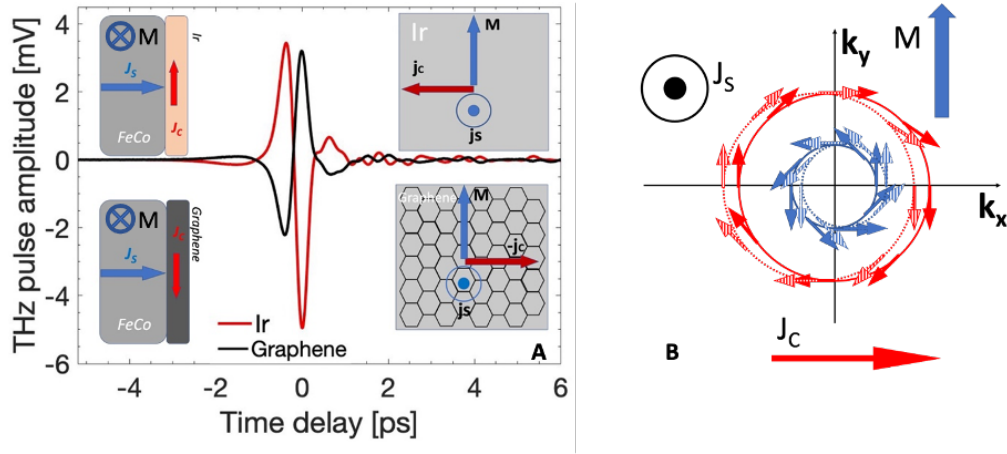


Figure 4.7: Evaluation of inverse Rashba-Edelstein length of graphene and Rashba spin texture (a) THz waveforms for FeCo/Ir (red) and FeCo/graphene (black) nanobilayers, recorded under the same experimental conditions. The insets show the mutual orientations of j_s , j_C , and M based on the value of θ_{SHE} for Ir (b) Fermi contours for minority (blue) and majority (red) spins in graphene conducting band. Dashed contours correspond to the shifted Fermi contours due to injection of spin polarized (spins parallel to M) electrons.

ples, $8 \text{ mV}/5 \text{ mV} = 1.6$, the θ_{SHE} for graphene can be estimated to be 0.0063–0.0125. In 2D systems, the 3D charge current density \mathbf{j}_C (units: A/cm^3) can be converted to a 2D current density \mathbf{j}_{2D} (units: A/cm^2). Thus, the ratio $\mathbf{j}_C/\mathbf{j}_s$ has the dimension of length, and is called the IREE length λ_{IREE} .

The 2D charge current density integrated over the thickness of the non-magnetic layer is given by:

$$\mathbf{j}_C = \theta_{SHE} \lambda_{sf} \tanh\left(\frac{t}{2\lambda_{sf}}\right) \mathbf{j}_s,$$

where λ_{sf} and t are the spin diffusion length and layer thickness, respectively.

For a few-layer graphene, where $t \ll \lambda_{\text{sf}}$, this simplifies to:

$$\mathbf{j}_C = \frac{1}{2}\theta_{\text{SHE}}t\mathbf{j}_S,$$

Combining these equations yields:

$$\lambda_{\text{IREE}} = \frac{1}{2}\theta_{\text{SHE}}t,$$

Considering graphene thicknesses to be in the range 0.3–1 nm, λ_{IREE} is evaluated to be $0.9\text{--}6.3 \times 10^{-3}$ nm, consistent with the $\sim 10^{-3}$ nm value obtained from spin-pump experiments for the graphene/YIG system [109].

In conclusion, a few-layer, CVD-grown graphene atop a 6-nm-thick epitaxial FeCo film generates strong THz transients when excited by fs laser pulses. The phase dependency of the transients on experimental geometry and the correlation of THz amplitude with $M(H)$ hysteresis highlight the role of IREE in THz generation. Comparison with FeCo/Ir bilayers enables estimation of the IREE length, confirming that graphene's spin-orbit coupling is significantly enhanced by proximity to the FM layer. This enhancement facilitates ultrafast spin-to-charge current conversion in graphene, paving the way for numerous applications.

4.3 Circular Photogalvanic Effect

The injection of spin current into materials with Rashba spin texture is not the only mechanism to induce charge current. The transfer of photon angular momentum to electrons can lead to a non-equilibrium distribution of photoexcited electrons in the momentum space, resulting in a nonzero spin current. This phenomenon is commonly referred to as the Circular Photogalvanic Effect (CPGE) [110]. The CPGE obeys optical selection rules, making the generated current dependent on the helicity of the excitation light.

CPGE has been observed in transition metal dichalcogenides [111], topological insulators [111, 112], and Weyl semimetals [110]. Depending on the material, CPGE can arise from interband or intraband transitions. The photon energy used in our experiment (~ 1.54 eV) suggests that interband transitions dominate in graphene, leading to the generation of electron-hole pairs. For ideal graphene, CPGE should result in zero net charge current due to electron-hole symmetry, where electron and hole currents cancel each other. However, non-idealities (e.g., defects) in graphene typically break this symmetry [113, 114], resulting in a nonzero CPGE current generated via valence-conduction interband transitions.

When CPGE is triggered by femtosecond pulses, it should emit THz bursts. Under circularly polarized excitation light, the charge current generated in graphene on FeCo has two components: one originating from the inverse Rashba-Edelstein effect (IREE) and the other from CPGE. These

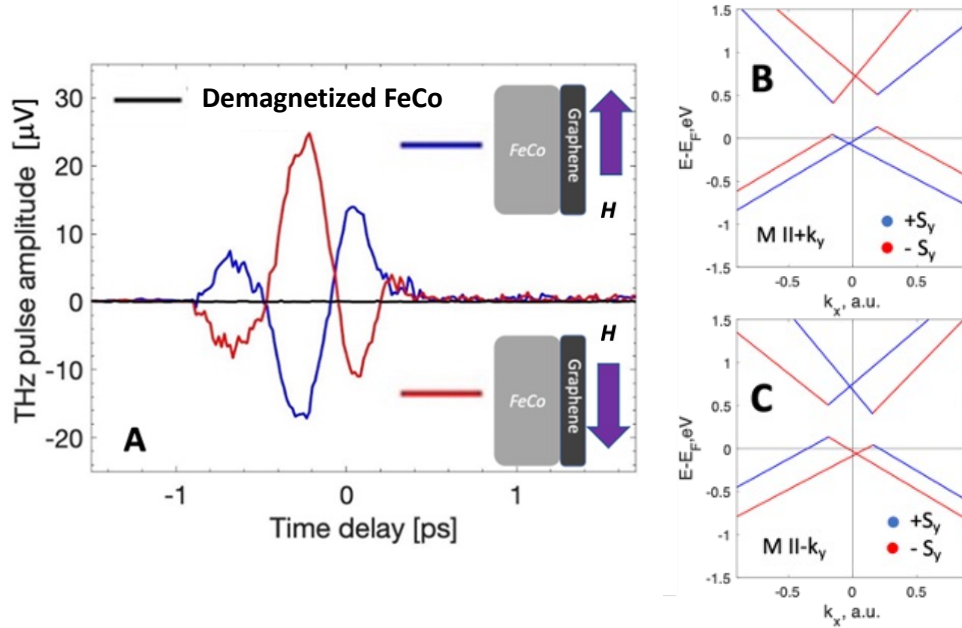


Figure 4.8: (a) THz transients recorded using a photoelastic modulator for two opposite directions of FeCo/graphene magnetization (blue and red) and a demagnetized sample (black). (b) and (c) The scheme of the graphene band diagram with SOC and exchange interaction included for an external magnetic moment parallel, $M \parallel +k_y$ (b), and antiparallel $M \parallel -k_y$ (c). Blue and red correspond to the orientations of the spins (S_y), parallel (blue) and antiparallel (red) to k_y . The presented dispersions are expressly distorted to clearly demonstrate the discussed effects.

components may add to or subtract from each other, depending on the light helicity. To isolate the CPGE component in our measurements, a photoelastic modulator (PEM) was employed to modulate the laser light polarization. During half of the modulation period, the light is right-circularly polarized (σ^+), and during the other half, it is left-circularly polarized (σ^-). Detailed information on the measurement scheme is provided in Chapter 3.1.1. The

THz transients corresponding to CPGE are presented in Fig. 4.8 (a). The signals were recorded for two opposite orientations of the FeCo film magnetization and for a fully demagnetized FeCo film.

We first emphasize that the waveform and amplitude of the PEM - modulated signal are distinct from those recorded using mechanically chopped modulation (see Fig. 4.4), confirming the different origin of the IREE and CPGE signals in our experiments. Additionally, the CPGE signal polarity depends on the magnetization direction, and the signal vanishes when the sample is demagnetized.

To explain this behavior, it is necessary to review the band structure of graphene. Previous models include only spin-orbit coupling (SOC), which would not exhibit magnetization dependency. However, proximity to ferromagnetic (FM) layer can induce strong exchange interactions in graphene-based materials [115, 116, 117]. This exchange field significantly modifies the structure of the graphene band, making it dependent on the magnetization direction. In Figs. 4.8(b) and 4.8(c), we illustrate the schematic band diagram of single-layer graphene for magnetic moments parallel and antiparallel to the \mathbf{k}_y -momentum direction, where both SOC and exchange interactions are considered. This scheme adopts the calculated band diagram from [115].

Circularly polarized light drives transitions obeying optical selection rules, requiring a total angular momentum change of $\Delta J = \pm 1$. In graphene, where conduction and valence bands are formed by $2p_z$ orbitals, there is no change in orbital momentum ($\Delta L = 0$). Thus, circularly polarized light induces

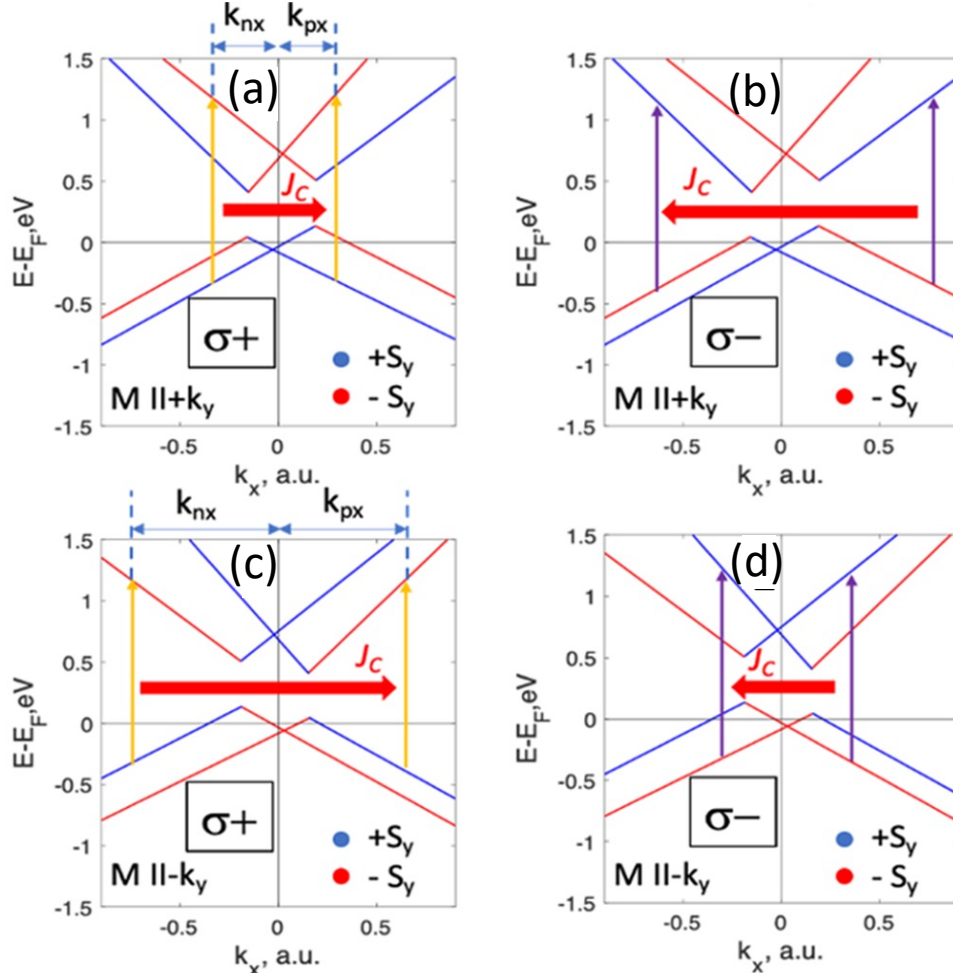


Figure 4.9: (a) and (b) show the allowed transitions for right-hand circularly polarized light, for $M \parallel +k_y$ and $M \parallel -k_y$, respectively. (c) and (d) show the allowed transitions for left-hand circularly polarized light, for $M \parallel +k_y$ and $M \parallel -k_y$, respectively. The thick red arrows represent the generated charge currents. The longer arrows correspond to larger currents.

spin-flip transitions ($\Delta S = \pm 1$) between the conduction and valence bands, as shown by the “red” and “blue” lines.

Fig. 4.9 (a) illustrates the transitions induced by σ^+ -polarized light. Although electrons excited by σ^+ light occupy states in the inner contour of the conduction band with opposite momentum directions, a non-zero charge current is generated due to momentum asymmetry ($k_{p_x} \neq k_{n_x}$), resulting from the peculiar structure of the graphene band, which includes both SOC and exchange interactions. Reversing the magnetization inverts the spin polarization direction for conduction and valence bands. However, the direction of current flow remains the same, while the magnitude of the generated current increases due to coupling with the outer contour under σ^+ light, as shown in Fig. 4.9 (b). Switching the light polarization from σ^+ to σ^- reverses the described current flow patterns, as illustrated in Figs. 4.9 (c)-(d).

The proposed model explains the dependence of the photogenerated current on magnetization and light polarization, consistent with experimental observations. The mechanism of momentum asymmetry in k -space assumes that interband transitions induced by circularly polarized light occur only between states with opposite spin directions. Although some studies [118] suggest transitions within the same $2p_z$ orbitals without spin flipping, the latter would only reverse the current direction while preserving the overall reasoning. The absence of signal for demagnetized films is attributed to the laser beam size ($\sim 100 \mu\text{m}$), which exceeds the FeCo domain size [119]. Consequently, CPGE signals generated in graphene over domains with opposite

orientations cancel each other.

4.4 Spin texture of a single-layer graphene

Our findings highlight the necessity of including exchange interactions in the analysis. The exchange coupling modifies the spin texture, as illustrated in Fig. 4.10. However, even with this modification, vertically aligned spin injection would generate currents in the same direction as presented in Fig. 4.7. Precise evaluation of spin arrangement in the studied system requires knowledge of SOC and exchange field values, necessitating further experiments.

The spin textures illustrate how the spins align along the field, which represents a superposition of the effective SOC field, B_{SO} (locked to the linear momentum of electrons, k), and the exchange field, B_{exch} . Fig. 4.10 (a) depicts the spin texture of graphene with SOC when the strength of the exchange field (B_{exch}) is comparable to the strength of the effective SOC field (B_{SO}). Fig. 4.10 (b) illustrates the spin texture for the case where $B_{\text{exch}} \gg B_{\text{SO}}$.

Although the spin texture in Fig. 4.10 (a) is notably different from the texture with zero exchange field, it leads to the same physical consequences. Specifically, spin-up-polarized electrons injected from the FeCo layer (J_s) will occupy states on the left side of the outer contour (dashed line), causing a shift and generating a charge current in the same direction as discussed in the main text.

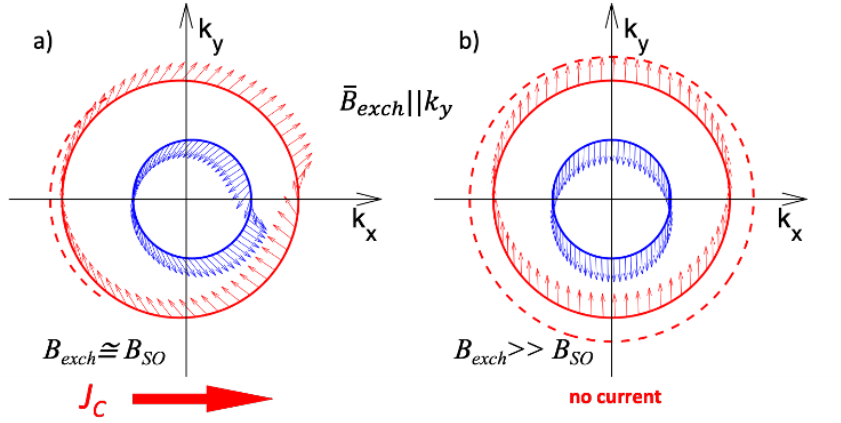


Figure 4.10: Spin texture of single layer graphene when both spin-orbit coupling and exchange energies are presented

In contrast, when B_{exch} dominates over B_{SO} (Fig. 4.10 (b)), the situation resembles Zeeman splitting. In this case, the injected spin-up-polarized electrons are uniformly distributed along the outer contour, resulting in no charge current generation.

Based on physical considerations, the Zeeman energy in FeCo (~ 2.5 kG) corresponds to ~ 250 μeV , about five times greater than graphene's intrinsic SOC energy (≤ 50 μeV) [120]. The exchange energy induced in graphene by proximity to Co(0001) layers is estimated at ~ 175 meV [115], though this may be overestimated due to differences in sample preparation and interface quality. For graphene decorated with ferromagnetic nanoparticles, the exchange energy was estimated to be 30 – 50 meV using the Klinovaja-Loss (KL) model [121, 122]. Since our experiments were conducted at room temperature, the SOC energy must exceed 26 meV, consistent with literature

values of 13 – 100 meV [120, 123, 124, 125, 126, 127].

4.5 Temperature-dependent THz transients in weakly remnant Py nanolayers

A schematic diagram of our THz temperature measurement setup is presented in Chapter 3.1.2. Independently, temperature-dependent magnetization measurements were conducted using a Superconducting Quantum Interference Device (SQUID) Magnetic Property Measurement System (MPMS).

The THz transient amplitude, A_{THz} (left y-axis), as a function of the magnitude of the in-plane magnetic field H for a Py/Pt sample is recorded and presented in Fig. 4.11). The external magnetic field H was varied from +70 to -70 kA/m. For each value of H , THz transients were recorded. The experiments were conducted in both direct and reverse illumination geometries, with the corresponding $A_{\text{THz}}(H)$ dependences shown as red and blue dots respectively [95].

As previously discussed, due to the reversed direction of the charge current J_c when the sample is flipped into the direct geometry, the $A_{\text{THz}}(H)$ dependence (red circles in Fig. 4.11) is also inverted compared to the blue circles. Additionally, Fig. 4.11) also depicts the magnetization $M(H)$ (right y-axis) dependence on the in-plane magnetic field H for a Py nanolayer (black line) measured by MPMS. By appropriately scaling the y-axes, excellent overlap between $A_{\text{THz}}(H)$ and $M(H)$ can be achieved while maintaining

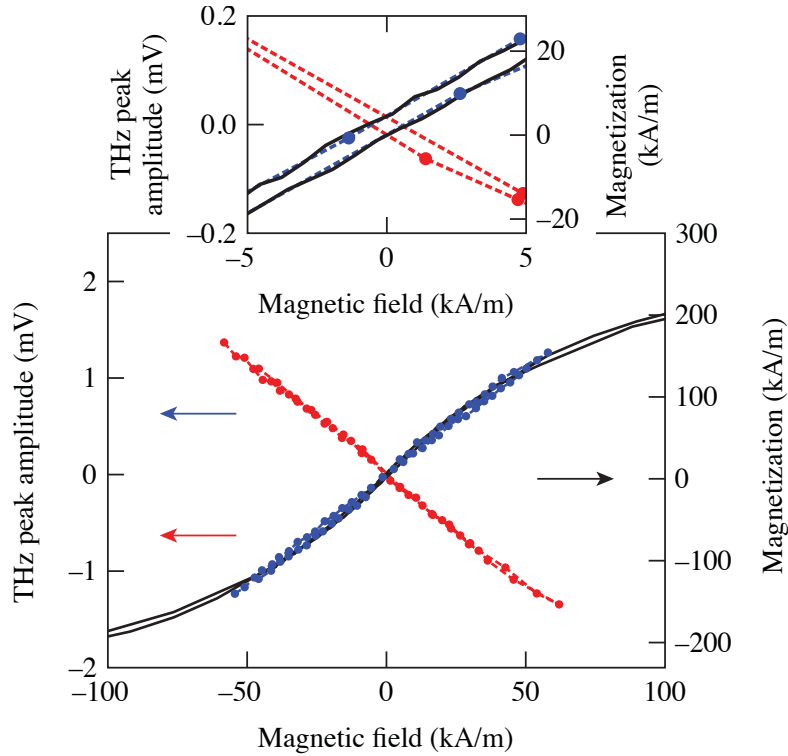


Figure 4.11: THz amplitudes, $A_{\text{THz}}(H)$ (left y-axis; red and blue dots), and magnetization, $M(H)$ (right y-axis; black solid line), of a Py/Pt bilayer as a function of the external magnetic field H . The inset provides a magnified view of the region near the origin for better visualization of fine details.

their original physical units (mV and kA/m, respectively). The inset provides a magnified view of the region near the origin, highlighting the narrow hysteretic curves of Py and demonstrating the perfect overlap of $A_{\text{THz}}(H)$ and $M(H)$. The magnetic susceptibility is estimated as $\chi = 3$ which also confirms that weak remnant of Py nanolayers.

The black curve in Fig. 4.12(a) represents temperature-dependent magnetization measurements obtained using a MPMS, indicating that the Curie

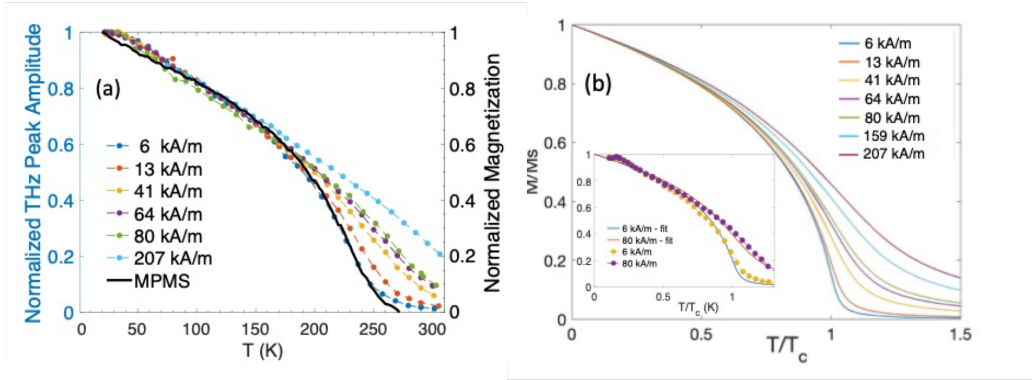


Figure 4.12: (a) $A_{\text{THz}}(T)$ of a Py/Pt sample as a function of reduced temperature (T/T_C) under different B_{ext} , with the black curve representing MPMS magnetization measurements. (b) qualitative fitting of relative magnetization versus reduced temperature, with the inset comparing relative magnetization and normalized THz peak amplitude.

temperature of Py/Pt is approximately 270 K. Additionally, Fig. 4.12(a) illustrates the THz amplitude, $A_{\text{THz}}(T)$, of a Py/Pt sample as a function of the reduced temperature (T/T_C) under different external magnetic field values. The observed increase in the tails of $A_{\text{THz}}(T)$ with the amplitude of B_{ext} aligns with mean-field theory [128]. The temperature dependence of $M(H)$ is estimated by averaging all possible alignments of the magnetic moment \mathbf{M} with respect to the effective field \mathbf{H}_{eff} , weighted by a Boltzmann factor, as expressed in Eq. 4.1

$$\frac{M}{M_S} = B_J \left(\frac{3J}{J+1} \cdot \frac{M}{M_S} \cdot \frac{T_C}{T} \right), \quad (4.1)$$

where $B_J(y)$ is the Brillouin function. In the classical limit, $J \rightarrow \infty$, $B_J(y)$

approaches the Langevin function, as demonstrated in Eq. 4.2

$$B_J(y) = \coth(y) - \frac{1}{y}, \quad (4.2)$$

$$M = M_{int} + M_{ext} \quad (M_{ext} = \chi H). \quad (4.3)$$

Qualitative fitting results are presented in Fig. 4.12 (b), where the fitted magnetic susceptibility parameter aligns with the MPMS values. The inset provides a comparative analysis between the relative magnetization and the normalized THz peak amplitude, showing a strong correlation. The spin current is influenced by the demagnetization rate of the ferromagnet [129]. As T approaches the Curie temperature of the Py/Pt sample, where the ferromagnet undergoes a magnetic phase transition, a significant magnetization change with temperature governs the generation of THz transients. These results reinforce the connection between magnetization dynamics and THz emission characteristics in the Py/Pt system.

4.6 Terahertz Emission from Tunneling FeCo/MgO/Pt Spintronic Heterostructures

MgO, a wide-bandgap insulator, serves as a tunnel barrier in ferromagnet-heavy metal (FM/HM) bilayer nanostructure. The MgO crystalline structure and its compatibility with ferromagnetic materials facilitates not only their epitaxial growth on top of the FM layer, but also high spin polarization, and

remarkable tunneling magnetoresistance effects [130]. We report here our studies of transient THz emission studies from a FeCo/MgO/Pt heterostructure emitter, paving the way for the advancement of the next-generation of highly efficient THz spintronic emitters.

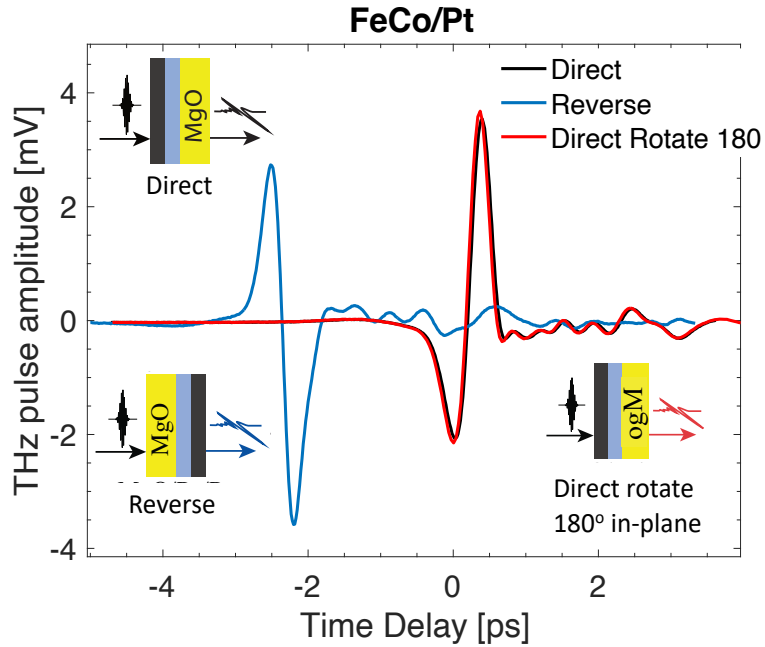


Figure 4.13: Time-domain THz transients measured from a 6-nm FeCo/4-nm Pt bilayer in the direct (black), reverse (blue), and 180° in-plane rotation (red) geometries. The bilayer orientation is depicted in the inset.

The experimental setup for THz time-resolved spectroscopy (THz-TDS) measurements is described in Chapter 3.1.1. An external magnetic field of up to 200 kA/m is applied to ensure that all magnetic moments within the ferromagnetic FeCo are aligned in the same direction. Fig. 4.13 presents time-domain electromagnetic transients emitted by a FeCo/Pt reference sample

under pulsed light illumination in three geometries: direct, reverse, and in-plane rotation by 180° , as indicated in the inset by black, blue, and red arrows. The THz transients measured from both the direct and in-plane rotation configurations are identical and consistent, again, with the expected the inverse spin Hall effect [95] both the spin current and spin polarization remain unchanged.

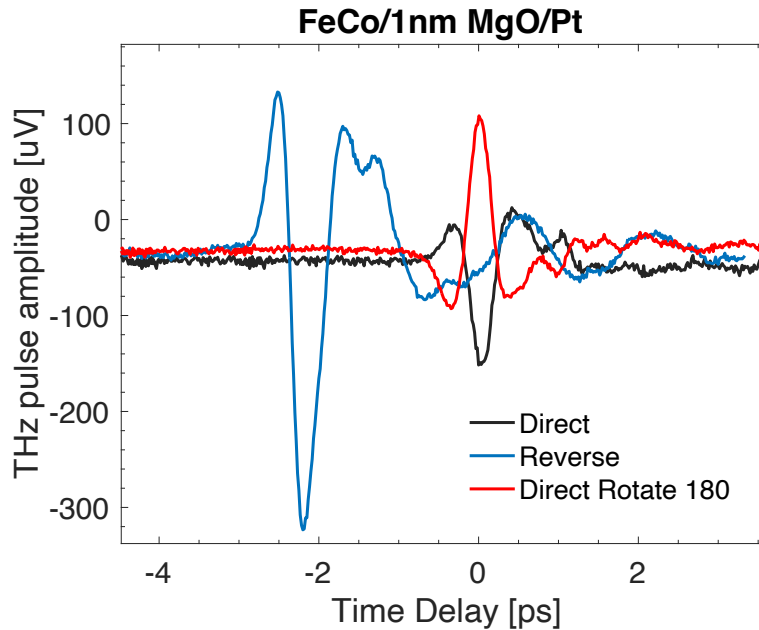


Figure 4.14: THz-TDS transients measured from a 6-nm FeCo/1-nm MgO/4-nm Pt trilayer in the same geometry.

In Fig.4.13 and 4.14, the THz transients from both the direct and reverse configurations are identical but exhibit opposite signs. This behavior arises because flipping the sample reverses the spin current direction, leading to an inverted THz signal [64]. However, an anomalous THz response was ob-

served in the case of the FeCo/1-nm MgO/Pt sample. As shown in Fig.4.14, reversing the sample resulted in a significant increase in the THz transient amplitude while maintaining the same sign.

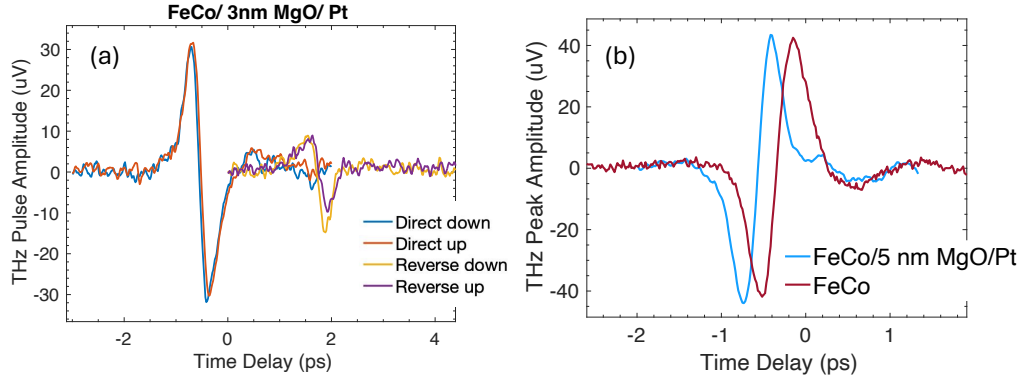


Figure 4.15: Enter Caption

Furthermore, a comparison between the signals measured in the direct configuration and those obtained after an in-plane rotation revealed identical amplitudes but opposite signs. A similar behavior was observed in the FeCo/2 nm-MgO/Pt sample. Notably, the amplitude of THz signals from the FeCo/MgO/Pt samples are significantly lower than that from a simple FeCo/Pt bilayer. However, it remains considerably higher than that of a pure FeCo sample under identical experimental conditions, indicating that demagnetization is not the predominant mechanism in the tunneling FeCo/MgO (1 nm and 2 nm)/Pt samples.

For FeCo/MgO (3, 4, 5 nm)/Pt samples, rotating the sample in-plane does not reverse the signals, as shown in Fig.4.15(a). Furthermore, when the samples are flipped, the signal remains unchanged, which excludes the

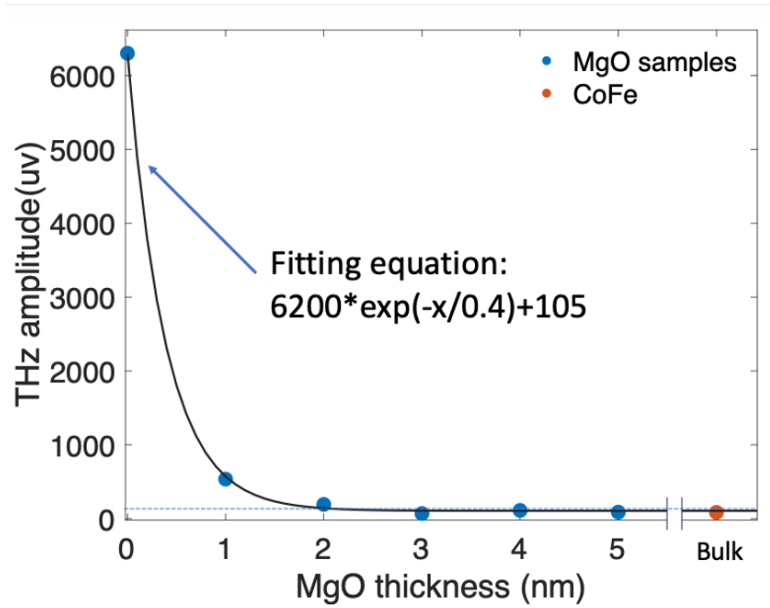


Figure 4.16: Enter Caption

contribution of ISHE. The signals obtained in the direct configuration are notably smaller than those from the reverse configuration because the MgO substrate absorbs THz waves. A comparison of the signals from CoFe and FeCo/5-nm-MgO/Pt, presented in Fig. 4.15 (b), shows identical characteristics, suggesting that the observed signals arise from demagnetization in the thicker spacer samples.

The THz peak-to-peak results for all FeCo/MgO/Pt samples, as well as FeCo and FeCo/Pt, are recorded and presented in Fig. 4.16. These results are fitted using a similar single-exponential decay, as described by the Eq. 5.12. Here, rather than interpreting τ as the carrier decay time, we define it as the spin diffusion time, which is 0.4 nm.

To gain deeper insights into the emission mechanism in the tunneling sample, polarization-sensitive detection was conducted [95]. A custom-designed sample holder was employed, allowing two external permanent magnets (200 kA/m) to rotate in-plane together with the sample, with a rotation accuracy of approximately 10° . The triangular notches of the LT-GaAs detector antenna in our setup were aligned vertically, as illustrated in the inset of Fig. 4.17. The dependence of the detector signal on the sample angle was measured for both FeCo/Pt and FeCo/MgO/Pt samples.

For the FeCo/Pt emitter, the maximum signals were observed at $\phi = 0^\circ/180^\circ$, while minimal signals, as expected, were detected at $\phi = 90^\circ/270^\circ$, since the emitted THz transients are polarized orthogonally to the direction of the applied magnetic field [95]. In contrast, for the FeCo/1 nm MgO/Pt emitter, the maximum signals were shifted to $\phi = 150^\circ/330^\circ$, with minima at $\phi = 60^\circ/240^\circ$. Similarly, for the FeCo/2 nm MgO/Pt emitter, the maximum signals were shifted to $\phi = 80^\circ/260^\circ$, with minima at $\phi = 170^\circ/350^\circ$. However, for FeCo, FeCo/3 nm MgO/Pt, FeCo/4 nm MgO/Pt, and FeCo/5 nm MgO/Pt, the maximum signals returned to $\phi = 0^\circ/180^\circ$.

The primary assumption is that the MgO spacer alters the spin polarization. These shifts observed in the 1 nm and 2 nm MgO spacer samples indicate that the detected THz polarization is rotated, which may explain the unusual behavior observed in Fig. 4.14. This effect arises because the detector signals are proportional to the projection of the THz radiation's electric field vector onto the axis defined by the detector's triangular notches. Start-

ing from the 3 nm MgO spacer, we believe the spacer becomes too thick, effectively blocking spin tunneling. As a result, Pt is completely decoupled from the FeCo layer, and the observed signal originates from demagnetization effects. This assumption is consistent with the data presented in Fig. 4.14. However, a more detailed explanation requires further experimental investigation.

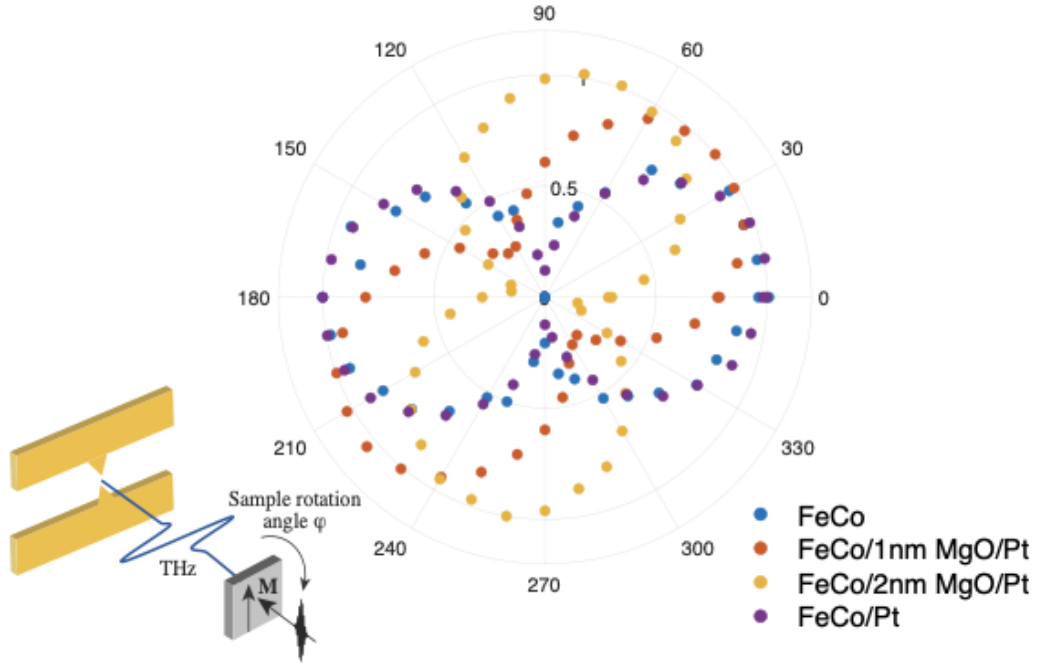


Figure 4.17: Angular dependence of a normalized signal for FeCo/Pt and FeCo/MgO/Pt samples. The $\mu = 0$ case corresponds to the sample/detector configuration shown in the inset

Chapter 5

CdMgTe materials and device characterization

This section presents the measurements conducted on bare CMT crystals to ensure an accurate evaluation of their intrinsic properties, focusing on optimizing the material composition and doping parameters to achieve the desired ultrafast photodetection performance. Subsequently, details about device fabrication and characterization under application-specific conditions will be provided, offering a comprehensive discussion of the fabrication methodologies and evaluation processes while highlighting the devices' performance in real-world scenarios.

5.1 Crystal growth

The CMT crystals used in this work were grown by our main collaborator and the project sponsor, Brimrose Co. Brimrose has developed an innovative procedure for purification of magnesium to the highest achievable level. This

proprietary technique involves sublimation of Mg under dynamic vacuum. The process uses two ampoules– a pyrolytic boron nitride (pBN) ampoule that is placed inside the second ampoule, which is a graphitized fused silica ampoule with length slightly longer than the pBN ampoule. Thus, Mg (in the molten or vapor phase) is prevented from reacting with the fused outer silica ampoule, which is connected to the high vacuum system [3][4].

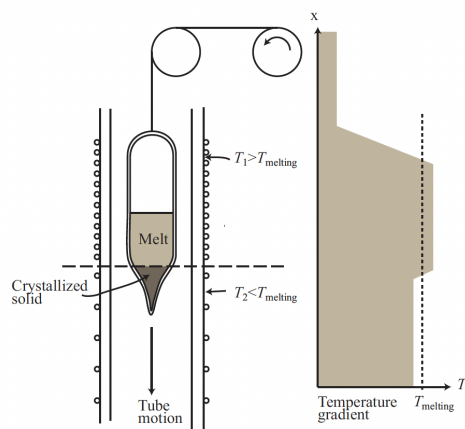


Figure 5.1: Schematic diagram of the Vertical Bridgman method.

To synthesize high-quality CMT ingots with low defects and homogeneous stoichiometry, three essential steps are required: compounding, the Bridgman technique, and zone-melting refining. Raw CdTe and MgTe components are synthesized separately from high-purity elements (6N for Cd and Te, 5N for Mg), and then mixed in precise amounts to achieve the desired composition of the source material. A vertical, three-heat-zone tubular furnace is employed to combine the binary components as Fig.5.1 presented [2]. This method offers advantages because the upper heater, which maintains a temperature

higher than the melting point, facilitates the variation of vapor pressure. Meanwhile, the middle heater creates a narrow liquid zone of tellurium that dilutes the polycrystalline ingot to saturation. The lower heater, operating at a lower temperature, establishes the temperature gradient for growth, with the growth rate being controlled by the speed at which the ampoule is lowered through the furnace.

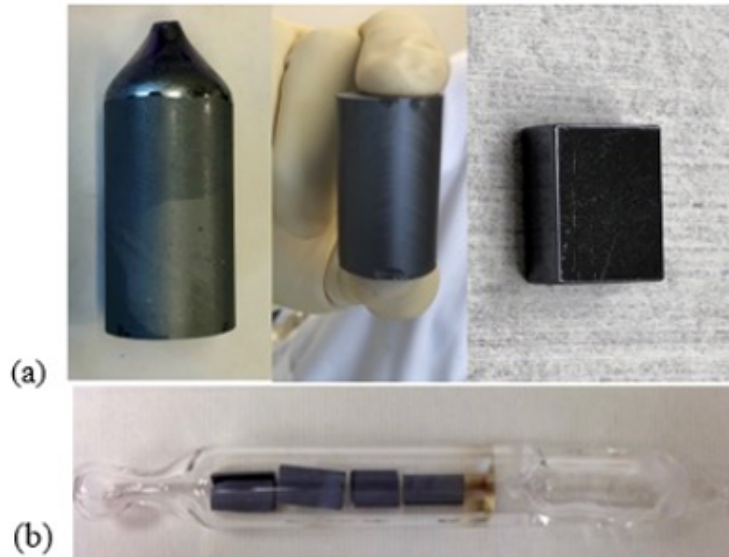


Figure 5.2: (a) Bridgman Grown CdMgTe crystalline boule and a sample prepared for detector fabrication; (b) a vacuum sealed ampoule for annealing

For practical applications, the production of large-sized crystals (≥ 2 inches in diameter) with high yield and low production cost is crucial for advancing beyond current X-ray detector technologies. Additionally, annealing was employed to enhance the crystalline quality of the samples. Fig.5.2 (a) illustrates a Bridgman-grown CMT crystal, showing both the entire boule and

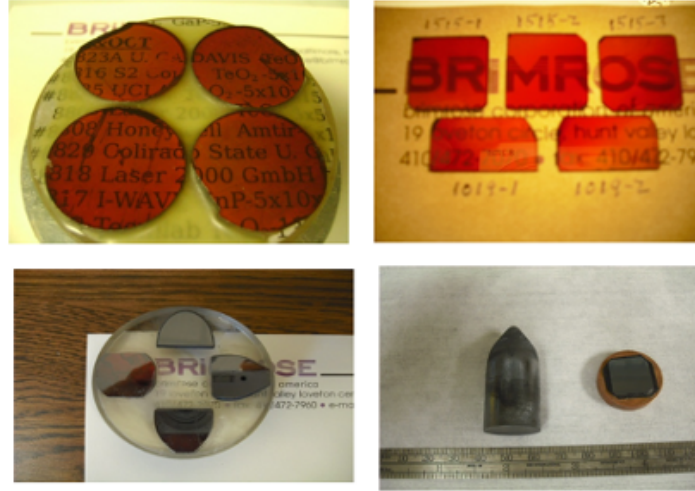


Figure 5.3: $\text{Cd}_{1-x}\text{Mg}_x\text{Te}$ single crystal wafers with different bandgaps: upper right $x = 0.45$, upper left $x = 0.45$, lower left $x = 0.15$, and lower right $x = 0.03$.

the portion remaining after the top and bottom of the boule are removed, along with a sample prepared for detector fabrication. Fig.5.2 (b) displays a vacuum-sealed ampoule containing CdMgTe samples undergoing annealing under Cd pressure.

Along with material processing optimization techniques, such as post-growth annealing, the Mg content and dopant levels can be tailored to engineer the material for various properties. Fig.5.3 shows $\text{Cd}_{1-x}\text{Mg}_x\text{Te}$ with different bandgaps ($x = 0.02$ to 0.45). For X-ray/optical cross-correlation detection, we found that a 3-8% magnesium concentration and 2-5% indium doping were the most suitable parameters.

5.2 Charge transport measurements

One significant factor that needs to be satisfied for ultrafast photoresponse for X-ray Free-Electron Laser coarse timing applications is that the electron lifetime of the material needs to be short, which is contrary to that required for nuclear spectroscopy and imaging applications, where one would aim to increase the electron lifetime value.

To estimate the lifetime in a transmission mode and select qualified samples from the pool of crystals grown under different experimental conditions, Brimrose Co. used an Am-241 source and measured the transient response time τ_e of a $10 \times 10 \times 1 \text{ mm}^3$ CMT sample in a planar detector form and estimate mobility μ via the transit technique. Since the spectral response of these planar detectors are recorded over a wide range of applied bias voltages, an estimation of $\mu\tau_e$ is possible via fitting the Hecht equation (Fig.5.4),

$$Q(V) = \frac{N_0 q V (\mu\tau)_e}{d^2} \left[1 - \exp\left(-\frac{d^2}{(\mu\tau)_e V}\right) \right] \quad (5.1)$$

N_0 represents the number of charge carriers, Q is total charge, d is thickness of the detector, q refers to electronic charge, and V represents applied bias voltage. we could get $\mu\tau_e = 4.349 \times 10^{-5} \text{ cm}^2/\text{V}$ from the fitting result. For CMT samples, the typical mobility (μ) values range from 500 to 1000 cm^2/Vs . Consequently, the estimated τ_e is in the range of 4.5 ns to 9 ns. We only select samples with τ_e in the range of a few ns to 0.1 ms for our ultrafast detectors. It is important to note that this refers to the elec-

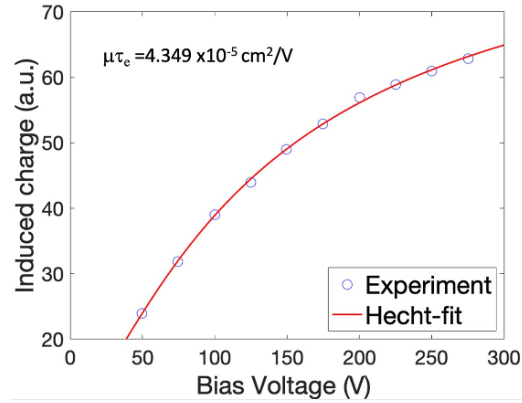


Figure 5.4: Hecht-fit via Am-241 response for obtaining $\mu\tau_e$ value.

tron lifetime in the bulk crystal for radiation detection. The surface electron lifetime will be determined through photoresponse measurements conducted using the well-known pump-probe technique, as discussed in the next section.

5.3 Bandgap and picosecond response measurements

In this section, the bandgap and carrier lifetime of CdMgTe (CMT) samples with a 3% Mg concentration are presented. Specifically, it is necessary to confirm the bandgap energy that aligns with the operational requirements of an optical photodetector, as most ultrafast sources—such as femtosecond lasers and x-ray sources—operate at wavelengths of 800 nm or longer. Furthermore, the carrier lifetime must also be evaluated to ensure the material’s suitability for ultrafast detection applications.

Optical transmission and reflection spectra of the $\text{Cd}_{0.97}\text{Mg}_{0.03}\text{Te}$ sample

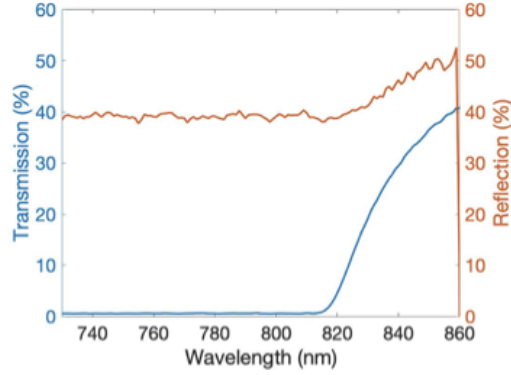


Figure 5.5: transmission and reflection spectra of CMT crystal with 3% Mg are measured at normal incidence using a Perkin-Elmer Lambda 900 spectrometer and shown in Fig.5.5. Scanning wavelength range was 600 nm to 900 nm, with a step size of 1 nm. For light incident on a thick sample, assuming that the reflection from the rear surface is negligible. In this case, the optical transmittance T is related to the optical absorption coefficient α through a simplified relationship, as described in [98]:

$$T = (1 - R)^2 e^{-\alpha d} \quad (5.2)$$

where R represents the reflectance, and d is the thickness of the sample. From Eq.5.2, the absorption coefficient (α) can be rewritten as below:

$$\alpha = \frac{1}{d} \ln \left[\frac{(1 - R)^2}{T} \right] \quad (5.3)$$

By applying the measured transmission and reflection data to the Eq.5.3, the absorption coefficient spectrum can be computed, as shown in Fig. 5.6.

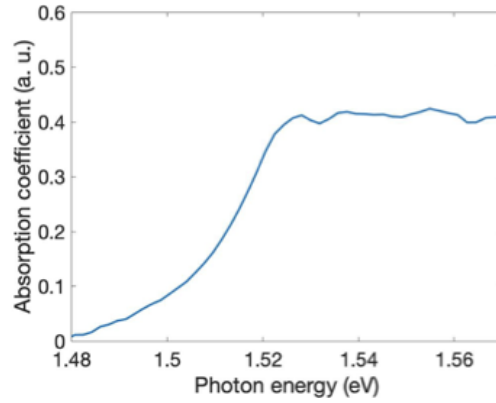


Figure 5.6: Absorption coefficient spectra of CMT crystal

We note a sharp absorption edge in the spectrum at approximately 1.5 eV (826 nm wavelength), which is typical for the band-to-band transition. Tauc equation [131] is used to determine the bandgap (E_g) based on the absorption spectrum of direct bandgap materials,

$$\alpha h\nu = A (h\nu - E_g)^{1/2}, \quad (5.4)$$

Where $h\nu$ is the incoming photon energy, and A is a constant. To calculate E_g , we extrapolate the $[(\alpha - \alpha_1) h\nu]^2$ dependence to the x -axis [132, 133], as shown in Fig. 5.7 where α_1 represents the minimum value of absorption coefficient. This yields $E_g = 1.5$ eV (826.5 nm wavelength) for CMT crystal with 3% Mg. To ensure repeatability, the similar CMT sample with 3% Mg is grown and the test, the similar bandgap result, 1.52 eV, is also presented in Fig. 5.7. Some subgap trap states are observed that may help enhance subgap absorption by introducing intermediate energy levels and facilitate

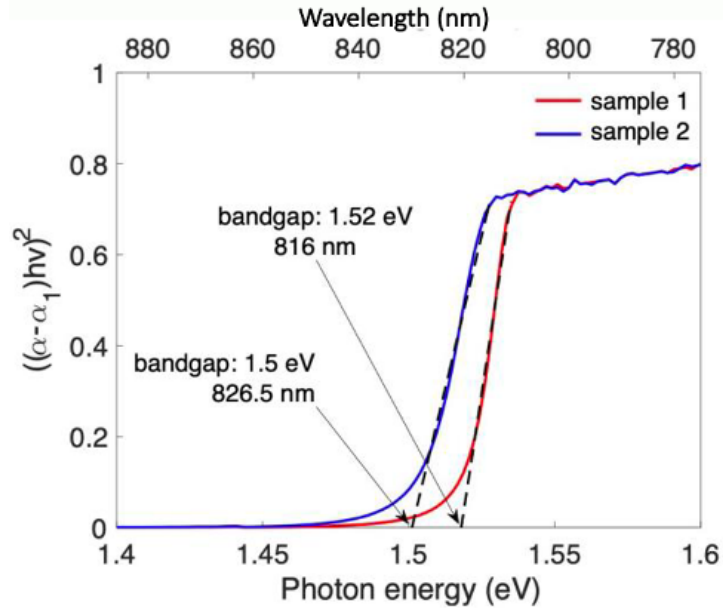


Figure 5.7: Tauc plot of a $\text{Cd}_{0.97}\text{Mg}_{0.03}\text{Te}$ single crystal. Two different samples were tested to analyze the optical properties of the material

charge carrier hopping [134].

Ultrafast photoresponse data were obtained using a pump-probe experimental setup, details can be found in Chapter 3.2.1. The pump excites free electrons from the valence band to excited states in the conduction band, while the probe monitors the photo-excited population of electrons in the entire conduction band.

The equation of complex refractive index is below:

$$\tilde{n} = n + ik, \quad (5.5)$$

where n is the real part and k is the imaginary part of the refractive in-

dex, which is proportional to the absorption coefficient $\alpha = 4\pi k/\lambda$ [135]. For probe beams, changes in the complex refractive index $\Delta\tilde{n}$ induced by the photoexcited electron-hole plasma can be described using the Drude model [136]

$$\Delta n = -\frac{Ne^2}{2\epsilon_0 n_b m^* \omega^2}, \quad (5.6)$$

$$\Delta\alpha = \frac{Ne^2}{\epsilon_0 n_b m^* \omega^2 \tau c}, \quad (5.7)$$

where N is the injected carrier density, e is the elementary charge, m^* is the effective carrier mass, ω is the angular optical frequency, τ is the momentum relaxation time, and $n_b = \sqrt{\epsilon_b/\epsilon_0}$ is the static dielectric constant. The contribution of holes to Δn and $\Delta\alpha$ is neglected due to their significantly heavier mass compared to electrons. For pump-probe spectroscopy in reflection mode, the differential reflectivity $\Delta R/R$ is defined as

$$\frac{\Delta R}{R} = \frac{R - R_0}{R}, \quad (5.8)$$

where R_0 and R are the reflectivities in the absence and presence of the pump beam, respectively. Using Fresnel's equation [137], for normal incidence:

$$R = \left(\frac{\tilde{n} - 1}{\tilde{n} + 1} \right)^2, \quad (5.9)$$

The normalized change in reflectivity $\Delta R/R$ can be expressed as:

$$\frac{\Delta R}{R} = \frac{d(\ln R)}{d\tilde{n}} \Delta\tilde{n} \quad (5.10)$$

Substituting Eq.5.6 into Eq.5.10 gives:

$$\frac{\Delta R}{R} = -\frac{2\epsilon_0 n e^2}{\omega^2} \frac{d(\ln R)}{dn} \frac{N}{m}, \quad (5.11)$$

Equation 5.11 shows that $\Delta R/R$ is linearly proportional to the carrier density N , making time-resolved measurements of $\Delta R/R$ directly indicative of the time evolution of N in the conduction band and does not depend on the details of the electronic states. The time-resolved $\Delta R/R$ signal collected from CdMgTe samples can be fitted using a single exponential relaxation model

$$\Delta R/R \propto \exp(-t/\tau), \quad (5.12)$$

where the initial fast relaxation time τ can be attributed to either electron-optical-phonon cooling or the direct trapping of hot, highly-excited electrons [138, 139]. This general model was originally derived by a former PhD student, Dr. John Serafini in our group [140].

Within the framework of the Drude model, $\Delta R/R$ is proportional to the nonequilibrium electron concentration in CMT. Consequently, the parameter τ can be interpreted as the carrier relaxation time. Based on Eq. 5.12, the relaxation time τ for Cd_{0.97}Mg_{0.03}Te is determined to be 3 ps. Further-

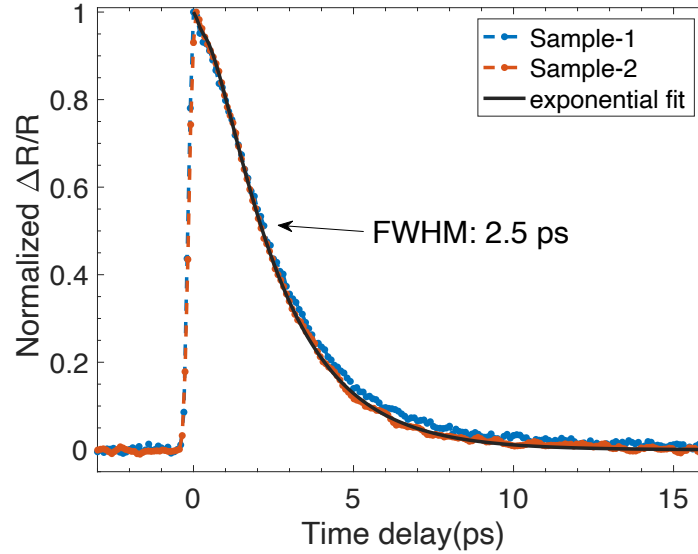


Figure 5.8: $\text{Cd}_{1-x}\text{Mg}_x\text{Te}$ ($x = 0.03$), single crystal pump-probe measurement results, indicate an ultrafast (2.5 ps) photoresponse with a 3 ps single-exponential relaxation. The exponential fit (solid black line).

more, the full width at half maximum (FWHM) of the photoresponse pulse is measured to be 2.5 ps, confirming the ultrafast response of the material.

5.4 Device fabrication

The fabrication process of the CMT device prototype was carried out at Brimrose Co. The CMT crystals were cut into appropriately sized samples, ranging from 4 mm^2 to 10 mm^2 in area and 1–2 mm in thickness, and fabricated into a metal-semiconductor-metal (MSM) structure for both electrical and optical characterization. A proof-of-concept CMT surface detector is shown in Fig. 5.9, with an initial R&D pattern displayed in the inset: a mi-

croscope image of the metal contacts at 100X magnification. Each finger of the pattern is $500\ \mu\text{m}$ in length and $70\ \mu\text{m}$ in width, with a gap of $30\ \mu\text{m}$ between adjacent fingers.

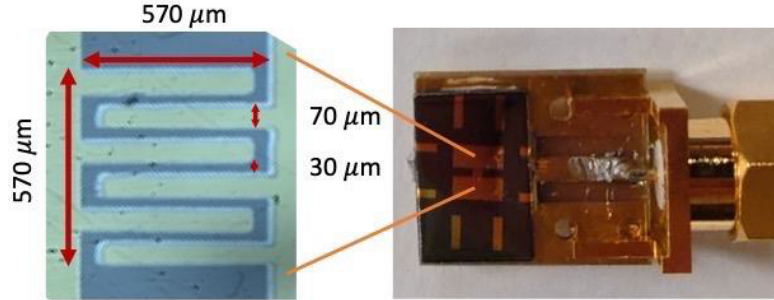


Figure 5.9: A proof-of-concept CMT surface photodetector. Inset on the left shows with a meander electrode pattern in detail. The device was wire-bonded to an SMA (Sub-Miniature Version A) connector for high-speed measurements.

The described structure represents the optical surface detector on the front side, featuring two narrowly separated voltage terminals (+Low V and ground). One terminal is wire-bonded to a $50\ \Omega$ Sub-Miniature version A (SMA) connector for biasing and high-speed measurements, while the other is connected to ground for safety. The metal deposition was performed on the CdMgTe surface using an electron-beam evaporator. A two-layer metal structure was employed: the first layer consisted of $211\ \text{\AA}$ of chromium (Cr) for adhesion, and the second layer comprised $687\ \text{\AA}$ of gold (Au) to ensure conductivity.

For more sophisticated devices, a laser writer with higher resolution is required. We utilized the Microtech LW405C laser writer in the UR nano

cleanroom, which offers a resolution of $1\ \mu\text{m}$, sufficient for our device fabrication. A $4\ \text{mm} \times 4\ \text{mm} \times 1\ \text{mm}$ CMT crystal was fabricated by Brimrose and subsequently shipped to UR. The designed pattern is shown in Fig. 5.10(a). The active area for photodetection is $600\ \mu\text{m} \times 600\ \mu\text{m}$, with finger widths of $30\ \mu\text{m}$ and lengths of $570\ \mu\text{m}$. The gap between fingers is $30\ \mu\text{m}$. The large pads are designed in a trapezoidal shape, with one side measuring $1\ \text{mm}$ and the other $2\ \text{mm}$, to mitigate power reflections between the active area and the microstrip line.

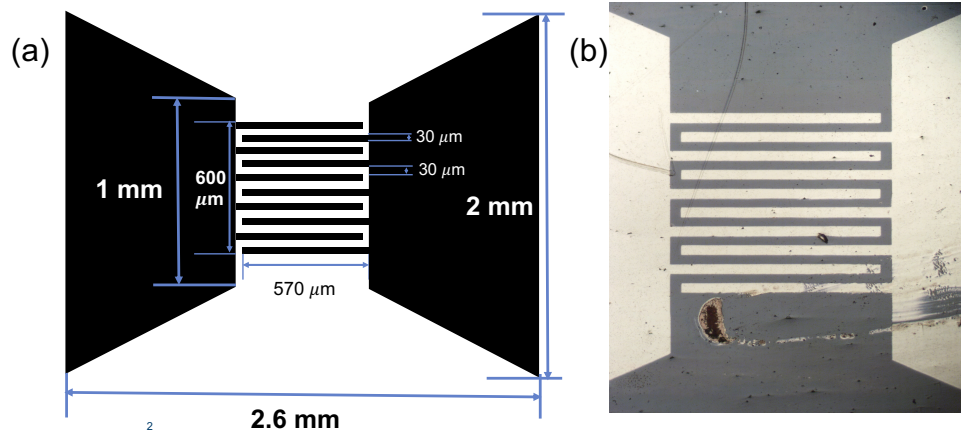


Figure 5.10: (a) Schematic design of the fabricated pattern, illustrating the geometric dimensions of the structure, including the active area ($600\ \mu\text{m} \times 600\ \mu\text{m}$), finger width ($30\ \mu\text{m}$), finger spacing ($30\ \mu\text{m}$), and total finger length ($570\ \mu\text{m}$). The large trapezoidal pads have widths of $1\ \text{mm}$ and $2\ \text{mm}$, designed to mitigate power reflections. (b) Optical microscope image of the fabricated pattern, demonstrating the successful transfer of the design onto the CMT crystal.

However, we encountered several challenges when using a conventional

lift-off approach. The first issue was during spin coating: due to a small sample size, an edge effect was observed, where the central region of the photoresist film was significantly thicker than the edges. To achieve a more uniform film, the rotation speed was doubled. However, the most significant challenge was the lift-off process itself. Because the pattern was relatively large, the deposited gold film covered the entire edge of the photoresist, preventing the solvent from effectively removing the photoresist.

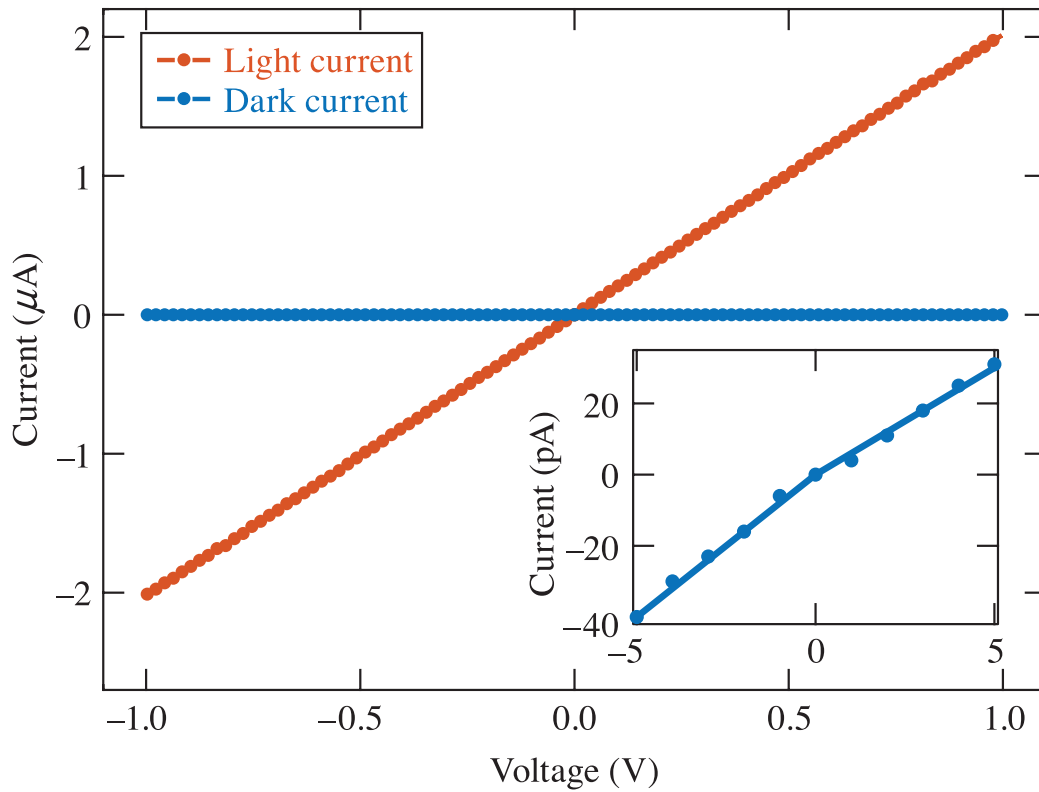
The suitable method, based on Au etching, for the CMT crystal fabrication is found. The sample surface is polished during the sample preparation step, then it was placed into a Reactive Ion Etcher where reactive gases and RF power are used to create a chemically reactive plasma to clean the sample surface. First, a 2-nm thick Cr was deposited on the CMT surface for adhesion and followed by an 150 nm Au film using e-beam evaporation. Secondly, a negative photoresist was spin coated on the substrate and then exposed to the designed pattern (Fig. 5.10(a)). Third, the sample was immersed in acetone and developed for 2 minutes to remove the unwanted photoresist pattern. This development step was critical for precisely eliminating the non-exposed regions of the photoresist. The last step, the sample was reintroduced into the Reactive Ion Etcher for CHF_3 etching. This etching process was conducted for 20 minutes to remove any extra gold. Immediately following the CHF_3 etching, the reactive gas was switched to O_2 , and an ashing process was performed to completely remove all remaining photoresist. The final fabricated pattern was then imaged and measured using a high-

resolution microscope, as shown in Fig. 5.10(b). The microscopic analysis clearly demonstrates that the quality of the fabrication is in good accordance with the initial design specifications, thereby validating the effectiveness and precision of the employed fabrication process.

5.5 Electrical photoconductive effect and responsivity

Fig.5.11 illustrates the strong photoconductive effect observed on CMT MSM diode. Under optical excitation (orange curve, 20 mW laser power), the photocurrent reaches approximately $2 \mu\text{A}$ at a 1 V bias. The I - V dependence is linear, indicating the absence of Schottky barriers. At the same time, the dark current (blue curve) is completely negligible. To avoid potential breakdown between the electrodes, which are separated by just $25 \mu\text{m}$, the bias voltage was limited to 1 V during these measurements. An accurate measurement of the dark current, performed on a CMT sample, is shown in the inset of Fig. 5.11. The dark current is observed to be in the picoampere range, as low as 40 pA at a bias of -5 V . For a nominal 1 V bias, the ratio of light current to dark current exceeds 2×10^5 . Moreover, the dark current of the leak remains well below 100 pA, meeting the upper limit typically required for x-ray detection.

Further systematic photoresponse characterization was conducted on the CMT MSM diodes, experimental setup details could be found in Chap-



E30445J1

Figure 5.11: I–V characteristics under light (red) and dark (blue) conditions for a tested CMT MSM device. The inset shows the dark current I–V in detail (bulk measurement across a CMT sample).

ter.3.2.2. To ensure uniformity and enhance the response, the beam size was enlarged to cover the pattern. Fig.5.12 shows a family of the IV current traces as a function of detector bias voltage for the incident power in the 20- μW to 600-mW range.

Fig. 5.12 presents a family of current-voltage (I–V) characteristics measured under a wide range of optical excitations (800-nm wavelength). I – V dependence is linear, indicating the absence of Schottky barriers. The device

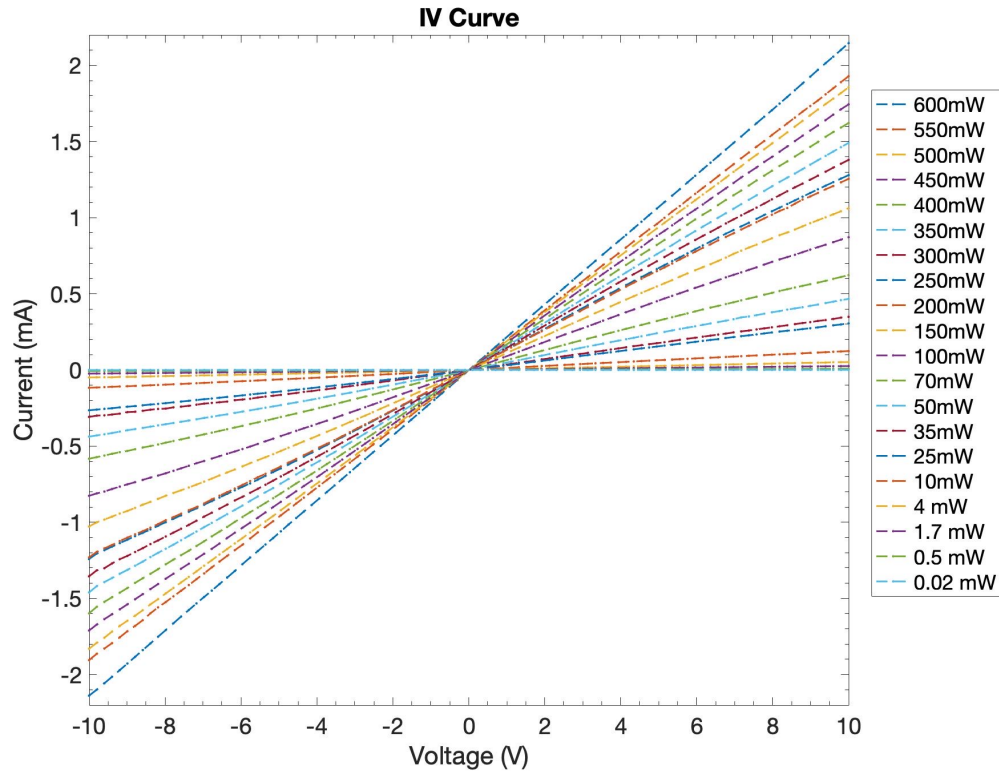


Figure 5.12: The I–V characteristics of our proof-of-concept $\text{Cd}_{1-x}\text{Mg}_x\text{Te}$ ($x = 0.03$) photodetector were measured under various power levels of 800-nm optical excitation. The beam diameter was approximately $300 \mu\text{m}$.

demonstrated excellent stability and could, in principle, operate at higher bias voltages. Meanwhile, Fig. 12 shows the corresponding optical responsivity as a function of the detector bias under the same optical excitation conditions. The relatively low bias voltages used in these studies were chosen to avoid the risk of reaching the breakdown voltage in our structure. The dark current, measured at 0.75 V bias without any laser illumination and with all ambient lights turned off, was 0.4 nA. The responsivity, de-

defined as the photocurrent divided by the incident optical power, is shown in Fig. 5.13. These dependences are linear, with responsivity values increasing as the incident optical power decreases. This behavior is common in semiconductors where there is a substantial disparity in electron and hole mobilities. When the electron mobility significantly exceeds that of holes, the electron transit time between the electrodes is much shorter than the hole lifetime. This disparity leads to an intrinsic gain mechanism, as many electrons are collected at the positive electrode before a single hole reaches the negative electrode.

In general, this effect is more pronounced under low optical illumination and in materials with relatively low carrier concentrations, such as our high-resistivity $\text{Cd}_{1-x}\text{Mg}_x\text{Te}$ sample. The highest responsivity observed was approximately 20 mA/W at a 10-V bias. However, we anticipate a substantial increase in responsivity with the optimization of surface electrodes.

5.6 Time-resolved photoresponse

We have also conducted preliminary electrical time-resolved photoresponse experiments. Further details can be found in Section 3.2.2. The 800 nm trace (blue) represents the photoresponse to 100 fs-wide, 800 nm wavelength optical pulses and recorded using a 5 GHz oscilloscope. The X-ray trace (black) corresponds to the photoresponse to 100 fs-wide, 9.8 keV central energy X-ray pulses measured at the SLAC National Accelerator Laboratory at Stanford

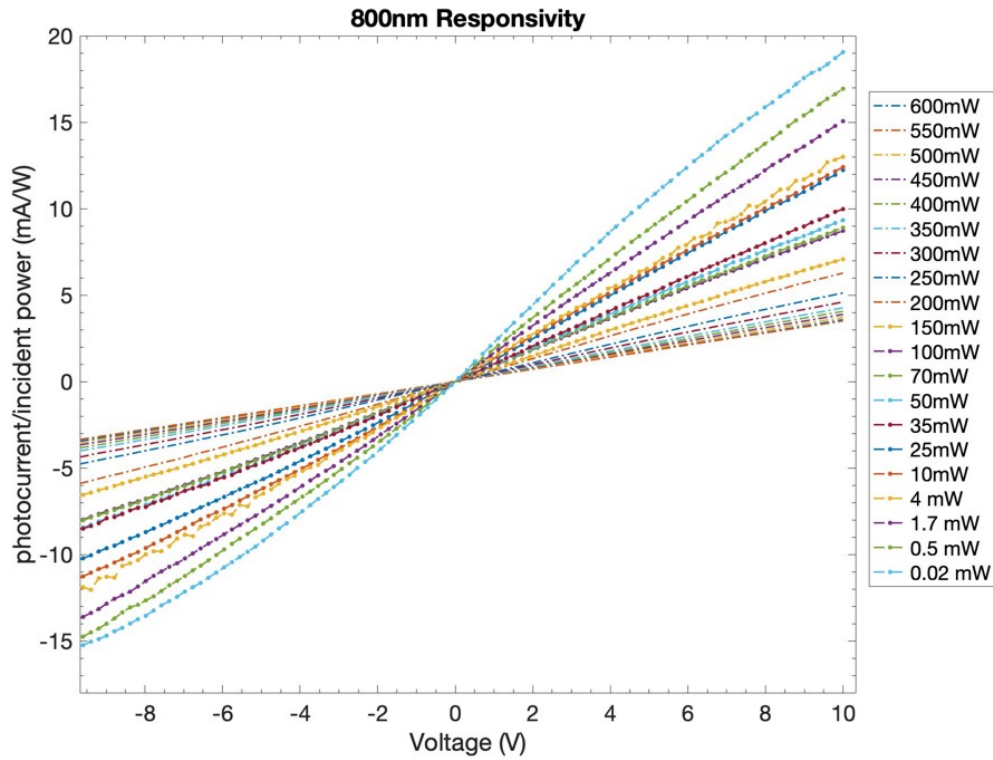


Figure 5.13: Responsivity as a function of bias voltage. The calculations are shown for various values of incident optical power

University, also recorded using a 5 GHz oscilloscope. The High Harmonic trace (red) shows the photoresponse to 100 fs-wide, 55–60 eV pulses measured at the High Harmonic Generation Facility in Jülich Research Centre, Germany, using a 5 GHz oscilloscope. All signals exhibit a rise time of less than 100 ps, limited by the bandwidth of the respective oscilloscopes.

To facilitate comparison, the recorded voltage signals were normalized. The FWHM measurements obtained from all three methods are highly consistent: 220 ps for 800 nm, 220 ps for X-ray, and 260 ps for High Harmonic.

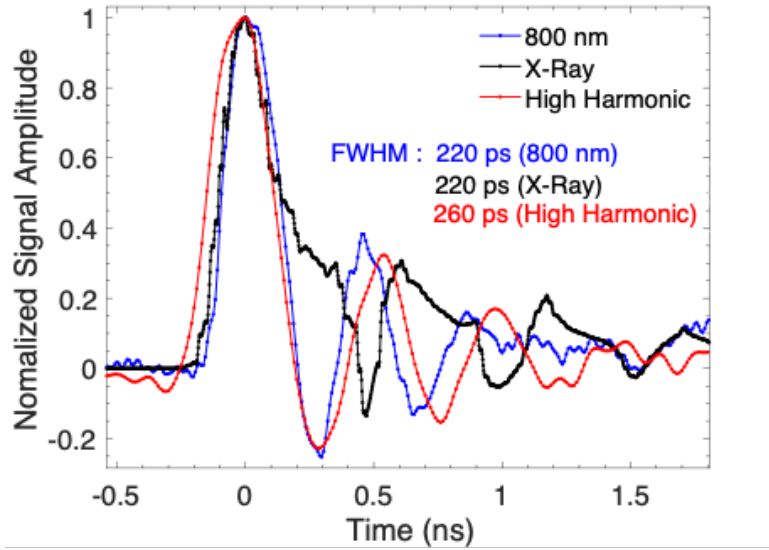


Figure 5.14: Time resolved CMT detector response to a pulsed x-ray, 800 nm, high harmonics signals

The differences in FWHM values are primarily attributed to the bandwidth limitations of the oscilloscopes, particularly for the high harmonic measurements, where the 5 GHz bandwidth is insufficient to accurately capture the picosecond response confirmed in the carrier lifetime section, where electro-optic sampling techniques is needed. The observed post-pulse oscillations are attributed to the impedance mismatch between the test sample and the 50 Ω SMA connector. These results confirm that CMT devices are highly suitable for picosecond free-electron laser and optical pump-probe spectroscopy timing applications.

5.7 Three terminal Device

In this section, we focused on transitioning from a 2-terminal device (operating in reflection mode only) to a 3-terminal device designed for transmission mode (Fig.5.15). We determined that two SMA connectors are required for 3-terminal device, along with a board design that allows the back contact to be biased with a high voltage for the volume detector.

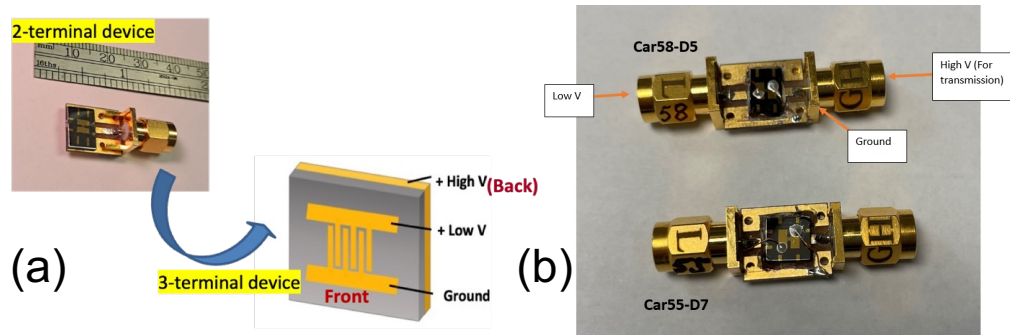


Figure 5.15: (a) Schematics of interdigitated surface electrodes and a back-crystal contact to collect X-ray-generated electrons. (b) A proof-of-concept three-terminal device to be developed for simultaneous surface absorption, optical, and volume transmission X-ray experiments.

The first SMA is allocated for low positive voltage (+V) and readout at the main pin, with the other terminal wired to ground, replicating the reflection mode used previously. The second SMA is designated for high positive voltage bias (+V) and transmission mode signal readout at the main pin, sharing a common ground. Note that the back side of the diode contains a third electrode, labeled “+High V.” A three-terminal device configuration was designed to include a volume detection x-ray pulses. Thus, at the front

face there is an optical surface detector with two narrow-spaced voltage terminals (+Low V and ground), while the x-ray volume detector is formed between the ground and the high-voltage, back-face electrode. In the latter case, the electric field is applied across the thickness of the CMT crystal

The HHG photoresponse experimental results for this same CdMgTe device are shown in Fig.5.16. In the case of a volume detector the photoresponse signal a very weak signal indicating a lack of HHG incident power was too low to create a substantial photoelectric effect in the detector volume. The photoresponse showed a FWHM of 2.9 ns, a rise time of 3 ns, and a fall time of 2 ns. Again, reflections in the volume detector response are due to the detector-housing mismatch.

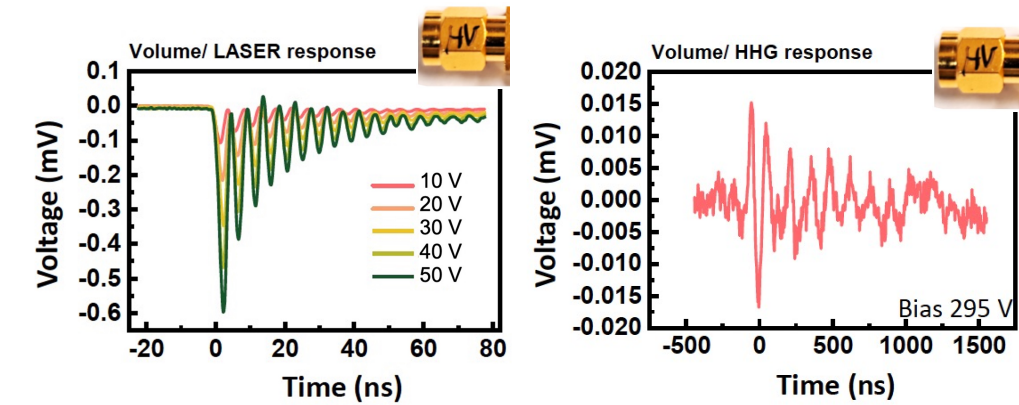


Figure 5.16: Optical photoresponse experimental results for volume detector at the HHG facility

5.8 Improved time-resolved photoresponse

A new package design is presented in the inset of Fig 5.17. The fabricated MSM is mounted within the head, which can be directly inserted into the SMA connector. Signal measurements were performed using the same experimental setup as presented in Chapter. 3.2.2, with the addition of a 25-GHz bandwidth oscilloscope to ensure high-frequency accuracy and precision. The blue curve represents the measured data, the red curve shows the data smoothed using a designed filter, and the black dashed line represents the Gaussian fit. These three data sets overlap quite well in Fig. 5.17. The FWHM of these pulses were measured to be 100 ps, significantly faster than the signals shown in Fig. 5.14, owing to the use of a more advanced oscilloscope and packaging. Moreover, post-pulse reflections were found to be nearly negligible, which can be attributed to the 18 GHz bandwidth SMA connector employed. Additionally, the rise time of the pulse was measured to be 43 ps, primarily limited by the bandwidth of the oscilloscope. The intrinsic response time of our detector can be calculated using the following equation,

$$t_{\text{int}} = \sqrt{t_{\text{FWHM}}^2 - t_{\text{scope}}^2 - t_{\text{SMA}}^2}, \quad (5.13)$$

We calculated that the intrinsic response time (t_{int}) of the improved detector is 73 ps. This value is still much larger than the carrier trapping time, as shown in Fig. 5.8.

The limitations in the detector's ultrafast response arise from several fac-

tors. First, the bandwidth of the oscilloscope is insufficient, which limits both the observed rise time and the overall speed of the system. Additionally, the bandwidth of the connectors and cables further restricts the performance of the detector. Another crucial factor is the RC time constant, which governs the charging and discharging rates in the circuit. This time constant, influenced by the material properties of the detector, defines how quickly the detector responds to incoming signals, thereby establishing an upper limit on its performance. Together, these factors constrain the ability to achieve faster response times in our ultrafast detection systems.

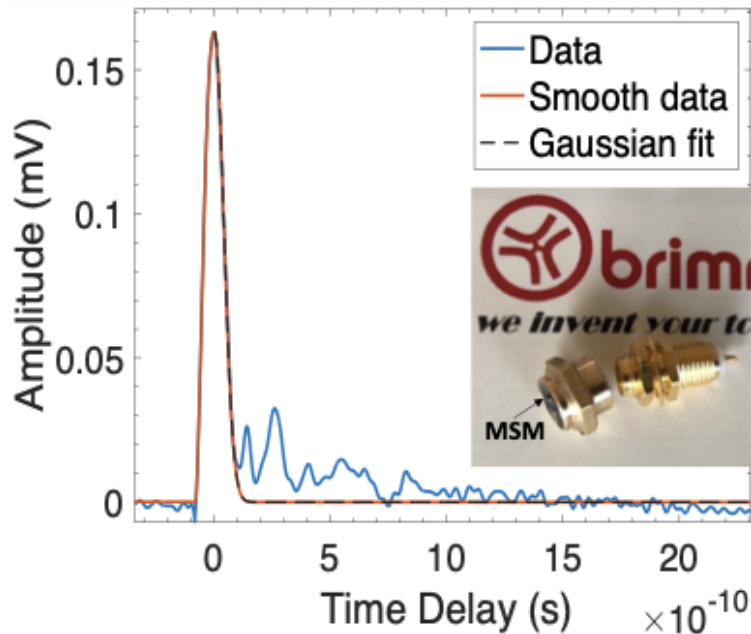


Figure 5.17: Time-resolved CMT detector response to pulsed 800 nm signals, measured using a 25-GHz bandwidth oscilloscope. Blue: Measured photoreponse; Red: Response smoothed by a high-pass filter; Black: Gaussian fit. Inset: New package, allowing direct insertion of the MSM into the SMA connector.

Chapter 6

Future Work

6.1 Future work about THz spintronics

6.1.1 Temperature-dependent THz transients in moderately remnant CoPd and strongly remnant FeCo nanolayers

Temperature dependences of THz transients emitted from CoPd/Pd and CoFe/Ir are presented in Fig.6.1. In both cases, the THz peak amplitude decreases as the temperature decreases, which is in contrast to the Py/Pt case. At 70 K, $A_{\text{THz}}(T)$ of CoPd/Pd drops by 70% and that of CoFe/Ir by 20%, compared to the room-temperature (RT) data.

We believe that for hard magnetic materials, the impact of magnetization becomes less significant. The Curie temperature of both samples is well above 400 K [141, 142]. When the temperature moves far below the Curie temperature, the magnetization changes only slightly, and other temperature-

sensitive properties, such as the spin Hall conductivity, are likely to dominate over $M(T)$ as the key factor [143]. Further studies are ongoing to confirm this conclusion.

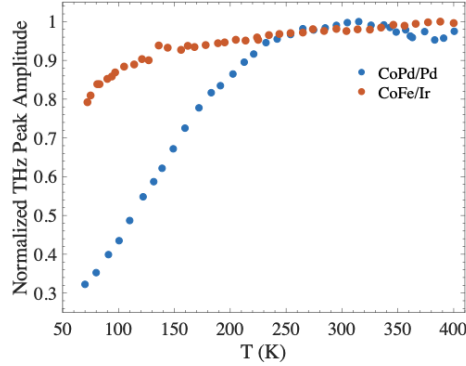


Figure 6.1: THz peak amplitude values of CoPd/Pd (blue dots) and CoFe/Ir (orange dots) samples as a function of temperature.

6.1.2 THz Measurements in the reflection mode

We can also explore the measurement of FeCo/Graphene in reflection mode. The experimental setup for the THz-TDS system in reflection mode closely resembles that described in Section 3.1.1. However, in this configuration, the sample is positioned at a 45° angle relative to the incident light. This approach allows us to probe exclusively the state of the graphene layer(s) on top of the FeCo/Graphene system, providing deeper insights into the asymmetric distribution of photocarriers in graphene's \mathbf{k} -space, which contributes to the Rashba texture.

6.2 Future work about CMT detector

6.2.1 Electro-optic sampling

Electro-optic sampling (EOS) is a measurement technique based on the electro-optic (EO) effect, also known as a Pockels effect. The EO effect means that the refractive index of a non-centrosymmetric material is proportional to the strength of an applied electric field [144]. There are several advantages of EOS system. Firstly, it provides ultrafast temporal resolution down to femtosecond timescale, far better than traditional oscilloscopes. Second, EOS can measure both the amplitude and phase of the signal, providing a more complete characterization of waveforms. In the future work, EOS system can be used to investigate the ultrafast response of CMT single detectors. To demonstrate this idea, a similar ‘experiment-on-chip’ measurement can be designed as the one earlier constructed in our group [145, 146] and shown in Fig.6.2 (a). CMT crystals will be cut into platelets with the (110) surface orientation to get the maximal EO effect in CMT and an Au coplanar waveguide transmission line will be deposited on the surface of CMT platelet. Subsequently, a time-resolved measurement can be conducted utilizing the EOS setup, which is illustrated in Fig.6.2 (b). The laser beam will be split into two parts: the pump beam is utilized to excite a CMT photodetector, while the sampling beam is used to probe the EO change. To facilitate the experiment, the pump beam will be frequency doubled using a BBO crystal

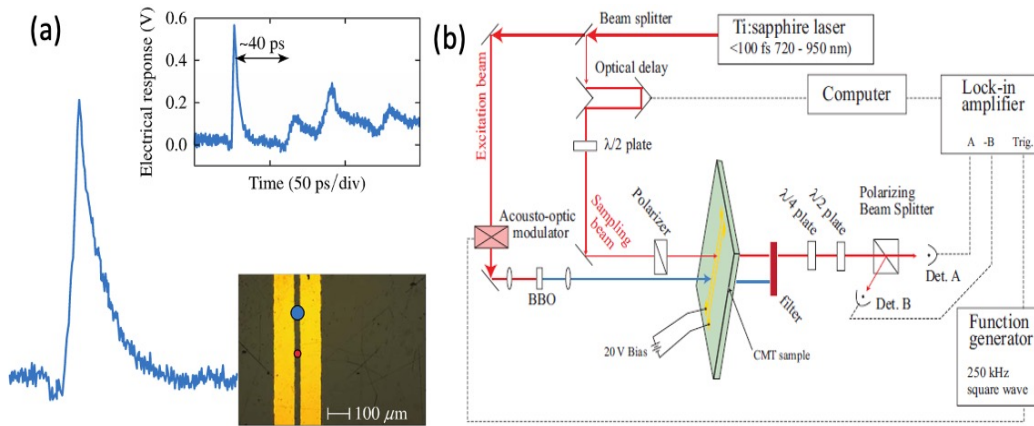


Figure 6.2: (a) A time resolved CMT photoconductive response measured at $75 \mu\text{m}$ from the excitation spot via the internal EO effect. (b) the schematic of two-color EOS setup. [146]

and modulated via an acoustic optical modulator before being focused onto the detector, while EO probing will be done in transmission mode using 820-nm light, taking advantage of an intrinsic EO effect in CMT. An example of a sampled transient signal from [146] is shown in Fig.6.2 (a). I hope to achieve similar results.

Bibliography

- [1] Md Didarul Alam, Syeda S Nasim, and Samiul Hasan. Recent progress in cdznte based room temperature detectors for nuclear radiation monitoring. *Progress in Nuclear Energy*, 140:103918, 2021.
- [2] A. Hossain, V. Yakimovich, A.E. Bolotnikov, K. Bolton, G.S. Camarda, Y. Cui, J. Franc, R. Gul, K.H. Kim, H. Pittman, and G. Yang. Development of cadmium magnesium telluride ($\text{cd}_{1-x}\text{mg}_x\text{te}$) for room temperature x-and gamma-ray detectors. *Journal of Crystal Growth*, 379:34–40, 2013.
- [3] S.B. Trivedi, C.C. Wang, S. Kutcher, U. Hommerich, and W. Palosz. Crystal growth technology of binary and ternary ii–vi semiconductors for photonic applications. *Journal of Crystal Growth*, 310(6):1099–1106, 2008.
- [4] E.G. LeBlanc, M. Edirisooriya, O.S. Ogedengbe, O.C. Noriega, P.A.R.D. Jayathilaka, S. Rab, C.H. Swartz, D.R. Diercks, G.L. Burton, B.P. Gorman, and A. Wang. Determining and controlling the magnesium composition in cdte/cdmgte heterostructures. *Journal of Electronic Materials*, 46:5379–5385, 2017.
- [5] J.M. Hartmann, J. Cibert, F. Kany, H. Mariette, M. Charleux, P. Alleysson, R. Langer, and G. Feuillet. Cdte/mgte heterostructures: Growth by atomic layer epitaxy and determination of mgte parameters. *Journal of Applied Physics*, 80:6257–6265, 1996.
- [6] A. Waag, H. Heinke, S. Scholl, C.R. Becker, and G. Landwehr. Growth of mgte and $\text{cd}_{1-x}\text{mg}_x\text{te}$ thin films by molecular beam epitaxy. *Journal of Crystal Growth*, 131:607–611, 1993.

-
- [7] A. Hoffmann. Spin hall effects in metals. *IEEE Transactions on Magnetics*, 49(10):5172–5193, 2013.
- [8] Y. Shiomi, K. Nomura, Y. Kajiwara, K. Eto, V. Novák, and E. Saitoh. Spin-electricity conversion induced by spin injection into topological insulators. *Physical Review Letters*, 113(19):196601, 2014.
- [9] T. Jungwirth, X. Marti, P. Wadley, and J. Wunderlich. Antiferromagnetic spintronics. *Nature Nanotechnology*, 11(3):231–241, 2016.
- [10] S. Roche, J. Åkerman, B. Beschoten, J. C. Charlier, M. Chshiev, S. P. Dash, and S. O. Valenzuela. Graphene spintronics: the european flagship perspective. *2D Materials*, 2(3):030202, 2015.
- [11] W. Han, R. K. Kawakami, M. Gmitra, and J. Fabian. Graphene spintronics. *Nature Nanotechnology*, 9(10):794–807, 2020.
- [12] A.W. Cummings, S.M.M. Dubois, J.C. Charlier, and S. Roche. Universal spin diffusion length in polycrystalline graphene. *Nano Letters*, 19(10):7418–7426, 2019.
- [13] S. Konschuh, M. Gmitra, and J. Fabian. Tight-binding theory of the spin-orbit coupling in graphene. *Physical Review B*, 82(24):245412, 2010.
- [14] K.T. Kim, C. Zhang, A.D. Shiner, S.E. Kirkwood, E. Frumker, G. Gariepy, A. Naumov, D.M. Villeneuve, and P.B. Corkum. Manipulation of quantum paths for space-time characterization of attosecond pulses. *Nature Physics*, 9(3):159–163, 2013.
- [15] A. Avsar, J.H. Lee, G.K.W. Koon, and B. Özyilmaz. Enhanced spin-orbit coupling in dilute fluorinated graphene. *2D Materials*, 2(4):044009, 2015.
- [16] L. Brey. Spin-orbit coupling in graphene induced by adatoms with outer-shell p orbitals. *Physical Review B*, 92(23):235444, 2015.
- [17] C. Weeks, J. Hu, J. Alicea, M. Franz, and R. Wu. Engineering a robust quantum spin hall state in graphene via adatom deposition. *Physical Review X*, 1(2):021001, 2011.

- [18] M. Peralta, E. Medina, and F. Mireles. Proximity-induced exchange and spin-orbit effects in graphene on ni and co. *Physical Review B*, 99(19):195452, 2019.
- [19] J. Balakrishnan, G.K.W. Koon, A. Avsar, Y. Ho, J.H. Lee, M. Jaiswal, S.J. Baeck, J.H. Ahn, A. Ferreira, M.A. Cazalilla, and A.H.C. Neto. Giant spin hall effect in graphene grown by chemical vapour deposition. *Nature Communications*, 5(1):4748, 2014.
- [20] J.C. Rojas-Sánchez, N. Reyren, P. Laczkowski, W. Savero, J.P. Attané, C. Deranlot, M. Jamet, J.M. George, L. Vila, and H. Jaffrès. Spin pumping and inverse spin hall effect in platinum: the essential role of spin-memory loss at metallic interfaces. *Physical Review Letters*, 112(10):106602, 2014.
- [21] P. F. Moulton. Spectroscopic and laser characteristics of ti:al₂o₃. *J. Opt. Soc. Am. B*, 3:125–133, Jan 1986.
- [22] D. H. Sutter et al. Semiconductor saturable-absorber mirror-assisted kerr lens modelocked ti:sapphire laser producing pulses in the two-cycle regime. *Opt. Lett.*, 24(9):631, 1999.
- [23] Xiaohong Han and Heping Zeng. Kerr-lens mode-locked ti:sapphire laser with an additional intracavity nonlinear medium. *Optics Express*, 16(23):18875–18880, 2008.
- [24] J. A. Armstrong. Measurement of picosecond laser pulse widths. *Applied Physics Letters*, 10(1):16, 1967.
- [25] John R. Serafini. *Ultrafast Optical and Electronic Characterization of (Cd,Mg)Te Single Crystals*. PhD thesis, University of Rochester, 2017. Accessed: 2023-02-11.
- [26] Benjamin Ferguson, Qian Wang, Xi-Cheng Zhang, and Nigel Chamberlain. Terahertz spectroscopy applied to the analysis of artists’ materials. *Applied Physics A*, 100(3):591–597, 2010.
- [27] John David Jackson. *Classical Electrodynamics*. Wiley, 1998.
- [28] B. Sklar. *Digital Communications: Fundamentals and Applications*. Prentice Hall, 2001.

-
- [29] G. D. Boreman. *Introduction to Applied Optics*. CRC Press, 2005.
- [30] E. Hecht. *Optics*. Pearson, 5th edition, 2017.
- [31] C. E. Mack. *Fundamentals of Semiconductor Manufacturing and Process Control*. John Wiley & Sons, 2008.
- [32] W. R. Hendee and E. R. Ritenour. *Medical Imaging Physics*. John Wiley & Sons, 2002.
- [33] R. Amato and M. Robbins. Positron emission tomography (pet) and its applications in medical diagnosis. *Journal of Medical Imaging*, 20(2):20–35, 2013.
- [34] D. J. Brenner and E. J. Hall. Computed tomography—an increasing source of radiation exposure. *New England Journal of Medicine*, 357(22):2277–2284, 2007.
- [35] Z. Jiang and Q. Wu. Recent advances in terahertz generation, detection, and applications. *Optics Express*, 29(5):6482–6495, 2021.
- [36] D. M. Mittleman. Terahertz technology. *Applied Physics*, 28:1–18, 2003.
- [37] Masayoshi Tonouchi. Cutting-edge terahertz technology. *Nature photonics*, 1(2):97–105, 2007.
- [38] A. Melikyan and I. Kurochkin. Quantum cascade lasers: Principles, developments, and applications in terahertz systems. *Journal of Optics*, 24(2):021301, 2022.
- [39] J. Xu and X. C. Zhang. Terahertz non-destructive testing and imaging. *Materials Science and Engineering*, 36(2):152–162, 2012.
- [40] S. Szobor and S. Stamatopoulou. Terahertz radiation in security applications. *Journal of Security and Privacy*, 8(3):47–58, 2020.
- [41] D. Klein and X. He. Terahertz spectroscopy for hazardous substance detection. *Sensors*, 18(7):2153, 2018.
- [42] B. Ferguson and X. C. Zhang. Terahertz imaging and applications in medicine. *Journal of Microscopy*, 206(3):324–331, 2002.

-
- [43] Y. Zhao and Y. Liu. Terahertz imaging for biomedical applications. *Journal of Biophotonics*, 14(8):e202100091, 2021.
- [44] Debamitra Chakraborty, Bradley N Mills, Jing Cheng, Ivan Komisarov, Scott A Gerber, and Roman Sobolewski. Development of terahertz imaging markers for pancreatic ductal adenocarcinoma using maximum a posteriori probability (map) estimation. *ACS Applied Materials & Interfaces*, 12(10):12023–12031, 2020.
- [45] Q. Zhang and X. Wang. Terahertz communication systems for 6g: Challenges and opportunities. *IEEE Access*, 9:111753–111765, 2021.
- [46] J. L. Carlin and A. Sorrentino. Terahertz frequency bands for satellite communications: A new horizon for 6g. *Nature Communications*, 11, 2020.
- [47] H Nemeč, A Pashkin, P Kuzel, M Khazan, S Schnull, and I Wilke. Carrier dynamics in low-temperature grown gaas studied by terahertz emission spectroscopy. *Journal of Applied Physics*, 90(3):1303–1306, 2001.
- [48] X. Liu, X. Zhang, S. Xu, and X. Li. Terahertz generation and detection in photoconductive antennas. *Journal of Applied Physics*, 109(3):033104, 2011.
- [49] J. Jensen, S. Lee, and H. Kim. High-efficiency terahertz emission and detection using photoconductive antennas. *Optics Express*, 20(15):15635–15640, 2012.
- [50] P. Wang and T. Zhang. Terahertz wave generation and detection: Technologies and applications. *Journal of Infrared, Millimeter, and Terahertz Waves*, 36(5):598–625, 2015.
- [51] Y. Zhang, L. Li, and Q. Huang. Ultrafast carrier dynamics in low-temperature-grown gaas for thz emission. *Journal of Applied Physics*, 128(10):103103, 2020.
- [52] R. Galler, F. Keilmann, and R. Huber. Balanced detection technique for thz radiation. *Applied Physics Letters*, 91(6):061101, 2007.

- [53] K. Bennett, J. Kuntz, and P. Braun. Phase matching in nonlinear thz generation. *Journal of Optical Society of America B*, 31(5):1064–1069, 2014.
- [54] Y. Gao, M. Kroll, and A. Wright. Quasi-phase matching in gaas for thz radiation. *Nature Photonics*, 10(3):165–170, 2016.
- [55] T. Seifert, S. Jaiswal, M. Sajadi, G. Jakob, S. Winnerl, M. Wolf, M. Kläui, and T. Kampfrath. Ultrabroadband single-cycle terahertz pulses with peak fields of 300 kv cm^{-1} from a metallic spintronic emitter. *Applied Physics Letters*, 110(25):252402, 2017.
- [56] E.T. Papaioannou and R. Beigang. Thz spintronic emitters: a review on achievements and future challenges. *Nanophotonics*, 10(4):1243–1257, 2021.
- [57] Edwin H. Hall. On a new action of the magnet on electric currents. *American Journal of Mathematics*, 2(3):287–292, 1879.
- [58] M. I. Dyakonov and V. I. Perel. Current-induced spin orientation of electrons in semiconductors. *Physics Letters A*, 35(6):459–460, 1971.
- [59] Jairo Sinova, Sergio O. Valenzuela, Jörg Wunderlich, Craig H. Back, and Tomáš Jungwirth. Spin hall effects. *Reviews of Modern Physics*, 87(4):1213–1260, 2015.
- [60] J. E. Hirsch. Spin hall effect. *Physical Review Letters*, 83(9):1834–1837, 1999.
- [61] M. Battiato, K. Carva, and P.M. Oppeneer. Superdiffusive spin transport as a mechanism of ultrafast demagnetization. *Physical Review Letters*, 105(2):027203, 2010.
- [62] Weipeng Wu, Charles Yaw Ameyaw, Matthew F Doty, and M Benjamin Jungfleisch. Principles of spintronic thz emitters. *Journal of Applied Physics*, 130(9), 2021.
- [63] T. Seifert, S. Jaiswal, U. Martens, J. Hannegan, L. Braun, P. Maldonado, F. Freimuth, A. Kronenberg, J. Henrizi, I. Radu, and E. Beaupaire. Efficient metallic spintronic emitters of ultrabroadband terahertz radiation. *Nature Photonics*, 10(7):483–488, 2016.

- [64] R. Adam, G. Chen, D.E. Bürgler, T. Shou, I. Komissarov, S. Heitfeld, H. Hardtdegen, M. Mikulics, C.M. Schneider, and R. Sobolewski. Magnetically and optically tunable terahertz radiation from ta/nife/pt spintronic nanolayers generated by femtosecond laser pulses. *Applied Physics Letters*, 114(21):212405, 2019.
- [65] T. Kampfrath, M. Battiato, P. Maldonado, G. Eilers, J. Nötzold, S. Mährlein, V. Zbarsky, F. Freimuth, Y. Mokrousov, S. Blügel, and M. Wolf. Terahertz spin current pulses controlled by magnetic heterostructures. *Nature Nanotechnology*, 8(4):256–260, 2013.
- [66] S. Manipatruni, D.E. Nikonov, C.C. Lin, T.A. Gosavi, H. Liu, B. Prasad, Y.L. Huang, E. Bonturim, R. Ramesh, and I.A. Young. Scalable energy-efficient magnetoelectric spin-orbit logic. *Nature*, 565(7737):35–42, 2019.
- [67] R. Yu, B.F. Miao, L. Sun, Q. Liu, J. Du, P. Omelchenko, B. Heinrich, M. Wu, and H.F. Ding. Determination of spin hall angle and spin diffusion length in β -phase-dominated tantalum. *Physical Review Materials*, 2(7):074406, 2018.
- [68] X. Tao, Q. Liu, B. Miao, R. Yu, Z. Feng, L. Sun, B. You, J. Du, K. Chen, S. Zhang, and L. Zhang. Self-consistent determination of spin hall angle and spin diffusion length in pt and pd: The role of the interface spin loss. *Science Advances*, 4(6):eaat1670, 2018.
- [69] L. Liu, C.F. Pai, Y. Li, H.W. Tseng, D.C. Ralph, and R.A. Buhrman. Spin-torque switching with the giant spin hall effect of tantalum. *Science*, 336(6081):555–558, 2012.
- [70] C.F. Pai, L. Liu, Y. Li, H.W. Tseng, D.C. Ralph, and R.A. Buhrman. Spin transfer torque devices utilizing the giant spin hall effect of tungsten. *Applied Physics Letters*, 101(12):122404, 2012.
- [71] Y. Ishikuro, M. Kawaguchi, N. Kato, Y.C. Lau, and M. Hayashi. Dzyaloshinskii-moriya interaction and spin-orbit torque at the ir/co interface. *Physical Review B*, 99(13):134421, 2019.
- [72] T. Fache, J.C. Rojas-Sanchez, L. Badie, S. Mangin, and S. Petit-Watelot. Determination of spin hall angle, spin mixing conductance,

- and spin diffusion length in cofeb/ir for spin-orbitronic devices. *Physical Review B*, 102(6):064425, 2020.
- [73] C. Hahn, G. De Loubens, O. Klein, M. Viret, V.V. Naletov, and J.B. Youssef. Comparative measurements of inverse spin hall effects and magnetoresistance in yig/pt and yig/ta. *Physical Review B*, 87(17):174417, 2013.
- [74] R. Schneider, M. Fix, J. Bensmann, S. Michaelis de Vasconcellos, M. Albrecht, and R. Bratschitsch. Composition-dependent ultrafast thz emission of spintronic cofe/pt thin films. *Applied Physics Letters*, 120(4):042404, 2022.
- [75] G. Torosyan, S. Keller, L. Scheuer, R. Beigang, and E.T. Papaioannou. Optimized spintronic terahertz emitters based on epitaxial grown fe/pt layer structures. *Scientific Reports*, 8(1):1311, 2018.
- [76] E.T. Papaioannou, G. Torosyan, S. Keller, L. Scheuer, M. Battiato, V.K. Mag-Usara, J. L’huillier, M. Tani, and R. Beigang. Efficient terahertz generation using fe/pt spintronic emitters pumped at different wavelengths. *IEEE Transactions on Magnetics*, 54(11):1–5, 2018.
- [77] A. Fert and F.N. Van Dau. Spintronics, from giant magnetoresistance to magnetic skyrmions and topological insulators. *Comptes Rendus Physique*, 20(7-8):817–831, 2019.
- [78] R. Sun, S. Yang, X. Yang, E. Vetter, D. Sun, N. Li, L. Su, Y. Li, Z.Z. Gong, and Z.K. Xie. Large tunable spin-to-charge conversion induced by hybrid rashba and dirac surface states in topological insulator heterostructures. *Nano Letters*, 19(7):4420–4426, 2019.
- [79] H. Isshiki, P. Muduli, J. Kim, K. Kondou, and Y. Otani. Phenomenological model for the direct and inverse edelstein effects. *Physical Review B*, 102(18):184411, 2020.
- [80] Z. Xue, W. Li, W. Zhang, M. Wang, D. Yu, Z. Li, and W. Zhao. Spintronic terahertz generation and detection in the time domain. *Physical Review Applied*, 20(3):034037, 2023.

- [81] Brian D Milbrath, Anthony J Peurrung, Mary Bliss, and William J Weber. Radiation detector materials: An overview. *Journal of Materials Research*, 23(10):2561–2581, 2008.
- [82] C. Leroy and P.G. Rancoita. *Principles of Radiation Interaction in Matter and Detection*. World Scientific, 2011.
- [83] T. Tanabe, H. Sumikura, H. Taniyama, A. Shinya, and M. Notomi. All-silicon sub-gb/s telecom detector with low dark current and high quantum efficiency on chip. *Applied Physics Letters*, 96(10):101103, 2010.
- [84] Y. Eisen, A. Shor, and I. Mardor. Cdte and cdznte x-ray and gamma-ray detectors for imaging systems. *IEEE Transactions on Nuclear Science*, 51(3):1191–1198, 2004.
- [85] Y. Zhao, C. Li, and L. Shen. Recent advances on organic-inorganic hybrid perovskite photodetectors with fast response. *InfoMat*, 1(2):164–182, 2019.
- [86] D.H. Auston. Ultrafast optoelectronics. In *Ultrashort Laser Pulses: Generation and Applications*, Topics in Applied Physics, pages 183–233. Springer-Verlag Berlin Heidelberg, Berlin, Germany, 2006.
- [87] S.E.R.G.I.O. Cova, A. Lacaita, M. Ghioni, G.I.A.N.C.A.R.L.O. Ripamonti, and T.A. Louis. 20-ps timing resolution with single-photon avalanche diodes. *Review of Scientific Instruments*, 60(6):1104–1110, 1989.
- [88] C. Gahl, A. Azima, M. Beye, M. Deppe, K. Döbrich, U. Haslinger, F. Hennies, A. Melnikov, M. Nagasono, A. Pietzsch, and M. Wolf. A femtosecond x-ray/optical cross-correlator. *Nature Photonics*, 2(3):165–169, 2008.
- [89] Liping Liao, Evgeniya Kovalska, Vlastimil Mazanek, Lukáš Valdman, Lukáš Dekanovsky, Wu Bing, David Sedmidubský, et al. Layered selenophosphate hgpse₃ single crystals: a new candidate for x-ray to visible light photodetectors. *Journal of Materials Chemistry C*, 10(22):8834–8844, 2022.

- [90] Henry Chen, Sue Kutcher, Julie Wen, Sudhir Trivedi, Jing Cheng, Genyu Chen, Debamitra Chakraborty, Ivan Komissarov, and Roman Sobolewski. Cadmium magnesium telluride for next-generation x-ray free electron laser, synchrotron, and many other applications. *IEEE Transactions on Nuclear Science*, 70(3):286–291, 2023.
- [91] Brian E McCandless and James R Sites. Cadmium telluride solar cells. *Handbook of photovoltaic science and engineering*, pages 600–641, 2011.
- [92] Antony Rogalski. HgCdTe infrared detector material: history, status and outlook. *Reports on Progress in Physics*, 68(10):2267, 2005.
- [93] Xiaohui Zhan, Ruoqiao Zhang, Xiaofeng Niu, Ilmar Hein, Brent Budden, Shuoxing Wu, Nicolay Markov, Cameron Clarke, Yi Qiang, Hiroki Taguchi, et al. Comprehensive evaluations of a prototype full field-of-view photon counting ct system through phantom studies. *Physics in Medicine & Biology*, 68(17):175007, 2023.
- [94] V. Sokalski, D. M. Bromberg, D. Morris, M. T. Moneck, E. Yang, L. Pileggi, and J. G. Zhu. Naturally oxidized feco as a magnetic coupling layer for electrically isolated read/write paths in mlogic. *IEEE Transactions on Magnetics*, 49(7):4351–4354, 2013.
- [95] Jing Cheng, Ivan Komissarov, Genyu Chen, Debamitra Chakraborty, Roman Adam, Daniel E Bürgler, Sarah Heidtfeld, Derang Cao, Markus Büscher, Hilde Hardtdegen, et al. Terahertz inverse spin hall effect in spintronic nanostructures with various ferromagnetic materials. *Journal of Magnetism and Magnetic Materials*, 593:171641, 2024.
- [96] S. D. Benjamin, H. S. Loka, A. Othonos, and P. W. E. Smith. Ultrafast dynamics of nonlinear absorption in low-temperature-grown gaas. *Applied Physics Letters*, 68:2544–2546, 1996.
- [97] X. Zheng, Y. Xu, R. Sobolewski, R. Adam, M. Mikulics, M. Siegel, and P. Kordos. Femtosecond response of a free-standing lt-gaas photoconductive switch. *Applied Optics*, 42:1726–1731, 2003.
- [98] T. Gong, L. X. Zheng, W. Xiong, W. Kula, Y. Kostoulas, R. Sobolewski, and P. M. Fauchet. Femtosecond optical response of y-ba-cu-o thin films: The dependence on optical frequency, excitation

- intensity, and electric current. *Physical Review B*, 47:14495–15000, 1993.
- [99] J.H. Hodak, I. Martini, and G.V. Hartland. Ultrafast electron-phonon relaxation dynamics in gold nanoparticles. *Chemical Physics Letters*, 284:135–141, 1998.
- [100] R.H.M. Groeneveld, R. Sprik, and A. Lagendijk. Femtosecond spectroscopy of electron-electron and electron-phonon energy relaxation in metals. *Physical Review B*, 51:11433–11445, 1995.
- [101] R.W. Schoenlein, W.Z. Lin, J.G. Fujimoto, and G.L. Eesley. Femtosecond studies of transient electronic and structural dynamics in metals. *Physical Review Letters*, 58:1680–1683, 1987.
- [102] P. Borri, F. Romstad, W. Langbein, A. Kelly, J. Mork, and J. Hvam. Separation of coherent and incoherent nonlinearities in a heterodyne pump-probe experiment. *Optics Express*, 7(3):107–112, 2000.
- [103] J Cheng, G Chen, D Chakraborty, S Kutcher, J Wen, H Chen, S Trivedi, and Roman Sobolewski. (cd, mg) te crystals for picosecond-response optical-to-x-ray radiation detectors. *Review of Scientific Instruments*, 93(11), 2022.
- [104] N. Kovalchuk, K. A. Niherysh, M. M. Mikhalik, and I. Komissarov. Possibility of determining the graphene doping level using raman spectra. *Journal of Applied Spectroscopy*, 2018.
- [105] D. Yoon, H. Moon, H. Cheong, J. S. Choi, J. A. Choi, and B. H. Park. Variations in the raman spectrum as a function of the number of graphene layers. *Journal of the Korean Physical Society*, 55(3):1299–1303, 2009.
- [106] S. Kim and S. Ryu. Thickness-dependent native strain in graphene membranes visualized by raman spectroscopy. *Carbon*, 100:283–290, April 2016.
- [107] J. E. Lee, G. Ahn, J. Shim, Y. S. Lee, and S. Ryu. Optical separation of mechanical strain from charge doping in graphene. *Nature Communications*, 3:1–8, August 2012.

- [108] A. C. Ferrari and D. M. Basko. Raman spectroscopy as a versatile tool for studying the properties of graphene. *Nature Nanotechnology*, 8(4):235–246, April 2013.
- [109] J.R. Sánchez, L. Vila, G. Desfonds, S. Gambarelli, J.P. Attané, J.M. De Teresa, C. Magén, and A. Fert. Spin-to-charge conversion using rashba coupling at the interface between non-magnetic materials. *Nature Communications*, 4(1):2944, 2013.
- [110] F. De Juan, A.G. Grushin, T. Morimoto, and J.E. Moore. Quantized circular photogalvanic effect in weyl semimetals. *Nature Communications*, 8:1–7, 2017.
- [111] H. Yuan, X. Wang, B. Lian, H. Zhang, X. Fang, B. Shen, G. Xu, Y. Xu, S.C. Zhang, H.Y. Hwang, and Y. Cui. Generation and electric control of spin–valley-coupled circular photogalvanic current in wse_2 . *Nature Nanotechnology*, 9(10):851–857, 2014.
- [112] K.N. Okada, N. Ogawa, R. Yoshimi, A. Tsukazaki, K.S. Takahashi, M. Kawasaki, and Y. Tokura. Enhanced photogalvanic current in topological insulators via fermi energy tuning. *Physical Review B*, 93(8):081403, 2016.
- [113] J. Li, L. Lin, D. Rui, Q. Li, J. Zhang, N. Kang, Y. Zhang, H. Peng, Z. Liu, and H.Q. Xu. Electron–hole symmetry breaking in charge transport in nitrogen-doped graphene. *ACS Nano*, 2017.
- [114] N. Dale, R. Mori, M.I.B. Utama, J.D. Denlinger, C. Stansbury, C.G. Fatuzzo, S. Zhao, K. Lee, T. Taniguchi, K. Watanabe, C. Jozwiak, A. Bostwick, E. Rotenberg, R.J. Koch, F. Wang, and A. Lanzara. Correlation-driven electron-hole asymmetry in graphene field effect devices. *NPJ Quantum Materials*, 7:1–7, 2022.
- [115] A.G. Rybkin, A.A. Rybkina, M.M. Otrokov, O.Y. Vilkov, I.I. Klimovskikh, A.E. Petukhov, M.V. Filianina, V.Y. Voroshnin, I.P. Rusinov, A. Ernst, A. Arnau, E.V. Chulkov, and A.M. Shikin. Magneto-spin-orbit graphene: Interplay between exchange and spin-orbit couplings. *Nano Letters*, 18:1564–1574, 2018.
- [116] J. Klinovaja and D. Loss. Rky interaction in carbon nanotubes and graphene nanoribbons. *Physical Review B*, 87:045422, 2013.

-
- [117] A.L. Danilyuk, I.V. Komissarov, A.V. Kukharev, F. Le Normand, J.M. Hernandez, J. Tejada, and S.L. Prischepa. Impact of cnt medium on the interaction between ferromagnetic nanoparticles. *EPL (Europhysics Letters)*, 117:27007, 2017.
- [118] M. Mecklenburg, J. Woo, and B.C. Regan. Tree-level electron-photon interactions in graphene. *Physical Review B - Condensed Matter and Materials Physics*, 81:245401, 2010.
- [119] T.H.E. Lahtinen, K.J.A. Franke, and S. Van Dijken. Electric-field control of magnetic domain wall motion and local magnetization reversal. *Scientific Reports*, 2:1–6, 2012.
- [120] D. Marchenko, A. Varykhalov, M.R. Scholz, G. Bihlmayer, E.I. Rashba, A. Rybkin, A.M. Shikin, and O. Rader. Giant rashba splitting in graphene due to hybridization with gold. *Nature Communications*, 3:1–6, 2012.
- [121] J. Klinovaja and D. Loss. Rkky interaction in carbon nanotubes and graphene nanoribbons. *Physical Review B*, 87:045422, 2013.
- [122] A.L. Danilyuk, A.V. Kukharev, and S.L. Prischepa. Long-range exchange interaction between ferromagnetic nanoparticles embedded in carbon nanotubes. *IEEE Transactions on Magnetism*, pages 1–1, 2021.
- [123] A. Varykhalov, D. Marchenko, M.R. Scholz, E.D.L. Rienks, T.K. Kim, G. Bihlmayer, J. Sánchez-Barriga, and O. Rader. Ir(111) surface state with giant rashba splitting persists under graphene in air. *Physical Review Letters*, 108:066804, 2012.
- [124] E.I. Rashba. Graphene with structure-induced spin-orbit coupling: Spin-polarized states, spin zero modes, and quantum hall effect. *Physical Review B*, 79:161409, 2009.
- [125] M. Krivenkov, E. Golias, D. Marchenko, J. Sánchez-Barriga, G. Bihlmayer, O. Rader, and A. Varykhalov. Nanostructural origin of giant rashba effect in intercalated graphene. *2D Materials*, 4:035010, 2017.
- [126] M.M. Otrokov, I.I. Klimovskikh, F. Calleja, A.M. Shikin, O. Vilkov, A.G. Rybkin, D. Estyunin, S. Muff, J.H. Dil, A.L. Vázquez De Parga,

- R. Miranda, H. Ochoa, F. Guinea, J.I. Cerdá, E.V. Chulkov, and A. Arnau. Evidence of large spin-orbit coupling effects in quasi-free-standing graphene on pb/ir(1 1 1). *2D Materials*, 5:035029, 2018.
- [127] E.V. Zhizhin, A. Varykhalov, A.G. Rybkin, A.A. Rybkina, D.A. Pudikov, D. Marchenko, J. Sánchez-Barriga, I.I. Klimovskikh, G.G. Vladimirov, O. Rader, and A.M. Shikin. Spin splitting of dirac fermions in graphene on ni intercalated with alloy of bi and au. *Carbon*, 93:984–996, 2015.
- [128] D. E. Bürgler. Memristive phenomena – from fundamental physics to neuromorphic computing. In R. Waser and M. Wuttig, editors, *47th IFF Spring School 2016*, chapter A8. Forschungszentrum Jülich, Jülich, Germany, 2016. Lecture Notes.
- [129] A. Eschenlohr, L. Persichetti, T. Kachel, M. Gabureac, P. Gambardella, and C. Stamm. Spin dynamics at interfaces on femtosecond timescales. *Journal of Physics: Condensed Matter*, 29(38):384002, 2017.
- [130] K. Inomata, N. Ikeda, N. Tezuka, R. Goto, S. Sugimoto, M. Wojcik, and E. Jedryka. Highly spin-polarized materials and devices for spintronics. *Science and Technology of Advanced Materials*, 9(1):014101, 2008.
- [131] J. Tauc. Optical properties and electronic structure of amorphous ge and si. *Materials Research Bulletin*, 3:37–46, 1968.
- [132] S. Sirohi and T. P. Sharma. Bandgaps of cadmium telluride sintered film. *Optical Materials*, 13:267–269, 1999.
- [133] B. D. Viezbicke, S. Patel, B. E. Davis, and D. P. Birnie. Evaluation of the tauc method for optical absorption edge determination: ZnO thin films as a model system. *Physica Status Solidi B*, 252:1700–1710, 2015.
- [134] Hamna F. Haneef, Andrew M. Zeidell, and Oana D. Jurchescu. Charge carrier traps in organic semiconductors: a review on the underlying physics and impact on electronic devices. *Journal of Materials Chemistry C*, 8(3):759–787, 2020. Received 17th October 2019, Accepted 17th December 2019, First published 17th December 2019.

-
- [135] D. J. Hilton. Ultrafast pump-probe spectroscopy. In *Optical techniques for solid-state materials characterization*. Taylor and Francis Group, 2012.
- [136] J. Kim. Effect of free-carrier absorption on the carrier dynamics of quantum-dot semiconductor optical amplifiers. *Journal of Korean Physical Society*, 55:512–516, 2009.
- [137] Eugene Hecht. *Optics*. Addison-Wesley, 4th edition, 2002.
- [138] R. N. Hall. Electron-hole recombination in germanium. *Physical Review*, 87:387, 1952.
- [139] W. Shockley and W. T. Read. Statistics of the recombinations of holes and electrons. *Physical Review*, 87:835, 1952.
- [140] J. Serafini, A. Hossain, R. B. James, S. B. Trivedi, and R. Sobolewski. Time-resolved, nonequilibrium carrier and coherent acoustic phonon dynamics in (cd, mg) te single crystals for radiation detectors. *Semiconductor Science and Technology*, 34(3):035021, 2019.
- [141] D. E. Nagle, P. P. Craig, W. A. Steyert, and R. D. Taylor. Paramagnetism of fe impurities in transition metals. *Physical Review Letters*, 9(1):12–14, 1962.
- [142] J. M. Leger, J. Loriers, and J. P. Bros. New kind of surface state in nearly-free-electron metals. *Physical Review B*, 6(4):1142–1145, 1972.
- [143] M. Matthiesen, D. Afanasiev, J. R. Hortensius, T. C. van Thiel, R. Medapalli, M. Lee, E. Lesne, B. A. Ivanov, A. V. Kimel, B. Koopmans, E. J. Geluk, M. P. de Jong, R. A. Duine, and A. D. Caviglia. Ultrafast spin-currents in optically excited amorphous gdfeco. *Applied Physics Letters*, 116(21):212405, 2020.
- [144] A. Tomasino, A. Parisi, S. Stivala, P. Livreri, A.C. Cino, A.C. Busacca, M. Peccianti, and R. Morandotti. Wideband thz time domain spectroscopy based on optical rectification and electro-optic sampling. *Scientific Reports*, 3(1):1–8, 2013.

-
- [145] J. Serafini, Y. Akbas, L. Crandall, R. Bellman, C.K. Williams, and R. Sobolewski. Time-resolved, nonequilibrium carrier dynamics in si-on-glass thin films for photovoltaic cells. *Semiconductor Science and Technology*, 31(4):045006, 2016.
- [146] J. Serafini, A. Hossain, R.B. James, M. Guziewicz, R. Kruszka, W. Słysz, D. Kochanowska, J.Z. Domagala, A. Mycielski, and R. Sobolewski. Photoconductive and electro-optic effects in (cd, mg) te single crystals measured in an experiment-on-chip configuration. *Applied Physics Letters*, 111(1):011108, 2017.